The neurobiological basis of inter-individual variability in visual perception

Chen Song

August 2015

Thesis Submitted to

University College London

for Degree of

Doctor of Philosophy

Institute of Neurology

University College London

Declaration

I, Chen Song, confirm that the work presented in this thesis is my own. Where information has been derived from other sources, I confirm that this has been indicated in the thesis. The work presented in this thesis has been published in the following peer reviewed papers.

Song, C., Schwarzkopf, D. S., Kanai, R., and Rees, G. (2015). Neural Population Tuning Links Visual Cortical Anatomy to Human Visual Perception. Neuron, 85(3): 1-16

Song, C., Schwarzkopf, D. S., and Rees, G. (2013). Variability in visual cortex size reflects trade off between local orientation sensitivity and global orientation modulation. Nature Communications, 4: 3201

Song, C., Schwarzkopf, D. S., Lutti, A., Li, B. J., Kanai, R., and Rees, G. (2013). Effective connectivity within human primary visual cortex predicts inter individual diversity in illusory perception. Journal of Neuroscience, 33(48): 18781-18791

Schwarzkopf, D. S., **Song, C.**, and Rees, G. (2011). The surface area of human V1 predicts the subjective experience of object size. Nature Neuroscience, 14(1): 28-30

Song, C., Schwarzkopf, D. S., Kanai, R., and Rees, G. (2011). Reciprocal anatomical relationship between primary sensory and prefrontal cortices in the human brain. Journal of Neuroscience, 31(26): 9472-9480

Acknowledgements

My research experience over the past few years at UCL is beyond words. I consider myself as extremely lucky to have the opportunity to conduct neuroscience research at UCL Queen Square, a place that have cultivated many of the world′s most eminent neuroscientists in the history and the current. The tradition of scientific excellence is all over the air, as is the unbelievably friendly atmosphere of collaboration. For all these, I would love to give my greatest gratitude to my supervisors and to others that I have had the honor working with.

My primary supervisor, Geraint Rees, and my secondary supervisor, Karl Friston, both represent amazing examples of how one could combine a scientific spirit with a humanistic heart. Without their unconditional support for letting me pursue my passion yet bearing with my naive ignorance and stubbornness, I would never be able to get as far as I am today. From Geraint, I learnt the art of experimental science, that a good experiment design is where the positive and the negative results are both meaningful and are meant to test alternative hypothesis; I also learnt the beauty of scientific writing, and perhaps the most unexpected, the style of inspirational leadership. From Karl, I learnt the power of theoretical science, that theoretical modeling can go beyond itself and be applied to infer hidden variables from experimental data; I also witnessed, from the countless amount of time that Karl spent in giving anyone in-need the free advices, the degree of generosity that a scientist can have in the very competitive and cruel world of modern science. Wherever I go and wherever I end up with in future, these sweet memory are going to stay with me and keep encouraging me during the hard times.

Abstract

Visual perception is the conscious experience that is unique to each individual. However, conventional neuroscience studies tend to focus on the commonality in visual perception across different individuals and fail to address the key properties of any conscious experience - its individuality and subjectivity. In my thesis, I investigated the neurobiological basis of perceptual variability across healthy human adults, through a combined approach of psychophysics, in-vivo MR imaging, in-vitro histological imaging, and computational modeling. I found that perception of local and global visual features, as assessed respectively from visual discrimination of local feature details and visual illusion induced by global feature contexts, exhibits a ten-fold inter-individual variability that correlates with the morphology of primary visual cortex. Specifically, an increase in the surface area of primary visual cortex is associated with a shift in the scope of visual feature perception from global-context-oriented to local-detail-oriented, where individuals with smaller visual cortical surface area experience stronger visual illusion and individuals with larger visual cortical surface area perform more accurate visual discrimination. Intriguingly, an increase in the thickness of primary visual cortex has the opposite impact, where visual discrimination is less accurate at visual field locations corresponding to thicker parts of primary visual cortex. The functional impact that visual cortical anatomy exerts on visual feature perception is recapitulated in visual neural selectivity. I found that in individuals with larger surface area of primary visual cortex, visual cortical neurons exhibit higher selectivity and respond to a smaller, localised visual field range. By contrast, at thicker parts of primary visual cortex, visual cortical neurons exhibit lower selectivity and respond to a larger, globalised visual field range. The opposite functional impacts exhibited by the two morphological dimensions, the surface area and the thickness, of primary visual cortex can nonetheless be unified under the framework of intracortical scaling. I found that the scaling of intracortical connectivity with visual cortical morphology shifts the scope of both visual feature perception and visual neural selectivity between global- and local-oriented. Together these findings revealed that the individuality in visual feature perception arises neurobiologically from the variability in visual cortical morphology, through the mediation of intracortical connectivity and visual neural selectivity.

Contents

List of Figures

Chapter 1

General Introduction

1.1 Overlooked existence of perceptual variability

It is well recognized that a substantial degree of variability exists across healthy human individuals in high-level cognitive functions such as the style of thinking and the skill of communication, where such variability is considered as examples of personality. At the same time, it is often overlooked that a substantial degree of inter-individual variability also exists in low-level perceptual functions. Instead, it is usually assumed that perception of the same physical stimulus is more or less identical across healthy human individuals. Consequently, conventional neuroscience studies tend to focus on the perceptual commonality across individuals and treat inter-individual perceptual variability as a source of noise [1].

Whereas conventional neuroscience studies are focused on the perceptual commonality across individuals, perception is by definition a subjective experience that is unique to each individual. As such, the key properties of any perceptual experiences are their individuality and subjectivity. Indeed, a close look at many of our perceptual experiences suggests that individuals differ in their low-level perceptual functions just as much as they do in high-level cognitive functions [2, 3]. As perceptual experiences are the basis of human cognition, such inter-individual variability in low-level perceptual functions may in fact shape inter-individual variability in everyday decision-making, memory formation, or other high-level cognitive functions.

Given the importance of inter-individual perceptual variability, it is essential to understand the mechanisms underlying the individuality and the subjectivity of our perceptual experiences. Among different perceptual domains, the visual domain accounts for more than 80% of our perceptual experiences. Moreover, compared to other perceptual systems, the visual system is probably the best studied, and we have gained substantial knowledge spanning multiple levels,

from the anatomy of visual cortices, to the connectivity between visual neural populations, to the response properties of single visual neurons. Therefore, the visual domain may serve as a good starting point for exploring the mechanisms underlying inter-individual perceptual variability.

Indeed, a number of researchers have started to explore the variability across healthy human adults in visual perception. It was found that perception of visual contextual illusion, where the presence of a surrounding context biased the perceived feature of a central stimulus, varied across individuals over ten-folds [3]. Inter-individual variability was observed not only in visual illusion, but also in visual discrimination [2, 4, 5, 6]. Intriguingly, inter-individual variability in visual discrimination exhibited covariance across different categories of visual features, such that individuals with higher performance in discriminating one visual feature (e.g., orientation) also performed better at discriminating another (e.g., luminance). By contrast, inter-individual variability in visual contextual illusion was dissociated among different categories of visual features [3].

These findings suggest that inter-individual variability in visual perception may not arise purely from generic factors such as decision-making ability, but instead has its neurobiological basis in the specific ways that the visual system processed visual input. In this thesis, I explored how the differences across individuals in cortical processing of the same visual input gave rise to inter-individual variability in visual perception, and how such inter-individual differences in visual cortical processing were in turn shaped by the variability in visual cortical anatomy. To this end, I would review in this chapter our existing knowledge of visual processing. First, I would discuss how the light signal, the very fundamental visual input, is transduced into the neural signal. Then, I would discuss how the seemingly identical neural signals give rise to the radically different perceptual experiences. Last, I would discuss how our existing knowledge of visual processing might contribute to our understanding of inter-individual variability in visual perception.

1.2 From light signal to neural signal

When we open our eyes, we see a world full of visual richness. To us, each object has its own shape, color, size, location, and many other visual features. The visual world is so rich that for a moment, we may even think that perception of different visual features are triggered by signals of distinct forms, as if our perception of color blue is triggered by a blue signal and our perception of an oriented line by a line signal. However, when we think about the nature of

visual processing, we soon realize that our seemingly diverse perceptual experience is in fact triggered by the same signal, a light signal. The wavelength and the intensity of light signal determine the color and the luminance that we perceive, whereas the visual field location of light signal defines the spatial pattern that we perceive [7]. The fact that a simple light signal could give rise to the complex visual world that we experience illustrates the remarkable power of visual processing. It also suggests that the perceptual variability across individuals is a result of inter-individual differences in visual processing of the same light signal. To understand the neurobiological basis of inter-individual variability in visual perception, it is therefore essential to start from the beginning of visual processing and examine how the light signal is transduced into a neural signal [8, 9].

Visual processing begins with the light entering the pupil, where the lens and the cornea project the inverted light onto the back of the eye. At the back of the eye is the retina, a layered structure composed of interconnected cells (Figure 1.1). Different retinal layers contain cells of different types that serve different functions [8, 9]. From the outmost to the innermost, the is the layer of Muller cells, the layer of ganglion cells, the layer of biopolar, horizontal, amacrine cells, and the layer of photoreceptor cells, respectively [10]. The Muller cell is a type of glial cell that serves as the supporting cell for neurons in the retina, whereas the ganglion cell, the biopolar cell, the horizontal cell, the amacrine cell, and the photoreceptor cell are different types of neurons.

Light travels through the outer retinal layers and reaches the layer of photoreceptor cells, where it gets transduced into neural signal via phototransduction (Figure 1.2). Playing the key role in phototransduction is a molecular called photopigment, located on the membrane of photoreceptor cells [11]. Photopigment is composed of a light-absorbing chromophore (retinal) and a G-protein-coupled receptor (opsin). Upon the absorption of light photon, the retinal changes its configuration from 11-cis to all-trans and breaks away from the opsin. This change leads to the activation of transducin (a G-protein) and phosphodiesterase (an enzyme), which then hydrolyzes cGMP (a second messenger). The decrease in cGMP concentration causes the closure of sodium channels, which in turn causes the hyperpolarization of photoreceptor membrane and the reduction of neurotransmitter release at photoreceptor synapse.

This chain of phototransduction reactions gives rise to a series of response properties that are unique to photoreceptor cells and enable the encoding of light intensity. In most sensory system, stimulation of a receptor cell causes its membrane to depolarize, which ultimately triggers an action potential and the release of neurotransmitter onto its postsynaptic cell. By

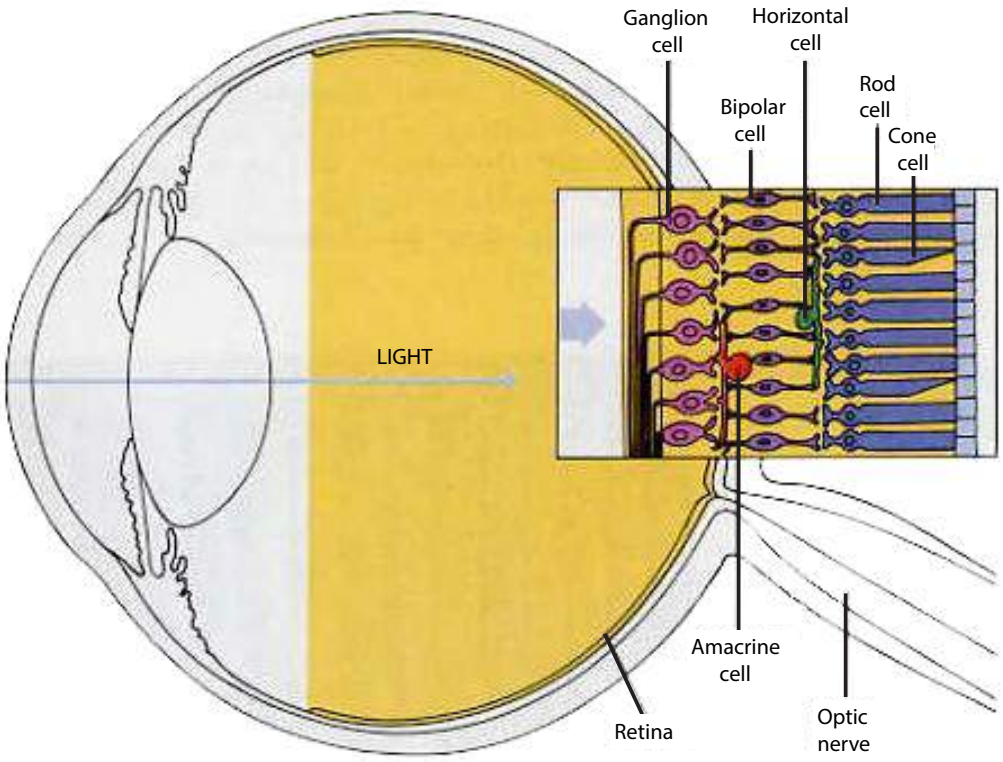

Figure 1.1: Layering of retina. The enlarged retina illustrates the relative positions of different retinal layers. The light signal travels through the layer of Muller cells, the layer of ganglion cells, the layer of biopolar, horizontal, amacrine cells, and arrives at the layer of photoreceptor cells where it is transduced into the neural signal. Then, the neural signal travels the opposite direction, from the layer of photoreceptor cells, via the layer of biopolar, horizontal, amacrine cells, to the layer of ganglion cells where it gets inputted into the brain. Figure adapted from [7].

contrast, light stimulation of a photoreceptor cell leads to the hyperpolarization rather than the depolarization of its membrane. Consequently, the photoreceptor cell does not exhibit action potential, but instead has its membrane potential and its neurotransmitter release changed in a graded fashion where the rate of change is determined by the intensity of light signal [12]. As such, the light intensity is encoded in the membrane potential of photoreceptor cells and this information is passed onto bipolar cells via the rate of neurotransmitter release.

While sharing similar mechanisms of phototransduction, photoreceptor cells can be divided into two classes (rod, cone) that have different photopigments. Specifically, the photopigment in rod cells can be stimulated by a single photon yet that in cone cells requires a large number of photons [11]. As a result, the rod cells exhibit high sensitivity (but low specificity) and function at dim light, whereas the cone cells exhibit high specificity (but low

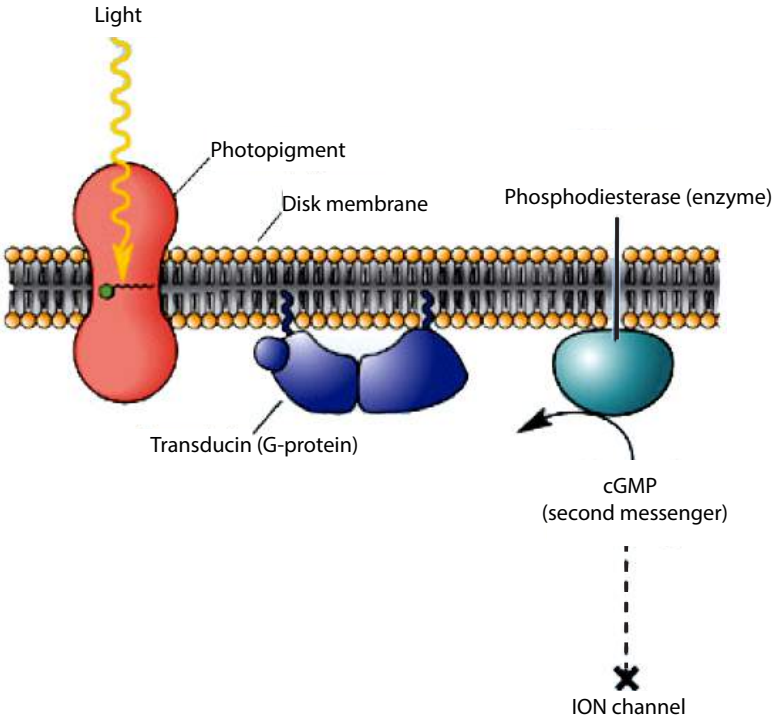

Figure 1.2: From light signal to neural signal. Phototransduction is the process by which the physical signal of light is converted into the biological signal of neural activity. This process occurs via the molecular photopigment that locates on the membrane of photoreceptor cell. Upon the absorption of light, photopigment changes its configuration, which leads to the closure of sodium channels and in turn causes the hyperpolarization of photoreceptor cell. Figure adapted from [7].

sensitivity) and function at normal light. In humans, the cone cells can be further divided into three classes (S, M, L), according to the wavelength of light photons that the photopigment absorbs. The photopigment in S, M, and L cone cells responds respectively to light of short, medium, and long wavelength [13, 14]. The diversity among photoreceptor cells in their wavelength responses allows the encoding of light wavelength and the relay of this information onto bipolar cells.

The intensity and the wavelength of light signal are encoded in the membrane potential of photoreceptor cells. The visual field location of light signal, on the other hand, is encoded in the receptive field of photoreceptor cells. By nature, the retina is a tissue sheet, where the photoreceptor cells at different retinal locations have different receptive fields and respond to light at different visual field locations. Specifically, the receptive field of a single photoreceptor cell is a cone-shaped visual field volume whose apex is located at the center of the lens and whose angle covers all directions from which the light signal can alter the membrane potential of that

cell. This spatial specificity, where a single photoreceptor cell does not respond uniformly to lights from anywhere but responds selectively to lights from certain directions, enables the encoding of light location.

In summary, the transduction of light signal into neural signal occurs via photoreceptor cells. A single photoreceptor cell responds to light signal from a certain range of wavelength and a certain range of visual field location, by hyperpolarizing its membrane potential and reducing its neurotransmitter release according to the intensity of light. Such spatially-organized, wavelength-dependent, intensity-regulated responses of photoreceptor cells form the basis of visual processing. However, the amount of information that photoreceptor cells can encode on their own is very limited, despite the large number (150 million) of photoreceptor cells present in adult human [8, 9]. The complexity of visual encoding is accomplished via the diversity of visual neural responses. For example, regardless of the properties (intensity, wavelength, location) of the input light signal, the same neural signal (excitatory neurotransmitter glutamate) is outputted from photoreceptor cells to bipolar cells. It is via the diversity in membrane receptor of bipolar cells that the same signal from photoreceptor cells (excitatory neurotransmitter glutamate) gets to produce different effects on different bipolar cells [15, 16]. To understand how the seemingly identical neural signals give rise to our diverse perceptual experiences, it is therefore essential to examine the diversity and complexity of visual neural responses along visual processing.

1.3 From neural signal to perceptual experience

1.3.1 Emergence of center-surround receptive field

Via phototransduction, the light signal gets transduced into the neural signal, in the form of hyperpolarized membrane potential and reduced neurotransmitter release of photoreceptor cells. To enter cortical processing, the neural signal needs to travel through retina in the opposite direction of light signal, from the layer of photoreceptor cells, via the layer of biopolar, horizontal, amacrine cells, to the layer of ganglion cells where it gets inputted into the brain [8, 9]. Along this chain of signal relay, the diversity and complexity in visual neural responses begin to emerge, as a result of the neural interconnections within and between retinal layers.

The neural interconnections in the retina follow two paths: a direct path and an indirect path [15, 16]. In the direct path, the photoreceptor cells feedforward directly to the bipolar cells, and the bipolar cells feedforward directly to the ganglion cells. In the indirect path, the photoreceptor cells feedforward to the bipolar cells through the horizontal cells, and the bipo-

lar cells feedforward to the ganglion cells through the amacrine cells. This indirect path gives rise to the increased response complexity from photoreceptor cells to bipolar cells to ganglion cells; and even along the direct path, the neural responses are in fact not passively relayed but increased in complexity.

Along the direct path, the photoreceptor cells output the neural signal, the excitatory neurotransmitter glutamate, to bipolar cells. The effect of this same signal, however, differs for different bipolar cells, depending on the type of receptor embedded on cell membrane. Upon the binding of glutamate, metabotropic receptors will hyperpolarize the bipolar cells whereas ionotropic receptors will cause cell depolarization [15, 16]. Therefore, the bipolar cells with metabotropic receptors (ON bipolar cell) are depolarized, and the bipolar cells with ionotropic receptors (OFF bipolar cell) are hyperpolarized by light stimulation. As such, the direct path gives rise to the ON, OFF response diversity of bipolar cells that is absent in photoreceptor cells.

The indirect path, on the other hand, gives rise to the center-surround receptive field organization of bipolar cells that is absent in photoreceptor cells. This center-surround organization arises from the opposition between horizontal cells and photoreceptor cells in the signal they output to bipolar cells [15, 16]. Specifically, the horizontal cells release the inhibitory neurotransmitter GABA, whereas the photoreceptor cells release the excitatory neurotransmitter glutamate, upon light stimulation. As a result, the center-only receptive field of photoreceptor cells and horizontal cells, where the light falling anywhere in the receptive field has the same influence on cell activity, forms the center-surround receptive field of bipolar cells, where the light falling in the receptive field center and that falling in the receptive field surround exerts the opposite influence on cell activity (Figure 1.3). For ON bipolar cells, light stimulation of receptive field center causes cell depolarization and light stimulation of receptive field surround causes cell hyperpolarization; for OFF bipolar cells, the opposite is observed.

The response properties of bipolar cells are relayed and form the center-surround receptive field organization of ON, OFF ganglion cells. However, the responses of ganglion cells are not a mere clone of the bipolar cells. Instead, the graded membrane potential in photoreceptor, horizontal, bipolar cells, is replaced by the action potential in ganglion cells, and the further relay of neural signal in the visual system all takes the form of action potential [8, 9]. Compared to the graded membrane potential, the action potential consumes much less metabolic energy. This advantage is particularly important, since the neural signal from ganglion cells needs to travel a long distance along optic nerve before entering cortical processing. By contrast, the

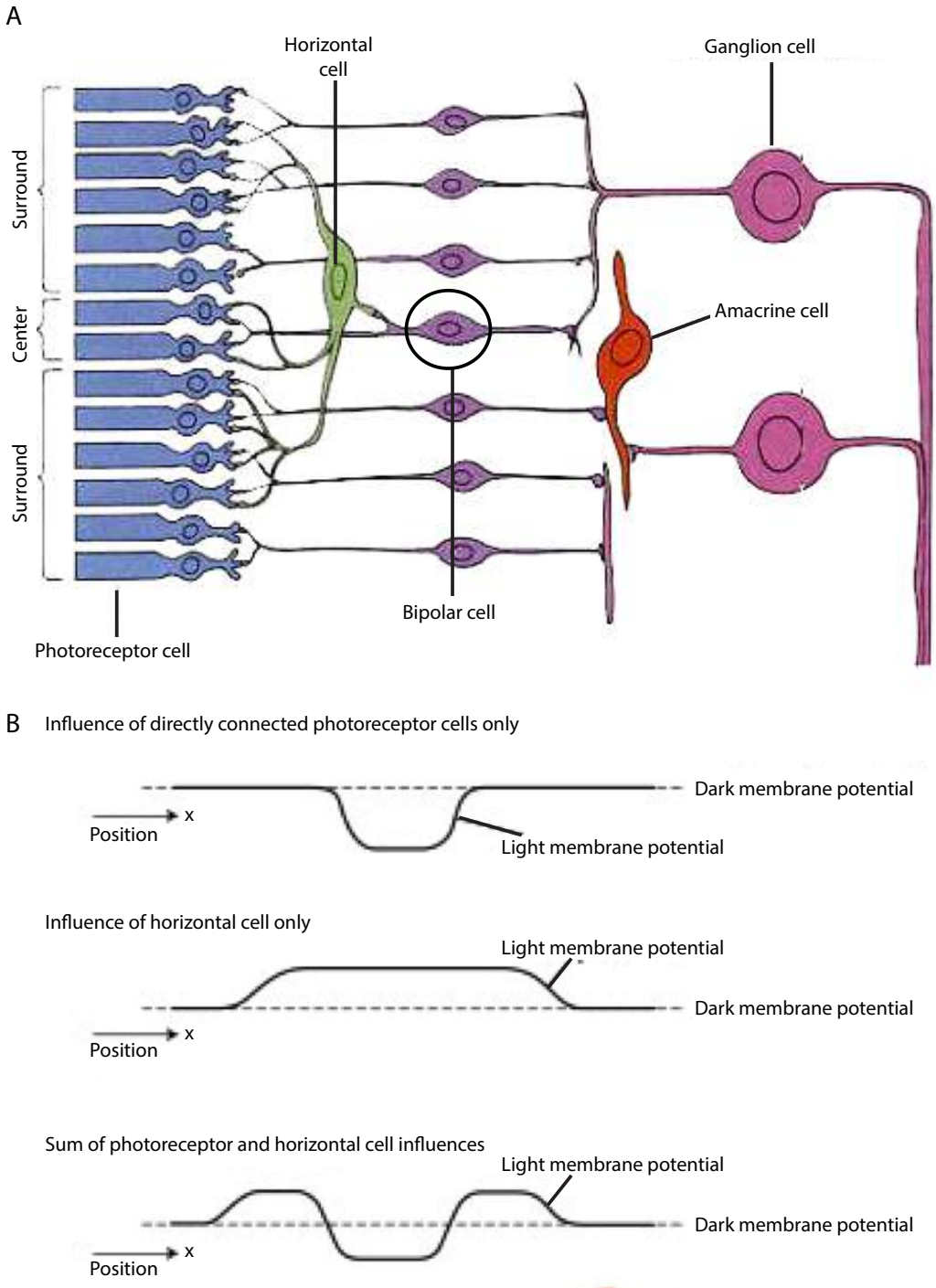

Figure 1.3: Emergence of center-surround receptive field. An example circuit shows how the center-surround receptive field of bipolar cells is formed from the center-only receptive filed of photoreceptor cells and horizontal cells. The receptive field center of an example bipolar cell is built up from a small number of photoreceptor cells that make direct excitatory synaptic contacts with the bipolar cell. The receptive field surround is built up instead from a much larger number of photoreceptor cells that make indirect inhibitory synaptic contacts with the bipolar cell through a horizontal cell. Figure adapted from [7].

travel of neural signal within retina between photoreceptor cells and ganglion cells is short in distance and does not require the form of action potential.

In summary, the retinal processing gives rise to the ON, OFF diversity and the center-surround complexity in receptive field organization. The OFF cells respond to dark (black) in exactly the same way as the ON cells respond to light (white). This duality may appear counter-intuitive at first thought, because we are accustomed to the physics concept that dark is the absence of light. As such, the ON cells that encode light (white) can also encode dark (black), and it would be redundant to have the set of OFF cells specialized for encoding dark (black). However, in nature stimulation, dark (black) is as frequently encountered as light (white). If our visual system were to have only one set of cells that encode the light intensity in the form of membrane potential, more metabolic energy would be needed to cover the natural range of light intensity. Therefore, it is biologically more efficient to have two separate sets of cells that respond to opposing polarity of light. Such design of visual system has interesting consequences for visual perception. Perceptually, dark (black) feels as real and intense as light (white), although physically, dark (black) is the void and light (white) is the full. This discrepancy indicates that our perception is not bounded by the law of physics and is instead created largely by visual neural responses.

The dissociation between the physical and the perceptual is furthered by the center-surround receptive field of bipolar and ganglion cells. Due to their center-surround receptive field organization, the cells do not respond to the absolute level of light intensity but respond to the local gradient in light intensity. This response property renders these cells a good encoder for contour information and a poor encoder for surface information, which in turn improves the efficiency of visual system. Indeed, in nature stimulation, contours, compared to surfaces, tend to occupy less space in visual field yet contain more information of ecological importance. If the responses of bipolar and ganglion cells were to faithfully represent the visual input, the majority of metabolic energy would be wasted on encoding surface information that is of little ecological relevance. This design of visual system has interesting correlates in visual perception. Similar to the responses of bipolar and ganglion cells, perceptually we are insensitive to surface information or to absolute value of light intensity, but sensitive to contour information or to local gradient in light intensity.

Together, the ON, OFF response diversity and the center-surround receptive field complexity of bipolar and ganglion cells suggest that the output of retinal processing contains information far more complex than the point representation of visual input in photoreceptor

cells. In this sense, the retina plays the role of a creative artist rather than a boring photographer. The artwork (retinal processing) seems to follow the principle of minimizing metabolic energy consumption. By so doing, the retina creates a perceptual world that works against the law of physics yet feels as vivid as (or in fact, much more vivid than) the physical reality.

1.3.2 Emergence of feature selectivity

Via retinal processing, the simple neural signal at the layer of photoreceptor cells, where the cell membrane potential represents the visual input in a non-distorted, photograph-like fashion, gives rise to the complex neural signal at the layer of ganglion cells, where the cell firing rate represents the visual input in a distorted, contour-highlighting fashion. This neural signal then travels along the optical nerve, is relayed at lateral geniculate body (LGN), and enters primary visual cortex (V1) for cortical processing [7, 17]. Similar to retina, V1 is composed of interconnected layers, where the optic nerve enters layer 4C of V1. There, the axons divide. The upper half of layer 4C (layer 4Cα) receives axons from the bottom two layers of LGN, which in turn receive inputs from rod cells in retina. The lower half of layer 4C (layer 4Cβ) receives axons from the upper four layers of LGN, which in turn receive inputs from cone cells in retina. The two halves of layer 4C differ not only in their afferent but also in their efferent projections [18, 19, 20, 21]. The upper half of layer 4C (layer 4Cα) projects to layer 4B. The lower half of layer 4C (layer 4Cβ) projects to layer 2 / 3. These different information flow then converge and feedforward to higher visual cortices.

As such, V1 is involved in feedforward visual processing, where layer 4C and layer 2 / 3 / 4B of V1 serve respectively as the input and the output ports [22, 23, 24]. The feedback visual processing, on the other hand, involves layer 5 / 6 of V1, which integrate signals from higher visual cortices with signals from layer 2 / 3 / 4B of V1, and project back to LGN [25]. Clearly, the layering in V1 is far more complex than the layering in retina [26, 27]. In fact, the layering complexity of V1 exceeds that of any other cortical region, including that of higher visual cortices, as illustrated below in the histological image of V1 versus V2 (Figure 1.4). Such anatomical complexity of V1 layering is likely to be driven by V1's unique role as the coordinator between cortical processing and subcortical processing. Correspondingly, the anatomical complexity of V1 layering is accompanied by the physiological complexity of V1 neural responses.

Compared to the neurons in retina or LGN, the neurons in V1 exhibit a much greater diversity and complexity in their responses. Here, the neurons are concerned not just with the

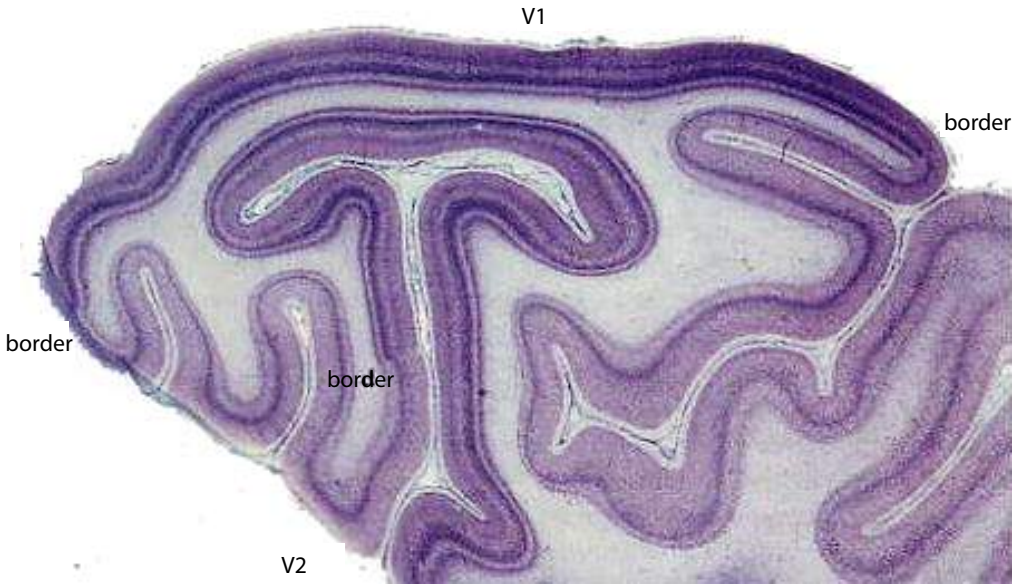

Figure 1.4: Layering of early visual cortex. The Nissl stain of the occipital lobe shows the layering complexity of V1 versus V2. Figure adapted from [7].

visual field location of the stimulus, as the neurons in retina or LGN do, but also with the orientation, length, eye-of-origin, and possibly other features of the stimulus [28, 29, 30]. As a result, while a neuron in retina or LGN will respond to any visual stimulus that falls in its receptive field, a neuron in V1 will respond only to the visual stimulus that exhibits certain features apart from falling in its receptive field. Among the features that the neurons in V1 exhibit selectivity for, the most prominent one is the stimulus orientation. Intriguingly, different orientation-selective V1 neurons differ, not just in the stimulus orientation that they respond optimally to or the visual field location of their receptive field, but in the way that they behave. The behavior of orientation selectivity can be divided into two categories (simple, complex): the complex neurons respond to any optimally oriented stimulus, as long as the stimulus is in their receptive field; by contrast, the simple neurons respond only when the optimally oriented stimulus is placed at certain location in their receptive field [7, 31]. In this sense, the complex neurons, compared to the simple neurons, have higher degree of invariance in their orientation selectivity.

The two categories of orientation-selective neurons are not evenly distributed across V1 layers. Instead, layer 5 / 6 of V1 contains only the complex neurons, whereas layer 2 / 3 / 4B of V1 contains both categories [31]. The neurons in layer 4C of V1, on the other hand, inherit their responses directly from the neurons in LGN, and as such, lack any feature selectivity but have center-surround receptive field. This increase in response complexity from layer 4C to

layer 2 / 3 / 4B to layer 5 / 6 suggests that the feature selectivity of V1 neurons emerges from feedforward visual processing [32, 33, 34]. Indeed, when a neuron receives its inputs from a set of non orientation-selective neurons that have aligned receptive field, this neuron would develop simple, non-invariant orientation selectivity (Figure 1.5A). Similarly, when a neuron receives inputs from a set of simple orientation-selective neurons that have identical orientation selectivity but different receptive field, this neuron would develop complex, invariant orientation selectivity (Figure 1.5B).

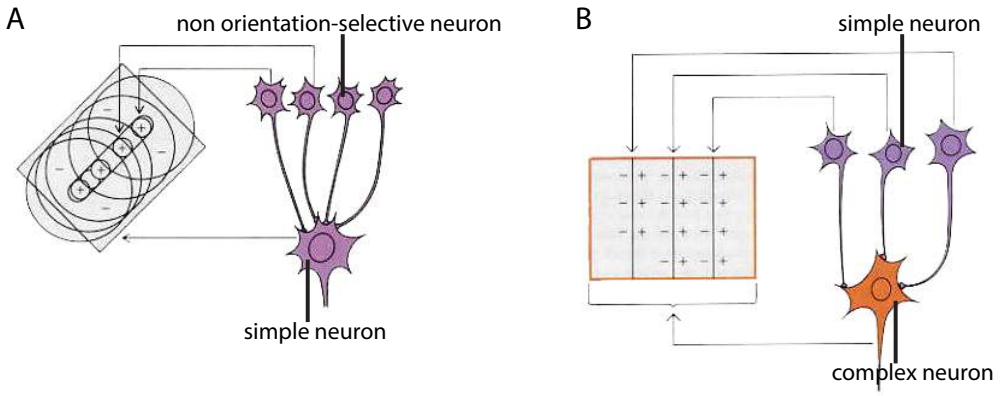

Figure 1.5: Emergence of orientation selectivity. Two example circuits show how the orientation selectivity of simple neuron (A) and complex neuron (B) is formed via feedforward visual processing. The simple neuron receives feedforward inputs from a group of non orientation-selective neurons whose receptive field lies along a line (A), and the complex neuron receives feedforward inputs from a group of simple neurons that have identical orientation selectivity but different receptive field (B). As a result, the simple neuron exhibits non-invariant orientation selectivity and responds only when the optimally oriented stimulus is placed at certain location in its receptive field, whereas the complex neuron exhibits invariant orientation selectivity and responds to any optimally oriented stimulus that falls in its receptive field. Figure adapted from [7].

This example of orientation selectivity illustrates how the visual cortical neurons are able to extract visual features and respond selectively to extracted features, through feedforward visual processing. Via similar mechanisms, the visual cortical neurons get to develop selectivity for visual features with progressive levels of abstraction and complexity along cortical hierarchy [35, 36]. For example, whereas the neurons in V1 respond to rather simple visual features such as orientation, the neurons in V2 start to exhibit selectivity for more complex visual features such as disparity, and the neurons higher up respond to even more complex visual

features such as faces and objects.

Therefore, the feedforward visual processing, mediated by the vertical connections between cortical layers, gives rise to the feature selectivity of visual cortical neurons. Yet, the visual cortical neurons are interconnected not only by vertical connections between cortical layers, but also by lateral connections within cortical layers [7, 37, 38]. These lateral connections play an important role in modulating the feature selectivity of visual cortical neurons. Specifically, the lateral inhibitory connections ensure that the visual cortical neuron does not respond to visual features other than the one that it exhibits selectivity for. Such lateral inhibition, in turn, sharpens the feature selectivity of visual cortical neurons. Intriguingly, within each cortical layer, the visual cortical neurons are distributed in an orderly fashion where neighboring neurons exhibit selectivity for similar (but not identical) visual features [39, 40, 41, 42, 43]. Consequently, the lateral inhibition is able to take place locally between neighboring neurons, and does not require the development of long-distance lateral connections. As such, the orderly distribution of visual cortical neurons facilitates the sharpening of feature selectivity and saves the materials of cortical connections.

In summary, via cortical processing, the center-surround receptive field of retina and LGN neurons gives rise to the feature selectivity of visual cortical neurons. As a result of such feature selectivity, a stimulus in the visual field will activate only a fraction of all the visual cortical neurons whose receptive field it falls in. Moreover, the more complex the stimulus is, the larger fraction of neurons it will activate. For example, a face stimulus will activate not only the object-selective neurons in high-level visual cortices that respond to the face identity, but also the orientation-selective neurons in low-level visual cortices that respond to the face contours; by contrast, an oriented line will activate only the orientation-selective neurons in low-level visual cortices. Such a match between the level of stimulus complexity and the number of activated neurons allows the visual system to encode the maximum amount of visual information with the minimum spent of metabolic energy. In this sense, the feature selectivity, similar to the center-surround receptive field, results naturally from the visual system's tendency to maximum its energy efficiency, and results naturally in the diversity and complexity of visual neural responses. It is due to such emergence of response diversity and complexity that the seemingly identical neural signals from phototransduction get to produce radically different perceptual experiences.

1.4 Exploring the neurobiological basis of perceptual variability

Our existing knowledge of the visual system, as discussed above, suggests that the external light signal generates the internal perceptual experience via a chain of visual processing, including transduction of light signal into neural signal by photoreceptor cells, development of center-surround receptive field at retina, and emergence of feature selectivity in visual cortices. These visual processing gives rise to the diversity and complexity of visual neural responses, which in turn enable the induction of rich perceptual experience from the seemingly simple light signal, and the induction of different perceptual experience in different individuals.

As such, inter-individual differences in perceptual experience are likely to arise neurobiologically from inter-individual variability in visual processing. Inter-individual variability in visual processing, on the other hand, may have its basis in visual cortical anatomy. In essence, the cortex is a tissue sheet that is anatomically composed of interconnected layers, and morphologically characterized by cortical thickness and cortical surface area. The visual cortical processing takes place via the intracortical connections that run vertically between cortical layers and laterally within cortical layers. The vertical connections and the lateral connections, in turn, scale with the cortical thickness and the cortical surface area [44, 45]. Therefore, the two morphological dimensions, the thickness and the surface area, of visual cortices, may get to affect visual processing via their covariance with intracortical connections.

In this sense, inter-individual differences in visual perception may arise ultimately from inter-individual variability in visual cortical anatomy. Indeed, parallel to inter-individual variability in subjective visual perception, the objective visual cortical anatomy also exhibits a substantial degree of variability. For example, the size of early visual cortices (V1, V2, V3) varies across healthy human adults over three-fold and is regulated by a set of genes including GPCPD1 and MECP2 [46, 47, 48, 49, 50]. Moreover, the two dimensions of cortical anatomy, the cortical surface area and the cortical thickness, are modulated by independent genetic factors [46, 51, 52, 53, 54, 55, 56, 57, 58]. The genetic independency between cortical surface area and cortical thickness is predicted by radial unit hypothesis, which suggests that the cortical surface area is dependent on the proliferation of cortical columns whereas the cortical thickness is dependent on the cell divisions within the cortical column [46].

As such, the origin of anatomical variability is relatively well studied. By contrast, the consequence of anatomical variability is less studied. It remains unclear whether the variability in visual cortical anatomy serves any function, perceptually or neurally. Possibly, as

a natural consequence of genetic variability, the visual cortical anatomy exhibits a substantial degree of inter-individual variability, which gives rise to inter-individual differences in visual cortical processing that shapes visual perception. In my thesis, I explore the contributions of visual cortical processing and visual cortical anatomy to inter-individual perceptual variability, with a particular focus on primary visual cortex (V1). This choice of focus is motivated by the recent advances in magnetic resonance imaging (MRI), which offer a fine measure for human V1, including the delineation of V1 boundary, the characterization of V1 morphology, and the estimate of V1 intracortical connectivity. While these measures are still at the macro-level, neurophysiology studies on animal models have revealed the micro-level anatomy and function of V1, which allow one to link the macro-level observations with the micro-level mechanisms. By contrast, our knowledge about higher visual cortices remains rather limited, both at the micro-level and at the macro-level.

I began my thesis by studying the extent to which perception of elementary visual features (orientation, visual field location, contrast, luminance) varied across healthy human adults (Chapter Three). I then studied how such inter-individual variability in subjective visual feature perception related with objective visual cortical anatomy, and specifically, with the surface area (Chapter Four) and the thickness (Chapter Five) of early visual cortices. Based on these empirical observations, I applied computational model to examine whether the relationships between visual feature perception and visual cortical anatomy were in fact mediated by the scaling of intracortical connections (Chapter Six). The computational model suggested that the scaling of intracortical connections affected the feature selectivity of visual cortical neurons that in turn mediated the relationships between visual feature perception and visual cortical anatomy. These predictions from the computational model were tested empirically, where I explored the dependence of neural feature selectivity on visual cortical anatomy (Chapter Seven) and the dependence of visual feature perception on intracortical connections (Chapter Eight).

Taken together, my thesis revealed that the individuality in visual feature perception arose from inter-individual differences in visual cortical anatomy, where the links between visual cortical anatomy and visual feature perception were built gradually through intracortical connections and neural feature selectivity. My thesis involved a combined approach of psychophysics, in-vivo MR imaging, in-vitro histological imaging, and computational modeling. In the next chapter (Chapter Two), I review how recent advances in MR imaging have allowed a fine measure of visual cortical anatomy and visual cortical processing.

Chapter 2

General Method

2.1 The hardware: acquisition of magnetic resonance image

2.1.1 MRI scanner composition

To study the neurobiological basis of inter-individual variability in visual perception, it is essential to acquire a noninvasive measure of human visual cortices. This is made possible by the invention of magnetic resonance imaging (MRI), a radiology technique that measures the anatomy and the physiology of a tissue sample (e.g., visual cortices) in vivo through the application of magnetic fields and radio waves [59]. In the field of cognitive neuroscience, MRI is widely applied to acquire the noninvasive MR image of brain anatomy and brain activity [60]. Before discussing how knowledge of visual cortices can be gained from the analysis of MR image (the software), I will first discuss how the MR image is acquired from the MRI scanner (the hardware).

The basic parts of a MRI scanner include a superconducting magnet that generates a static magnetic field, two radiofrequency coils (transmitter coil, receiver coil) that collect the MR signal, three gradient coils (X-gradient coil, Y-gradient coil, Z-gradient coil) that provide the spatial information for the MR signal, and several shimming coils that ensure the uniformity of the magnetic field [61]. The superconducting magnet generates a strong, static magnetic field that aligns the atomic nuclei in the tissue sample and results in their equilibrium state. The radiofrequency transmission coil, on the other hand, generates a radiofrequency pulse at the resonant frequency of the atomic nuclei that perturbs their equilibrium state. This process, during which the atomic nuclei absorb the radiofrequency energy and break the equilibrium state, is known as excitation [62]. When the radiofrequency pulse ends, the atomic nuclei return to the equilibrium state and release the absorbed energy. The released energy is received by the

radiofrequency receiver coil and forms the MR signal.

The MR signal alone does not contain any spatial information of which location in the space that the signal comes from, and cannot be used to form the MR image. The gradient coils, which generate the spatial variations in the magnetic field, provide the spatial information needed for imaging [61]. In essence, the gradient coils cause the MR signal to become spatially dependent in a controlled manner where different locations in the space contribute differently to the MR signal [63]. This spatial information can then be reconstructed from the MR signal using the Fourier transform [64]. To make the image reconstruction as simple as possible, three gradient coils are typically applied where each gradient coil generates the spatial variation in the magnetic field along one single direction (X, Y, Z). For the accuracy of image reconstruction, the spatial variation generated by the gradient coils needs to be linear, and the magnetic field generated by the superconducting magnet needs to be homogeneous. However, these are rarely the case in reality, and the shimming coils are applied to compensate for the spatial inhomogeneity in the magnetic field [61].

In summary, the four parts of a MRI scanner, the superconducting magnet, the radiofrequency coils, the gradient coils, and the shimming coils, work together to produce the MR signal containing spatial information of brain anatomy and brain activity. The signal quality is dependent on the amount of radiofrequency energy transmitted and received, which is in turn dependent on the distance between the radiofrequency coils and the tissue sample. Typically, the radiofrequency coils are placed either adjacent to the scalp surface on the brain-region-of-interest (surface coil) or further from the scalp surface surround the entire brain (volume coil). The surface coil offers a high signal quality but has a poor spatial coverage. The volume coil, by contrast, provides a uniform coverage for a large tissue volume but is traded-off by a poor signal quality.

2.1.2 MRI image formation

To understand how exactly the MR image is formed [65], it is necessary to explain the physics underlying the MR signal and introduce the concept of nuclear spin. The spin is a type of angular momentum that is carried by the atomic nuclei. Under natural condition, the thermal energy causes the atomic nuclei to spin about itself. By contrast, the application of an external magnetic field causes the spins to exhibit rapid gyroscopic precession around the axis parallel to the magnetic field (the longitudinal direction) and in the plane orthogonal to the magnetic field (the transverse plane). If the external magnetic field is static, such as the

one generated by the superconducting magnet, each spin will adopt either a low-energy state or a high-energy state, and the net magnetization across all spins will be along the longitudinal direction. If instead, a radiofrequency pulse is applied, such as the process of excitation, the net magnetization will be tipped from the longitudinal direction into the transverse plane. Once the radiofrequency pulse ends, the net magnetization will recover from the transverse plane to the longitudinal direction.

These physical processes can be captured by a single formula [66], known as the Bloch equation.

$$dM/dt = \gamma M(B_0 + B_1 + G) + (M_0 - M_z)/T_1 - (M_x + M_y)/T_2 \tag{2.1}$$

In the equation, B_0 denotes the static magnetic field generated by the superconducting magnet, B_1 denotes the radiofrequency field generated by the radiofrequency coils, G denotes the spatially varying magnetic field generated by the gradient coils, and M denotes the net magnetization. The net magnetization M can be broke down into the transverse component $(M_x + M_y)$ that is orthogonal to the magnetic field, and the longitudinal component M_z that is parallel to the magnetic field. Following the excitation process where the net magnetization is tipped from the longitudinal direction into the transverse plane, the longitudinal magnetization is zero and the transverse magnetization is maximum. The recovery of longitudinal magnetization from zero to maximum is governed by time constant T_1, whereas the decay of transverse magnetization from maximum to zero is governed by time constant T_2.

Such decay of transverse magnetization $(M_x + M_y)$ is detected by the radiofrequency receiver coil and forms the MR signal. However, because the MRI scanner does not have separate receiving coils for individual voxels but has only one receiver coil, the MR signal reflects the transverse magnetization summed across all voxels in the tissue volume and contains no spatial information about the contribution of different voxels in the tissue volume [61]. Due to the lack of such spatial information, the MR signal on its own cannot form the MR image. The formation of MR image requires the application of spatially varying magnetic gradients generated by the gradient coils [63]. Specifically, three gradient coils, X-gradient coil, Y-gradient coil, Z-gradient coil, are used together to create magnetic gradients along X, Y, and Z directions, respectively. The three gradient coils cause the static magnetic field to vary across the body, so that different spatial locations are associated with different precession frequencies. Such spatial information is then encoded in K-space representation of MR signal, and is converted

into spatially informative MR image through Fourier transform [64].

In summary, the formation of MR image takes place via the joint efforts of the radiofrequency pulse generated by the radiofrequency coils and the spatially varying magnetic gradients generated by the gradient coils. The radiofrequency pulse causes the net magnetization to tip from the longitudinal direction into the transverse plan, and as such, gives rise to the MR signal that can be detected by the radiofrequency coil. The spatially varying magnetic gradients cause different voxels in the tissue volume to have different contribution to the MR signal, and as such, enable the encoding of spatial information in the MR signal. Through the Fourier transform, this spatial information is extracted from the MR signal and forms the MR image.

2.1.3 MRI contrast selection

The series of radiofrequency pulses and spatially varying magnetic gradients used by the MRI scanner is known as a pulse sequence [67], which determines the type of MR image being acquired. In this sense, the MR image is not a photograph of the tissue sample per se but is instead a spatial map depicting some properties related with the spins in the tissue sample [59, 60]. Depending on the exact pulse sequence used, the MR image can be acquired where the image intensity reflects specific tissue properties such as the density of the spins or the rate of change in the net magnetization, and the image contrast distinguishes between specific tissues types such as between low proton density and high proton density or between gray matter and white matter. The design of pulse sequence for capturing the tissue-property-of-interest constitutes the concept of MR contrast selection. Typically used in the field of cognitive neuroscience are the T1- or T2-contrast MR image that reveals the brain anatomy, and the blood-oxygen-level dependent (BOLD) MR image that reveals the brain activity.

To reveal the brain anatomy, the T1- or T2-contrast MR image relies on the differences across brain tissues (gray matter, white matter, cerebrospinal fluid) in the magnetization change after the excitation process where the net magnetization is tipped from the longitudinal direction into the transverse plane [59]. Specifically, the T1-contrast MR image measures the differences across brain tissues in the recovery of longitudinal magnetization, whereas the T2-contrast MR image measures the differences across brain tissues in the decay of transverse magnetization. In the T1-contrast MR image, the gray matter has medium intensity (appears as gray), the white matter appears has high intensity (appears as white) and the cerebrospinal fluid has low intensity (appear as black). In the T2-contrast MR image, the gray matter has medium intensity (appears as gray), the white matter has low intensity (appears as black), and

the cerebrospinal fluid has high intensity (appears as white).

To reveal the brain activity, the blood-oxygen-level dependent (BOLD) MR image relies on the consumption of metabolic energy by the information-processing activity of neurons [68, 69]. Specifically, the BOLD signal measures the change in magnetic properties of water molecules that reflects the influence of paramagnetic deoxyhemoglobin, while deoxyhemoglobin is itself a physiological correlate of oxygen consumption that is in turn driven by the neural activity (Figure 2.1). The exact neurovascular events that link the neural activity to the hemodynamic activity are as follows [70]. The activity of neurons consists of the change in membrane potential and the release of neurotransmitter, both of which is supported by the movements of ions across neural membrane. The restoration of ions concentration level following the neural activity consumes most of the brain's metabolic energy. Such metabolic energy is supplied to the active neurons in the form of adenosine triphosphate (ATP). However, since the brain does not store metabolic energy, it has to synthesis ATP on site through the oxidation of glucose, and both oxygen and glucose are carried by the increased blood flow. Such increase of blood flow and oxygen delivery flushes deoxyhemoglobin from blood vessels. Because deoxyhemoglobin molecules generate magnetic field gradients that alter the spins of nearby water molecules, the displacement of deoxyhemoglobin in turn leads to a local increase in MR signal. This chain of neurovascular events allows the inference of neural activity, which is difficult to measure noninvasively in human participants, from the MR image of hemodynamic activity.

In summary, the choice of multiple image contrast or multiple pulse sequence renders magnetic resonance imaging an extremely versatile technique. Using it, noninvasive brain image can be acquired that emphasize contrast due to different tissue properties. This in essence allows the same MRI scanner to serve different purposes and reveal different aspects of the brain. In particular, the MRI scanner can be used to reveal the brain anatomy, based on the differences across brain tissues in the magnetization change after the radiofrequency excitation, or to reveal the brain activity, based on the local displacement of paramagnetic deoxyhemoglobin induced by neural activity.

2.2 The software: analysis of magnetic resonance image

2.2.1 Delineation of visual cortical boundary

As discussed above, the MRI scanner allows the acquisition of MR image that reflects the brain activity or the brain anatomy. However, the MR image on its own cannot reveal much

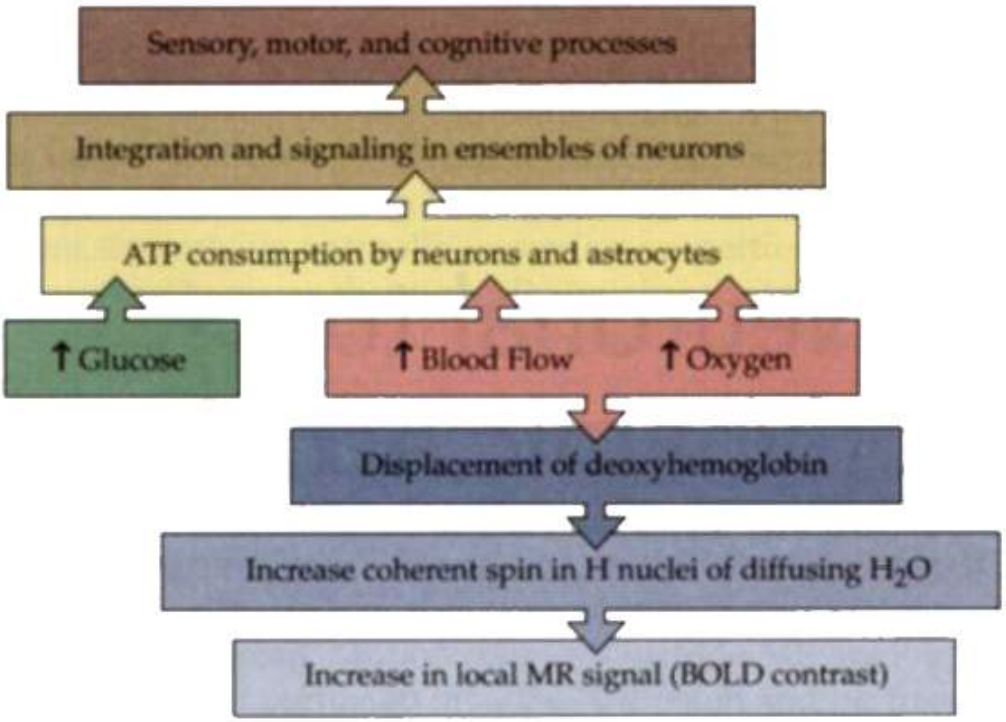

Figure 2.1: Relationship between neural signal and MR signal. Illustrated here is the chain of neurovascular events that link the underlying neural activity, which is difficult to measure in human participants, to the hemodynamic activity, which can be measured noninvasively from the MR BOLD signal. Figure adapted from [59].

about either visual cortical processing or visual cortical anatomy. To gain a deep understanding of visual cortices from the MR image, one needs the appropriate experiment paradigm and the corresponding data analysis method. I will therefore discuss how the recent advances in MRI have provided us with such techniques, beginning from the noninvasive delineation of visual cortical boundary. Indeed, before being able to measure any properties of visual cortices, the boundaries of visual cortices need to be delineated accurately. As such, the noninvasive delineation of visual cortical boundary forms the basis of any further visual cortical measures.

The delineation of visual cortical boundary is based on the orderly representation of visual field in visual cortices, where cortically adjacent neurons respond to spatially adjacent visual field locations [71, 72, 73, 74]. The orderly representation is known as retinotopic map, meaning the map of retina. In essence, the retinotopic map reflects the hierarchy of visual processing, where the retina that resides at the bottom of visual hierarchy feedforwards its orderly representation of visual field to the rest of visual system. As a result, each visual cortex, low-level or high-level, contains a retinotopic map whose boundary defines the visual corti-

cal boundary [74, 75, 76, 77]. This property, in turn, allows the delineation of visual cortical boundary from the measure of retinotopic map.

The retinotopic map is typically measured with respect to two orthogonal dimensions, polar angle and eccentricity, that defines polar coordinate. Since its invention, the phase-encoded method has served as the standard paradigm for retinotopic mapping in human participants [71]. This method measures for individual visual cortical location (e.g., voxel), the visual field location that elicits its largest response. In the experiment, two types of periodic visual stimuli are used. The first stimulus, designed to elicit each voxel's preferred polar angle, is a high-contrast, flickering, wedge-shape checkerboard that spans the fovea to periphery along a small range of specific polar angles, and rotates either clockwise or counterclockwise around the central fixation (Figure 2.2A). The second stimulus, designed to elicit each voxel's preferred eccentricity, is a high-contrast, flickering, ring-shape checkerboard that spans a small range of specific eccentricities, and expands or contracts along fovea to periphery (Figure 2.2B).

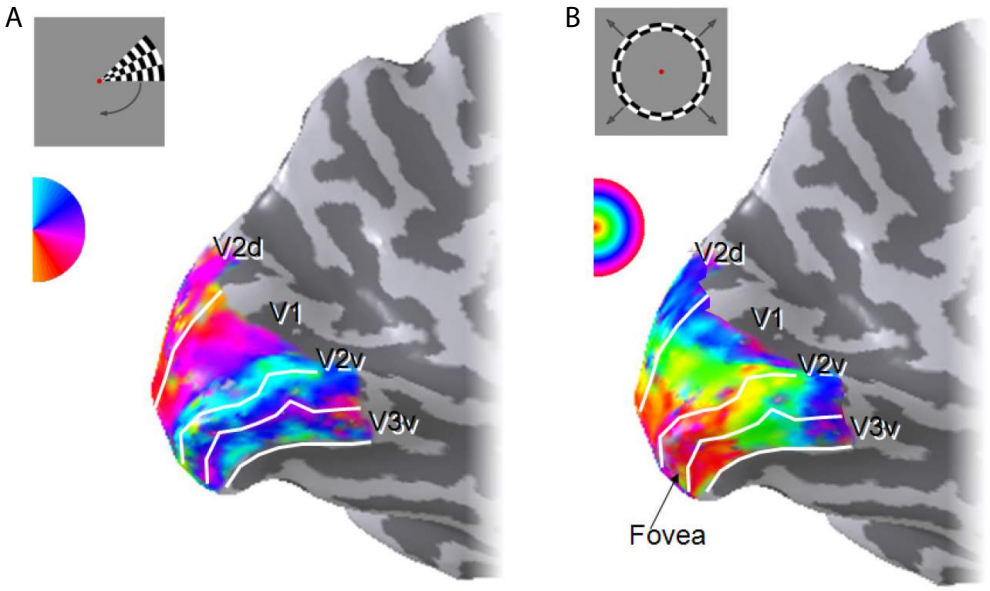

Figure 2.2: Delineation of visual cortical boundary. To delineate the boundaries between early visual cortices (V1, V2, V3), the method of phase-encoded retinotopic mapping is typically applied. In the method, a set of high-contrast, flickering, checkerboard patterns cycle through the visual field along iso-eccentricity (A) or iso-polar-angle (B) lines. This reveals for individual visual cortical location, its preferred polar angle (A) and its preferred eccentricity (B). From the retinotopic map of polar angle preference, the boundaries between early visual cortices are delineated as the mirror reversals in the polar-angle gradient. Figure adapted from [74].

In a single experiment run, only one stimulus is presented, and the visual field is cycled

through several times with this stimulus. Such cycling creates a travelling wave of cortical activity that travels from one end of retinotopic map to the other end, along the iso-eccentricity or the iso-polar-angle lines (Figure 2.2). Thus, the phase of the peak response varies smoothly across the visual cortical surface, and this phase defines the preferred polar angle or the preferred eccentricity for individual voxel. Such encoding of preferred visual field location in the phase of cortical response gives the method the name of phase-encoded reinotopic mapping. Notably, the phase-encoded method is not only capable of revealing the retinotopic organization of visual cortices, but also ensures that only the retinotopically-organized cortical regions get activated. As such, the retinotopic map has a high signal-to-noise ratio, which in turn enables the accurate localization of visual cortices.

To visualize the reinotopic map, a color-coded scheme is usually applied where the color represents the preferred polar angle or the preferred eccentricity. As illustrated in the color-coded eccentricity map (Figure 2.2B), the foveal representation of early visual cortices (V1, V2, V3) is positioned at the occipital pole, with more peripheral representation extending progressively into more anteromedial cortex and forming an eccentricity gradient. The color-coded polar-angle map (Figure 2.2A), on the other hand, illustrates the topological relationship between early visual cortices. In particular, V1 has a contiguous polar angle gradient that represents the full hemifield, whereas both V2 and V3 are constituted of split polar angle gradients that bound V1 dorsally or ventrally (V2d, V2v, V3d, V3v) and represent the lower or upper visual quarterfield. Thus, the boundaries between V1, V2, V3 can be delineated according to the mirror reversals in the polar-angle gradient [71].

In summary, the retinotopic organization of visual cortices, where the visual cortical neurons that respond to adjacent visual field location are also adjacent on the cortical surface [73, 74], allows the delineation of visual cortical boundary from the retinotopic map. To acquire the retinotopic map, the phase-encoded method is standardly applied where a periodic visual stimulus moves smoothly in the visual field along iso-eccentricity or iso-polar-angle lines. This reveals for individual visual cortical location, its preferred visual field location, defined in polar coordinate by eccentricity and polar angle. Based on the retinotopic map of polar angle preference, the boundaries of early visual cortices (V1, V2, V3) are delineated as the mirror reversals in the polar-angle gradient.

2.2.2 Characterization of visual cortical morphology

Using the method of phase-encoded retinotopic mapping, the boundaries of early visual cortices (V1, V2, V3) can be delineated accurately yet noninvasively from the MR image of brain activity. This allows the measure of cortical morphology (cortical thickness, cortical surface area) for the delineated visual cortices, from the MR image of brain anatomy. However, the original MR image of brain anatomy, acquired directly from the MRI scanner, is in the three-dimensional volume space. Yet, the cerebral cortex is a two-dimensional, highly folded tissue sheet [46], whose morphology can only be properly measured in the two-dimensional surface space. In order to measure the human visual cortical morphology, it is essential to reconstruct the two-dimensional surface representation from the three-dimensional volume data, for individual participants in an automated analysis.

The reconstruction of two-dimensional cortical surface is a complex task that requires the solution to a number of subtasks, such as intensity normalization, skull stripping, spatial filtering, tissue segmentation, and surface deformation. Such tasks are made soluble by the recent advances in MRI analysis, and the solutions are implemented in software such as Freesurfer [78, 79]. Specifically, the surface-based analysis in Freesurfer involves tissue segmentation (where the original MR image of brain anatomy is segmented into different brain tissues), surface reconstruction (where the cortical surface is reconstructed from the tissue segments), and morphology calculation (where the cortical thickness and the cortical surface area is calculated from the surface reconstruction).

First, the raw MR image of brain anatomy goes through intensity normalization that compensates the influence of inhomogeneous magnetic field, and skull stripping that removes extracerebral voxels. The pre-processed image is then segmented into different brain tissues (gray matter, white matter, cerebrospinal fluid) using a procedure that combines intensity-based tissue classification and plane-of-least intensity variance detection. Based on the prior information that the locally planer structure sits on the border between different tissues, the plane-of-least variance detection complements the intensity-based classification by resolving the classification of voxels with ambiguous intensity. The series of tissue segmentation procedure overcomes the common problems of partial volume, radiofrequency field inhomogeneity, and magnetic susceptibility artifacts.

After the tissue segmentation, the two cerebral hemispheres are partitioned and any interior holes in the white matter segments are filled, resulting in a single filled white matter

segment for each hemisphere. Then, this white matter segment is covered with triangular tessellation that produces smooth triangle-mesh representations of the white and the pial surfaces with subvoxel accuracy. A triangle-mesh is a collection of vertices (points), edges (connections between vertices) and triangle faces (closet sets of three edges) that defines the shape of a three-dimensional object in geometric modeling. Two triangle faces are used to represent each voxel face (i.e., square face) at the white / gray matter border, and the resulting triangle tessellation is smoothed with deformable surface algorithum to reconstruct the white and the pial surfaces. Notably, because the size of a single MRI voxel is smaller than the cortical thickness, the trillinear interpolation used in deformable surface algorithm allows the cortical surface to be reconstructed with subvoxel and submillimeter accuracy.

From the surface reconstruction, the cortical thickness is computed as the vertical distance between the white and the pial surfaces for individual location (vertex) in a cortical region, while the cortical surface area is computed as the summed surface area of all triangle faces in a cortical region. To enable such morphology calculation, a surface-based coordinate system is built by transforming the convoluted cortical surface into a spherical surface. The use of a spherical surface allows the preservation of the topological structure (local connectivity) in the original cortical surface. This is in contrast to the use of a flattened surface, which requires cuts to be introduced prior to flattening. These cuts would change the topological structure of the cortical surface, where the points that are adjacent on the original cortical surface but reside on the opposite sides of a cut would become far apart in the final flattened surface. Yet at the same time, the choice of a spherical surface retains the computational easiness of a flattened space and facilitates the calculation of morphological properties (distances, areas, angles) that are difficult to compute on less symmetric surfaces.

In summary, the characterization of cortical morphology (cortical thickness, cortical surface area) is realized through the automated surface-based analysis implemented in software such as Freesurfer [78, 79]. In the analysis, the original MR image of brain anatomy is segmented into different brain tissues (gray matter, white matter, cerebrospinal fluid). From the gray matter and the white matter segments, the cortical surface is reconstructed as a triangle-mesh, where each vertex of the mesh represents a single cortical location distinguishable by MRI. Based on the cortical surface reconstruction, the thickness at individual visual cortical locations (vertices) and the surface area summed over different visual cortical locations are calculated.

2.2.3 Estimate of visual cortical connectivity

Similar to the measure of visual cortical morphology, the measure of visual cortical connectivity is made possible by the recent advances in MRI analysis, such as the Dynamic Causal Modeling (DCM) analysis. DCM analysis provides a validated measure of effective connectivity, which reflects the directional connectivity from one neural population to another [80, 81, 82]. The concept of effective connectivity is to be distinguished from the better-known concept of functional connectivity, which reflects the statistical dependence between the activities of two neural populations. Effective connectivity and functional connectivity are two empirically dissociable measures suitable for addressing different questions [82, 83, 84, 85, 86].

Specifically, functional connectivity is a descriptive measure of the statistical relationships in the observed data (e.g., BOLD signal) with no inferences about the underlying causes (e.g., neural connectivity). However, the statistical dependence between the activities of two neural populations can arise from confounding causes, such as shared inputs, other than the underlying neural connectivity [82, 83, 84]. By contrast, the concept of effective connectivity originates from the field of single-unit electrophysiology, as an attempt to disambiguate the effects of confounding causes from those induced by the underlying neural connectivity [85, 86]. It refers explicitly to the directional connectivity from one neural population to another, and represents inference of the causes (e.g., neural connectivity) underlying the observed data (e.g., BOLD signal). As such, the measure of effective connectivity rests upon the comparison between different models that hypothesize different causes (e.g., different neural connectivity).

The different nature of the two measures, inferential for effective connectivity and descriptive for functional connectivity, determines the types of questions that each measure is suitable for addressing [82]. The analysis of effective connectivity recapitulates the scientific process of hypothesis testing, where one tests different models, each incorporating a hypothesis of neural connectivity, that are made to explain the observed data. For example, DCM analysis is typically applied to making inferences about the changes in neural connectivity under different experimental conditions such as different visual stimuli, by testing models with or without an effect of experimental manipulation on neural connectivity. In contrast to the inferential nature of effective connectivity, functional connectivity is a descriptive parameter of the statistical relationships in the observed data. In functional connectivity analysis, no hypothesis of neural connectivity is tested; instead, the hypothesis tested is statistical dependency versus no dependency [82]. In this sense, functional connectivity can be used for identifying statistical patterns (e.g., covariance network) in the data, but not for drawing inference about the underlying neu-

ral connectivity.

To make inferences concerning the underlying neural connectivity from the observed BOLD signal, DCM analysis models the links between neural connectivity and BOLD signal via hemodynamic state equations and neural state equations. The hemodynamic state equations describe the neurovascular mechanisms that link the BOLD signal to the neural activity [87], whereas the neural state equations describe how the activity of one neural population is modulated by the directional connectivity from another neural population multiplied by the activity of that neural population [88]. Different models incorporating different hypothesis of neural connectivity are constructed, and Bayesian model comparison is applied to select the model with the highest posterior probability [82, 89].

The posterior probability of a model is a function of its prior probability and its model evidence. The model evidence quantifies the probability of the observed data given the model. It is a reflection of both how accurate the model fits the data (the more accurate, the higher the model evidence) and how simple the model structure is (the simpler, the higher the model evidence). The model evidence can be approximated by Free Energy (FC), Akaike's Information Criterion (AIC), or Bayesian Information Criterion (BIC), and free energy is used in DCM analysis as an approximation to model evidence [90]. The prior probability is specified to indicate prior knowledge about the plausibility of model structure. When there exists no strong prior against or for specific models, different models are given equal prior probabilities and their posterior probability effectively reflects their model evidence. Due to the nature of Bayesian model comparison, the models with implausible structure, even when included in the model space and given the same prior probability as the other models, would be less explanatory of the empirical data and have lower posterior probabilities.

In summary, DCM analysis offers an estimate of effective connectivity, which reflects the casual influence that the activity of one neural population has on another [81, 82]. For this purpose, DCM models implement neural state equations and hemodynamic state equations to link neural connectivity to neural activity and in turn to BOLD signal. Usually, several different models are constructed that incorporate different hypothesis of neural connectivity, and Bayesian model comparison is applied to select the model with the highest posterior probability. Whereas the classical functional connectivity analysis is suitable for describing the statistical relationships in the BOLD signal, the DCM effective connectivity analysis is suitable for making inferences of the neural connectivity underlying the BOLD signal.

Chapter 3

Variability in Visual Feature Perception

3.1 Introduction

Living in the same objective world, we tend to assume that our subjective perception of this world is also more or less similar across individuals. Yet, a close look at many of our perceptual experiences suggests that this is not the case. Individuals differ in their visual perception just as much as they do in higher-level cognitive functions such as memory and decision-making. The topic of perceptual variability is not very well addressed in neuroscience literatures [2, 3], where most studies focus on the commonality in perceptual experiences across individuals and treat inter-individual variability as a pure source of noise. Consequently, not much is known about the extent to which subjective perception of the objective world varies among healthy human adults, and even less is known about the neurobiological basis of such perceptual variability.

In this chapter, I explored perceptual variability in healthy human adults. Given the diversity of visual stimulation in the external environment, visual perception has multiple levels of complexity, ranging from perception of elementary visual features such as luminance and contrast to perception of complicated visual images such as faces and houses. Regardless of the exact complexity level, any given visual stimulation can usually be decomposed into elementary visual features through a combined approach of filtering and independent component analysis [91, 92, 93, 94, 95]. The neural processing of elementary visual features is relatively well studied, allowing one to explore how the variability in subjective perception of elementary visual features stems from the objective neural processing. Therefore, I focused my study on the perceptual variability of elementary visual features.

Different elementary visual features can be divided into different categories according to the neural response patterns. Specifically, the response of visual cortical neurons to orienta-

tion or visual field location is a Gaussian-shaped function where the neural firing rate is the highest for the preferred orientation or the preferred visual field location; moreover, the neural response is arranged in an orderly cortical representation where neurons responding to more similar orientations or more similar visual field locations are more likely to be intracortically connected (Figure 3.1) [37, 38, 43]. Conversely, the response of visual cortical neurons to contrast is a monotonic function where the firing rate increases monotonically with stimulus contrast, and is arranged without any orderly cortical representation (Figure 3.1) [37, 96, 97]. As a third category, visual cortical neurons respond to luminance in a Gaussian-shaped function with no orderly cortical representation (Figure 3.1) [37, 97, 98]. These neural response patterns are largely based on observations in animal models. Nevertheless, limited studies in human participants hint towards similar patterns [41, 71]. The distinct patterns of neural response to different elementary visual features allow one to explore whether perception of these visual features also exhibits different patterns of variability. Therefore, I studied the perceptual variability for a variety of elementary visual features - orientation, visual field location, contrast, and luminance - that covered three different categories of neural response patterns.

Perception of elementary visual features has two key aspects to it - local feature perception, as assessed from visual discrimination of local feature details [2, 99], and global feature perception, as assessed from visual illusion induced by global feature contexts [100, 101, 102]. These two aspects of visual perception correspond very well with two key properties of visual neural response - the response selectivity for local details [36, 38, 43, 96, 98, 103] and the response modulation by global contexts [30, 104, 105, 106, 107]. As such, local and global perception of elementary visual features may very well represent neural-based personal traits, allowing one to explore the neurobiological basis of inter-individual perceptual variability. Therefore, I studied the variability across individuals in local and global perception of orientation, contrast, and luminance.

Local perception of feature details varies not only across individuals, but also within individuals across the visual field, as assessed by the differences in visual discrimination threshold between different visual field locations [99]. The exact pattern of intra-individual perceptual variability, on its own, may be unique for each individual and represent a personalized perceptual fingerprint. This allows one to explore whether intra-individual perceptual variability shares the same neurobiological basis with, or have a different neurobiological basis to, inter-individual perceptual variability. Therefore, apart from studying the variability across individ-

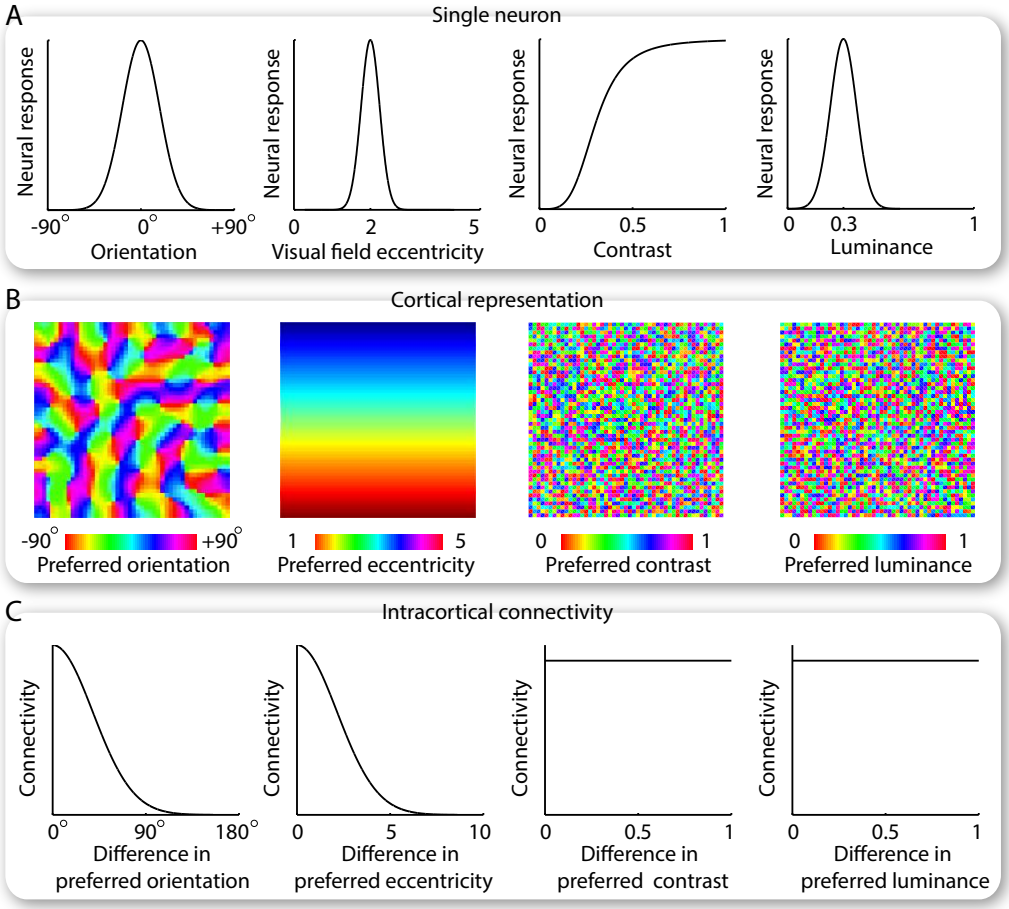

Figure 3.1: Neural response to elementary visual features. Neurons in early visual cortices respond to different elementary visual features in different patterns, where the response is a Gaussian-shaped function for orientation, visual field location, or luminance, and a monotonic function for contrast (A). The cortical representation of neural response also differs across elementary visual features (B). In particular, the orientation preference or the visual field location preference has an orderly cortical representation where intracortical connectivity correlates with the similarity in preferred orientation or preferred visual field location between connected neurons; conversely, the contrast preference or the luminance preference has a randomized cortical representation where there exists no systematic relationship between intracortical connectivity and neural feature selectivity (C).

uals, I also studied the variability within individuals in local perception of visual field location.

Taken together, in this chapter, I explored the perceptual variability in healthy human adults with three specific aims. First, I studied to which extent local and global perception of elementary visual features varied across and within individuals. Then, I tested whether such perceptual variability represented robust personal traits or was dependent on nuisance factors

such as the experimental paradigm. Last, I addressed how the perceptual variability differed between different categories of elementary visual features that had different neural response patterns. To this end, I assessed the variability across individuals in perception of orientation, contrast, and luminance, by measuring the visual discrimination threshold and the contextual illusion magnitude at the visual field center (fovea). I also assessed the variability within individuals in perception of visual field location, by measuring the location discrimination threshold at different visual field locations.

3.2 Methods

3.2.1 Participants and Apparatus

A group of forty-five healthy participants (aged 21 to 35, twenty females, twenty-five males) gave written informed consent to take part in the experiments measuring the perceptual variability across individuals, and a second group of twenty healthy participants (aged 19 to 34, ten females, ten males) gave written informed consent to take part in the experiments measuring the perceptual variability within individuals. All participants had normal or corrected-to-normal vision and no neurological history. All experiments were approved by the UCL ethics committee.

The psychophysics experiments took place in a dark room where the computer monitor provided the only significant source of light. The visual stimuli were presented on the computer monitor and viewed through a chin and forehead rest. For the display, I sought to use a monitor with a high spatial resolution (i.e., a small pixel size) that improved the measurement accuracy, as well as a large visual field coverage that facilitated the measure of intra-individual perceptual variability. However, there is a natural trade-off between the spatial resolution and the visual field coverage of any display. Consequently, I applied two different displays, a 17 inch monitor (size = 34.2 x 27.5 cm, viewing distance = 3 m, resolution = 1280 x 960 pixels) that offered a high spatial resolution (pixel size = 0.005 degree of visual angle) yet a limited visual field coverage (radius = 2.4 degree of visual angle), and a 22 inch monitor (size = 41 x 30.6 cm, viewing distance = 67 cm, resolution = 2048 x 1536 pixels) that offered a large visual field coverage (radius = 12.9 degree of visual angle) yet a limited spatial resolution (pixel size = 0.017 degree of visual angle). I used the 17 inch monitor for the measures at the visual field center, and the 22 inch monitor for the measures at the peripheral visual field.

3.2.2 Inter-individual variability in global feature perception

To assess inter-individual variability in global feature perception, I measured the magnitude of visual contextual illusion for orientation (tilt illusion), contrast (contrast-contrast illusion), and luminance (simultaneous brightness contrast illusion), in separate experiments (Figure 3.2A). Uniform gray stimuli that contained no contrast and no orientation were used in the luminance experiments; low-pass filtered white noise stimuli that contained no orientation and had constant average luminance were used in the contrast experiments; sinusoidal grating stimuli (spatial frequency =1.5 cycles per degree of visual angle) that had constant contrast (full contrast) and constant average luminance were used in the orientation experiments.

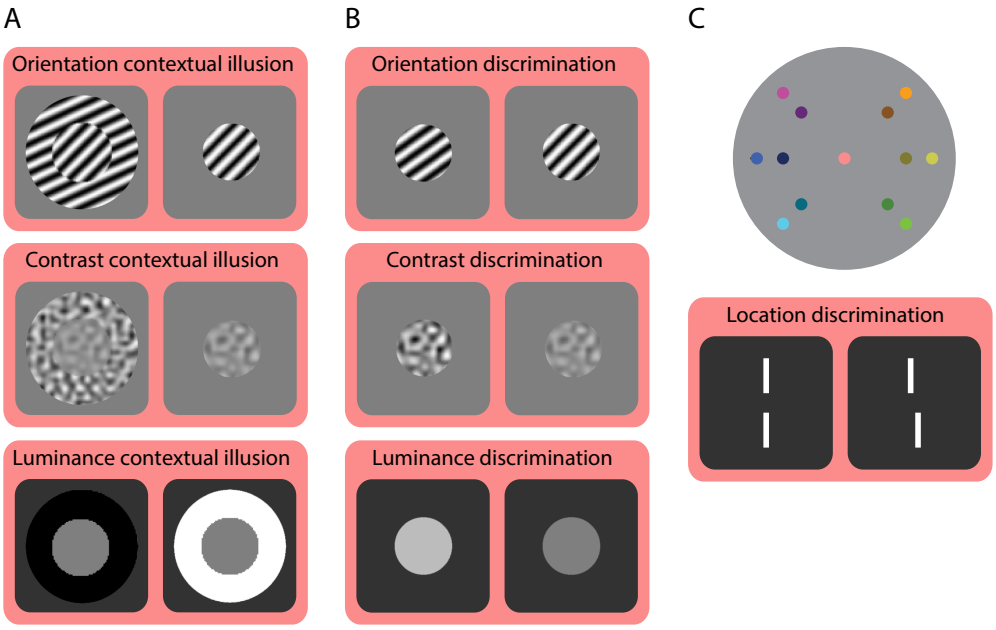

Figure 3.2: Psychophysics measure of perceptual variability. Inter-individual variability in global feature perception was assessed using visual contextual illusion for orientation, contrast, and luminance, in three separate experiments (A). Inter-individual variability in local feature perception was assessed using visual discrimination for orientation, contrast, and luminance, in three separate experiments (B). Intra-individual variability in local feature perception was assessed using visual discrimination for visual field location, in thirteen separate experiments that took place at thirteen non-overlapping visual field locations (C).

The orientation, contrast, and luminance experiments differed only in the visual stimuli and shared the same experiment procedures. Specifically, I used the standard method of constant stimuli with a temporal forced-choice task, where participants judged the parametric difference between two sequentially presented visual stimuli at the visual field center. In a

single experiment trial, two central circular stimuli (diameter = 1.5 degree of visual angle), one with and one without a surrounding annular context (inner diameter = 1.5 degree of visual angle, outer diameter = 6 degree of visual angle), were presented in succession on the computer monitor. The parametric difference between the surrounding context and the central stimulus was optimized to reach the maximum contextual illusion. Specifically, in the orientation experiment, the surrounding context was tilted 15 degree from the central stimulus; in the contrast experiment, the surrounding context had a contrast of 100% and the central stimulus a contrast of 40%; in the luminance experiment, the surrounding context alternated between black and white. The interval (first or second) where the surrounding context appeared was randomized but counter-balanced across trials. The duration of each stimulus was 300 ms and the inter-stimulus-interval was 500 ms. While maintaining central fixation throughout the experiment, participants made an unspeeded forced-choice regarding whether the central stimulus in the second interval, compared with the one in the first interval, was rotated clockwise or anti-clockwise (orientation experiment), had higher or lower contrast (contrast experiment), or had higher or lower luminance (luminance experiment).

Prior to the experiment, each participant performed four trials in which they manually adjusted the orientation, contrast, or luminance of the central stimulus presented in isolation till it matched the perceived orientation, contrast, or luminance of the central stimulus presented in the surrounding context. The parametric difference between the two central stimuli at the point of perceptual equality reflected the adjustment-derived measure of contextual illusion magnitude. In the subsequent experiment, the orientation, contrast, or luminance of the central stimulus presented in the surrounding context was kept constant, while that of the central stimulus presented in isolation was varied around this adjustment-derived point of perceptual equality for seven different parametric values. In a single experiment, a total of 112 trials (16 trials per parametric value) were taken to produce a psychometric curve. The parametric difference between the two central stimuli at the 50% threshold point of the psychometric curve where they appeared perceptually equal reflected the psychometric-derived measure of contextual illusion magnitude. The robustness of contextual illusion measure was addressed by comparing the psychometric-derived measure with the adjustment-derived measure.

3.2.3 Inter-individual variability in local feature perception

To assess inter-individual variability in local feature perception, I measured the threshold of visual discrimination for orientation, contrast, and luminance, in separate experiments (Figure 3.2B). Similar to the visual stimuli used in the contextual illusion experiments, uniform

gray stimuli, low-pass filtered white noise stimuli, and sinusoidal grating stimuli were used for the measure of luminance, contrast, and orientation discrimination threshold, respectively.

The orientation, contrast, and luminance experiments differed only in the visual stimuli and shared the same experiment procedures. Specifically, I used the standard 2-up-1-down staircase procedure with a temporal forced-choice task, where participants judged the parametric difference between two sequentially presented visual stimuli at the visual field center. In contrast to the spatial forced-choice task where participants judge the parametric difference between two concurrently presented stimuli at different visual field locations, the temporal forced-choice task avoids the complication of spatial inhomogeneity between different visual field locations [108]. However, for the measure of orientation discrimination threshold, the application of temporal forced-choice task has the pitfall of confounding orientation discrimination with visual field location discrimination, since participants may in theory use the location of sinusoidal grating stripes as cues for orientation discrimination. Therefore, to test whether the measure of orientation discrimination threshold was robust against the experimental paradigm, I conducted control experiments where I replaced the temporal forced-choice task with a spatial forced-choice task.

For the temporal forced-choice task, in a single experiment trial, two central circular stimuli (diameter = 1.5 degree of visual angle), one with a constant parametric value (45 degree for orientation experiment, 40% for contrast experiment, 50% of the monitor maximum luminance for luminance experiment) and the other a variable parametric value, were presented in succession on the computer monitor. The interval (first or second) where the stimulus with a constant parametric value appeared was randomized across trials. The duration of each stimulus was 300 ms and the inter-stimulus-interval was 500 ms. While maintaining central fixation throughout the experiment, participants made an unspeeded forced-choice regarding whether the second stimulus, compared with the first one, was rotated clockwise or anti-clockwise (orientation discrimination), had higher or lower contrast (contrast discrimination), or had higher or lower luminance (luminance discrimination).

For the spatial forced-choice task, in a single experiment trial, a circle (eccentricity = 6.9 degree) of six sinusoidal grating stimuli (diameter = 2.8 degree of visual angle) was presented twice on the computer monitor. In one presentation, the six gratings were exactly identical, and in the other presentation, one of the six gratings popped-out from the rest by a slightly different orientation. The presentation (first or second) and the location (one of the six) of the pop-out grating were randomized across trials. The duration of each presentation was 200 ms

and the inter-presentation-interval was 500 ms. While maintaining central fixation throughout the experiment, participants made an unspeeded forced-choice judgment regarding whether the first or the second presentation contained the pop-out grating.

The parametric difference between the two successively presented stimuli (temporal forced-choice task) or between the pop-out grating and the rest of the gratings (spatial forced-choice task) was varied in a 2-up-1-down staircase fashion that assessed the threshold value at which the discrimination performance converged to 70.7% correct [109]. Specifically, two consecutive correct answers led to a one-step decrease in the orientation, contrast, or luminance difference in the next trial, whereas one incorrect answer lead to a one-step increase in the parametric difference. The experiment stopped after eighteen reversals, and the discrimination threshold was calculated as the parametric difference averaged over the last ten reversals.

3.2.4 Intra-individual variability in local feature perception

To assess intra-individual variability in local perception, I measured the threshold of visual field location discrimination for each participant at thirteen non-overlapping locations across the visual field through thirteen independent experiments (Figure 3.2C). These thirteen locations covered three eccentricities (0, 4.7, 6.7 degree) and six polar angles (45, 90, 135, 225, 270, 315 degree). Such a distributed coverage of the visual field allowed a comprehensive assessment of intra-individual perceptual variability. I used white bar stimuli that contained no luminance, contrast, or orientation for the measure of location discrimination threshold.

The thirteen experiments differed only in the location of visual stimuli and shared the same experiment procedures. Specifically, I used the standard 2-up-1-down staircase procedure with a spatial forced-choice task, where participants judged the location difference between two concurrently presented bar stimuli (Vernier stimuli). Similar to the study on inter-individual perceptual variability, I conducted control experiments where I replaced the spatial forced-choice task with a temporal forced-choice task, in order to test whether the measure of location discrimination threshold was robust against the experimental paradigm.

For the spatial forced-choice task, in a single experiment trial, one pair of collinear bars and one pair of horizontally offset bars (single bar width = 0.15 degree of visual angle, single bar length = 0.6 degree of visual angle, vertical distance between two bars = 0.3 degree of visual angle) were presented in succession on the computer screen with randomized order. The duration of each bar pair was 300 ms and the inter-stimulus-interval was 500 ms. While maintaining central fixation throughout the experiment, participants made an unspeeded forced

choice regarding which temporal interval contained the pair of horizontally offset bars.

For the temporal forced-choice task, in a single experiment trial, two bars (bar width = 0.15 degree of visual angle, bar length = 1.5 degree of visual angle), one at a constant visual field location and the other a horizontally different visual field location, were presented in succession on the computer monitor with randomized order. The duration of each bar was 300 ms and the inter-stimulus-interval was 500 ms. While maintaining central fixation throughout the experiment, participants made an unspeeded forced-choice regarding whether the second bar, compared with the first bar, was moved horizontally rightwards or leftwards.

The horizontal location difference between the pair of horizontally offset bars (spatial forced-choice task) or between the two successively presented bars (temporal forced-choice task) was varied in a 2-up-1-down staircase fashion that assessed the threshold value at which the discrimination performance converged to 70.7% correct [109]. Specifically, two consecutive correct answers led to a one-step decrease in the horizontal location difference in the next trial, whereas one incorrect answer lead to a one-step increase in the parametric difference. The experiment stopped after eighteen reversals, and the location discrimination threshold was calculated as the horizontal location difference averaged over the last ten reversals.

3.3 Results

3.3.1 Extent of perceptual variability

Across participants, I observed a substantial degree of variability both in the threshold of visual discrimination for local feature details and in the magnitude of visual illusion induced by global feature contexts. Specifically, the orientation discrimination threshold varied inter-individually from 0.73 degree to 7.04 degree, the contrast discrimination threshold from 1.92% to 9.23%, and the luminance discrimination threshold from 1.32% to 6.70%. Such a large degree of inter-individual variability in local perception was surpassed by an even larger degree of inter-individual variability in global perception, where the orientation contextual illusion magnitude varied across participants from 0.48 degree to 14.72 degree, the contrast contextual illusion magnitude from 0.79% to 24.38%, and the luminance contextual illusion magnitude from 1.42% to 35.35%.

Within participants, I observed a substantial degree of variability across the visual field in the threshold of visual discrimination for local location differences. Consistent with previous reports [99], the location discrimination threshold increased intra-individually along the visual

field eccentricity from as small as 0.008 degree of visual angle at the visual field center (fovea), to as large as 0.127 degree of visual angle at the peripheral visual field (6.7 degree eccentricity). Moreover, at the same visual field eccentricity, I found that the location discrimination thresholds still exhibited a two- to three-fold intra-individual variability across different visual field locations. Intriguingly, the exact pattern of intra-individual variability in location discrimination threshold was quite different for different participants. Whereas some participants had a nine-fold increase in their location discrimination threshold from the visual field center to the peripheral visual field, other participants exhibited a less than two-fold increase.

3.3.2 Robustness of perceptual variability

To test whether intra-individual variability in local perception represented robust personal traits, I compared the measures of location discrimination threshold from different experimental paradigms where participants judged the location difference between two concurrently (spatial forced-choice) and sequentially (temporal forced-choice) presented stimuli, respectively. I found that the location discrimination thresholds measured from different experimental paradigms were correlated across participants (r = 0.652, 95% CI = [0.295, 0.849], $p < 0.01$, N = 20 participants), suggesting that the measure reflected trait-like perceptual variability.

To address the robustness of inter-individual variability in local perception, I applied a similar analysis where I compared the orientation discrimination thresholds measured from the spatial and the temporal forced-choice paradigms, respectively. Again, I observed correlation across participants in the measure of orientation discrimination threshold from different experimental paradigms (r = 0.555, 95% CI = [0.150, 0.800], $p < 0.05$, N = 20 participants), suggesting that the measure reflected trait-like perceptual variability. In addition to explicitly comparing different experimental paradigms, I further addressed the robustness of inter-individual variability in local perception using an implicit approach, by deriving the visual discrimination threshold from the slope of psychometric curve acquired in the contextual illusion experiments. Specifically, the parametric difference between the 50% threshold point (pure guess) and the 70.7% threshold point (matching 2-up-1-down staircase) of the psychometric curve reflected the visual discrimination threshold under the presence of the surrounding context. I found that this psychometric-derived, implicit measure and the staircase-derived, explicit measure of visual discrimination threshold were highly correlated across participants in all three experiments - orientation (r = 0.770, 95% CI = [0.616, 0.867], $p < 10^{-9}$, N = 45 participants), contrast (r = 0.470, 95% CI = [0.205, 0.670], $p < 0.001$, N = 45 participants), and luminance (r = 0.420,

95% CI = [0.145, 0.635], $p < 0.005$, N = 45 participants).

These correlations suggested that local perception, as assessed from the threshold of visual discrimination for local details, represented robust personal traits independent of the specific experimental paradigm and the specific stimulus layout. To test whether global perception, as assessed from the magnitude of visual illusion induced by global contexts, also represented robust personal traits, I compared the contextual illusion magnitudes derived from the psychometric curve (method of constant stimuli) and the manual adjustments, respectively. In all three experiments - orientation (r = 0.480, 95% CI = [0.218, 0.678], $p < 0.001$, N = 45 participants), contrast (r = 0.520, 95% CI = [0.268, 0.705], $p < 0.001$, N = 45 participants), and luminance (r = 0.860, 95% CI = [0.758, 0.921], $p < 10^{-13}$, N = 45 participants), I observed significant correlations across participants between the psychometric-derived measure and the adjustment-derived measure of contextual illusion magnitude. This observation demonstrated the robustness of inter-individual variability in global perception.

3.3.3 Relationship between different perceptual variability

The analyses above revealed that local perception of feature details and global perception of feature contexts both exhibited a substantial degree of trait-like variability that was robust against the experimental paradigm. Moreover, the extent and the robustness of perceptual variability were comparable across different categories of elementary visual features. Building upon these observations, I next explored how inter-individual variability in local perception and that in global perception related with each other, and whether such relationship differed between different categories of elementary visual features.

Across participants, I found that the orientation discrimination threshold correlated strongly with the orientation contextual illusion magnitude (Figure 3.3; r = 0.780, 95% CI = [0.631, 0.873], $p < 10^{-8}$, N = 45 participants). By contrast, I did not observe any significant correlation across participants between the contrast discrimination threshold and the contrast contextual illusion magnitude (Figure 3.3; r = 0.03, 95% CI = [-0.27, 0.320], p = 0.82, N = 45 participants), or between the luminance discrimination threshold and the luminance contextual illusion magnitude (Figure 3.3; r = -0.25, 95% CI = [-0.51, 0.046], p = 0.10, N = 45 participants). Moreover, the correlation between the visual discrimination threshold and the contextual illusion magnitude in orientation perception was significantly higher than that in contrast perception ($t(42) = 7$, $p < 10^{-7}$, N = 45 participants) or that in luminance perception ($t(42) = 11$, $p < 10^{-13}$, N = 45 participants).

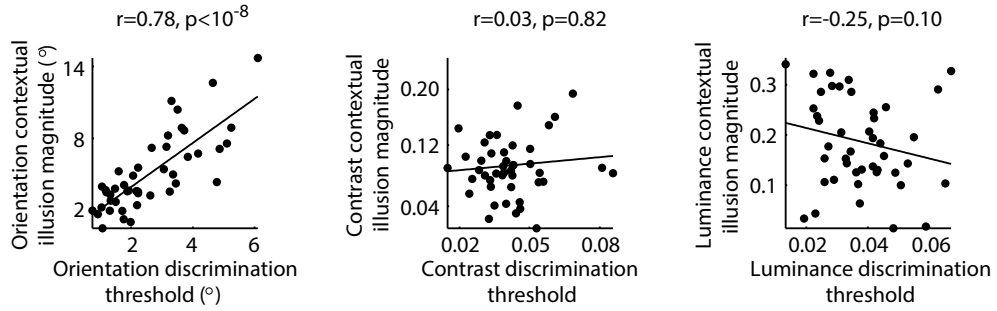

Figure 3.3: Relationship between different perceptual variability. Across participants, the orientation discrimination threshold was plotted against the orientation contextual illusion magnitude, illustrating a trade-off between local and global perception of orientation. For contrast or luminance perception, no such trade-off was observed between the discrimination threshold and the contextual illusion magnitude. Each point represents a single participant (N = 45) and the line is the best-fitting linear regression. Statistical values reflect Spearman's rho with FDR correction for multi-comparisons (α = 0.025).

Thus, there was an inter-individual trade-off between local and global perception of orientation, where individuals who were able to perform finer discrimination of local orientation details tended to experience weaker modulation by global orientation contexts. This trade-off, however, was not observed in perception of contrast or luminance, suggesting that it was not a perceptual phenomenon generalizable across different categories of elementary visual features.

3.4 Discussion

In summary, this study revealed a substantial degree of inter-individual variability in local perception of feature details and global perception of feature contexts, for all three categories of elementary visual features studied - orientation, contrast, and luminance. While the extent of inter-individual perceptual variability was similar across different visual features, local and global perception of orientation exhibited an inter-individual trade-off that was not observed in perception of contrast or luminance. In addition to such inter-individual variability, my study revealed a large degree of intra-individual variability in local perception of feature details, not only across visual field eccentricities but also across different visual field locations at the same eccentricity.

Both local perception of feature details and global perception of feature contexts were robust against nuisance factors such as the experimental paradigm, suggesting that their variability across individuals represents personal traits. The trait-like variability in local and global

perception of elementary visual features may be partially accounted for by non-neurobiological factors such as cultural influences [110, 111]. However, non-neurobiological factors alone are not able to explain the distinct patterns of perceptual variability associated with different categories of elementary visual features. The observation of inter-individual trade-off between local and global perception of orientation but not between local and global perception of contrast or luminance hints towards a neurobiological contribution.

The neurobiological factors that contribute to inter-individual perceptual variability may span multiple levels from the anatomy of visual cortices to the response function of visual cortical neurons. Importantly, this neurobiological contribution would need to explain for the difference between orientation perception and contrast or luminance perception in the pattern of inter-individual variability. The neural response to orientation and the neural response to luminance share the same Gaussian-shaped function [38, 96]. However, the neural response to orientation is unique in its orderly cortical representation, where visual cortical neurons responding to more similar orientation are more likely to be cortically adjacent and connected [37, 38, 43]. This orderly cortical representation is not observed in neural response to contrast or luminance. In fact, whereas there is a relatively large number of different visual features, visual cortices can only accommodate a limited number of orderly representations [97], among which the orientation representation is an ecologically robust pattern observable in many mammalian species from rodents to human [37, 38, 41, 42, 43]. As such, inter-individual perceptual variability is likely to be neurobiologically based in the cortical representation of visual features.

Whereas inter-individual perceptual variability may be accounted for by a combination of non-neurobiological and neurobiological factors, intra-individual perceptual variability across the visual field may arise purely from a neurobiological basis, as a non-neurobiological explanation of the visual field heterogeneity appears difficult. By the same token, the exact neurobiological basis of intra-individual perceptual variability may differ from that of inter-individual perceptual variability. Specifically, inter-individual perceptual variability, likely shaped by the neurobiological differences between individuals in the representation of visual features over the visual cortex, represents a region-level characteristic. In contrast, given the retinotopic correspondence between visual field locations and visual cortical locations [71], intra-individual perceptual variability between different visual field locations is likely to be shaped by the neurobiological differences between corresponding visual cortical locations and therefore rep-

resents a point-level characteristic.

Intriguingly, the region-level characteristic of inter-individual perceptual variability and the point-level characteristic of intra-individual perceptual variability resemble the distinct nature exhibited by the two morphological dimensions, the surface area and the thickness, of cerebral cortex. Although the cortical surface area and the cortical thickness jointly determine the cortical volume, the two morphological dimensions are controlled by independent sets of genetic-developmental factors and capture different aspects of cortical anatomy [49, 57, 58, 46]. Specifically, the cortical surface area captures the region-level cortical anatomy, where the surface area of a cortical region is determined jointly by the set of cortical locations it bounds. By contrast, the cortical thickness captures the point-level cortical anatomy, where the thickness at different cortical locations within the same cortical region can be assessed independently. This characteristic similarity between perceptual variability and anatomical variability is further illustrated in the different extent of variability exhibited by the cortical surface area versus the cortical thickness. The cortical surface area has expanded over one thousand fold from small mammals to humans [46, 112]. Even within human species, the surface area of a cortical region (e.g., early visual cortices) can vary three-fold across healthy adults [48]. In contrast to the substantial inter-individual variability in cortical surface area, cortical thickness differs marginally across human individuals and has only doubled during mammalian evolution [46, 112]. Nevertheless, the cortical thickness exhibits substantial intra-individual variability, where it can vary over three-fold across different cortical locations within the same cortical region of the same individual [113, 114].

As such, the variability in visual cortical thickness reflects the neurobiological differences between different visual cortical locations within the same individual and may underlie intra-individual perceptual variability, whereas the variability in visual cortical surface area reflects the neurobiological differences between different individuals and may underlie inter-individual perceptual variability. This hypothesis was tested in the next two chapters (Chapter Four, Chapter Five), where I explicitly explored how the surface area and the thickness of early visual cortices related to inter-individual and intra-individual variability in perception of elementary visual features.

Chapter 4

Role of Visual Cortical Surface Area

4.1 Introduction

The cerebral cortex is divided into a number of distinct cortical regions that each has its unique functions. Controlled by the interplay between genetic and developmental factors, this process of cortical arealization exhibits a substantial degree of inter-individual variability. As a notable example, the retinotopically defined surface area of early visual cortices (V1, V2) varies over three-fold across healthy human adults [48]. Such variability in visual cortical surface area is much greater than the variability in overall cortical surface area [115]. It has been suggested that the retinotopically defined surface area of early visual cortices may be an important endophenotype determining individual visual experiences [50]. Nevertheless, the exact relationships between inter-individual perceptual variability and visual cortical surface area remain largely unclear. Moreover, the possible mechanisms underlying such relationships remain unexplored.

In this chapter, I studied how the surface area of early visual cortices (V1, V2) related with inter-individual variability in local and global perception of elementary visual features. To this end, I hypothesized two possible mechanisms. The retinotopically defined surface area of early visual cortices represents neurobiological differences between individuals in the amount of cortical surface devoted to the same visual field space [71]. Consequently, a visual stimulus of the same physical size will activate a larger cortical area and have a larger effective size in individuals with a larger visual cortical surface area. One intuitive hypothesis is that visual cortical surface area influences perception through this scaling of effective stimulus size. The threshold of visual discrimination for local details and the magnitude of visual illusion (modulation) by global contexts, which reflect respectively local and global perception of elementary visual features, are both dependent on the stimulus size. Increasing the stimulus size generally leads to improved detail discrimination [116, 117, 118] but weakened contextual illusion

[119, 120, 121]. As such, individuals with a larger visual cortical surface area may perform finer visual discrimination of local details, whereas individuals with a smaller visual cortical surface area may experience stronger visual illusion (modulation) by global contexts. This first hypothesis suggests a generic change in the scope of visual perception from global, context-oriented to local, detail-oriented as visual cortical surface area increases across individuals.

A second, competing, hypothesis is that visual cortical surface area influences perception not just through the scaling of effective stimulus size, but also through the scaling of intracortical connectivity. When visual cortical surface area increases, physical constraints tend to prevent intracortical connections from lengthening at the same rate as the expansion of visual cortical surface, and different neurons within a neural population activated by a visual stimulus are thus less inter-connected [44, 45]. This intracortical scaling is likely to influence perception of different visual features differently, depending on their cortical representation. Specifically, for visual features (e.g., orientation) with a continuous, orderly cortical representation where the intracortical connectivity co-varies with the similarity in feature selectivity (e.g., orientation selectivity) between connected neurons [37, 97], the intracortical scaling will predominantly influence the connectivity between neurons responding to similar feature values (e.g., similar orientations). By contrast, for other visual features, the connectivity between neurons responding to similar versus opposite feature values will be equally affected and will counteract each other. Since local perception of feature details and global perception of feature contexts involve, respectively, discrimination and modulation between visual features close in values, the scaling of intracortical connectivity with the similarity in feature selectivity between connected neurons may be a mechanism through which visual cortical surface area influences visual feature perception. This second hypothesis suggests that the relationships between inter-individual perceptual variability and visual cortical surface area are not generic but are instead visual-feature-dependent.

To test these two hypotheses, I studied how the surface area of early visual cortices (V1, V2) related with inter-individual perceptual variability, for a variety of elementary visual features - orientation, contrast, and luminance. The visual discrimination threshold and the contextual illusion magnitude for orientation, contrast, or luminance are all dependent on the stimulus size [116, 117, 118, 119, 120, 121]. However, whereas the cortical representation of contrast or luminance is not orderly [97], the continuous, orderly representation of orientation in V1 is an ecologically robust pattern observable in many mammalian species from rodents to human [37, 41, 42, 97]. The commonality in stimulus size dependence versus the difference in

cortical representation between orientation and contrast or luminance allows one to disentangle the two hypotheses.

Taken together, in this chapter, I explored the relationships between inter-individual perceptual variability and visual cortical surface area in healthy human adults with two specific aims. First, I studied to which extent the surface area of early visual cortices varied across individuals, and whether such variability represented robust anatomical traits. Then, I tested how inter-individual variability in visual cortical surface area related with inter-individual variability in orientation perception, and whether such relationships, if observed, generalized to contrast or luminance perception. To this end, I assessed the variability across individuals in visual cortical surface area, using three different experimental paradigms where early visual cortices (V1, V2) were delineated retinotopically according to phase-encoded map, retinotopically according to population-receptive-field map, or morphologically according to cortical folding patterns. I also assessed inter-individual perceptual variability, by measuring the threshold of visual discrimination and the magnitude of contextual illusion for orientation, contrast, and luminance.

4.2 Methods

4.2.1 Participants and Apparatus

A group of twenty healthy participants (aged 19 to 34, ten females, ten males) gave written informed consent to take part in the experiments studying the robustness of the measure of visual cortical surface area, as well as the experiments studying the relationships between visual cortical surface area and orientation perception. For test-retest reliability, I repeated the experiments studying the relationships between visual cortical surface area and orientation perception, in a second group of twenty healthy participants (aged 21 to 35, nine females, eleven males). The second group of participants further took part in the experiments studying the relationships between visual cortical surface area and contrast or luminance perception. All participants had normal or corrected-to-normal vision and no neurological history. All experiments were approved by the UCL ethics committee.

The psychophysics experiments took place in a dark room where the computer monitor provided the only significant source of light. The visual stimuli were presented on a 22 inch computer monitor (size = 41 x 30.6 cm, resolution = 2048 x 1536 pixels) and viewed through a chin and forehead rest (viewing distance = 67 cm). The neuroimaging experiments took place in a Siemens Trio 3T MRI scanner with a 32-channel head-coil. The visual stimuli were pro-

jected onto a screen (size = 28.6 x 21.5 cm) in the back of the scanner and viewed through a mirror on the head-coil, where the viewing distance was 85 cm (the first group of participants) or 72 cm (the second group of participants). The stimuli covered a portion of the visual field extending from 0.25 to 7.2 degree eccentricity (the first group of participants) or 8.5 degree eccentricity (the second group of participants). For both groups of participants, structural MRI data were collected using a T1-weighted sequence at 1 mm resolution (TR = 7.92 ms, TE = 2.48 ms, matrix = 256 x 240). For the first group of participants, functional MRI data were collected using a 3D EPI sequence at 1.5 mm resolution (volume TR = 3.2 s, TE = 32.86 ms, matrix = 128 x 128). For the second group of participants, functional MRI data were collected using a 2D EPI sequence at 2.3 mm resolution (volume TR = 3.06 s, TE = 56 ms, matrix = 96 x 96). Functional MRI data were preprocessed in SPM8 through bias correction, realignment, unwarping, coregistration, and physiology noise correction.

4.2.2 Psychophysics experiments

To assess inter-individual variability in local and global perception, in separate experiments I measured the visual discrimination threshold and the contextual illusion magnitude for orientation, contrast, or luminance. Uniform gray stimuli that contained no contrast and no orientation were used in the luminance experiments; low-pass filtered white noise stimuli that contained no orientation and had constant average luminance were used in the contrast experiments; sinusoidal grating stimuli (spatial frequency =1.5 cycles per degree of visual angle) that had constant contrast (full-contrast) and constant average luminance were used in the orientation experiments. The orientation, contrast, and luminance experiments differed only in the visual stimuli and shared the same experiment procedures. Specifically, I used the standard 2-up-1-down staircase procedure to measure the visual discrimination threshold, and the standard method of constant stimuli to measure the contextual illusion magnitude. The visual discrimination threshold and the contextual illusion magnitude were both measured with a temporal forced-choice task, where participants judged the feature difference between two sequentially presented visual stimuli at the visual field center.

To measure the visual discrimination threshold, in a single experiment trial, two central circular stimuli (diameter = 1.5 degree of visual angle), one with a constant feature value (45 degree for orientation experiment, 40% for contrast experiment, 50% of the monitor maximum luminance for luminance experiment) and the other a variable feature value, were presented in succession on the computer monitor. The interval (first or second) where the stimulus with a constant feature value appeared was randomized across trials. The duration of each stimulus

was 300 ms and the inter-stimulus-interval was 500 ms. While maintaining central fixation throughout the experiment, participants made an unspeeded forced-choice regarding whether the second stimulus, compared with the first one, was rotated clockwise or anti-clockwise (orientation discrimination), had higher or lower contrast (contrast discrimination), or had higher or lower luminance (luminance discrimination). The feature difference between the two successively presented stimuli was varied in a 2-up-1-down staircase fashion that assessed the threshold value at which the discrimination performance converged to 70.7% correct [109]. Specifically, two consecutive correct answers led to a one-step decrease in the orientation, contrast, or luminance difference in the next trial, whereas one incorrect answer lead to a one-step increase in the feature difference. The experiment stopped after eighteen reversals, and the discrimination threshold was calculated as the feature difference averaged over the last ten reversals.

To measure the contextual illusion magnitude, in a single experiment trial, two central circular stimuli (diameter = 1.5 degree of visual angle), one with and one without a surrounding annular context (inner diameter = 1.5 degree of visual angle, outer diameter = 6 degree of visual angle), were presented in succession on the computer monitor. The feature difference between the surrounding context and the central stimulus was optimized to reach the maximum contextual illusion. Specifically, in the orientation experiment, the surrounding context was tilted 15 degree from the central stimulus; in the contrast experiment, the surrounding context had a contrast of 100% and the central stimulus a contrast of 40%; in the luminance experiment, the surrounding context alternated between black and white. The interval (first or second) where the surrounding context appeared was randomized but counter-balanced across trials. The duration of each stimulus was 300 ms and the inter-stimulus-interval was 500 ms. While maintaining central fixation throughout the experiment, participants made an unspeeded forced-choice regarding whether the central stimulus in the second interval, compared with the one in the first interval, was rotated clockwise or anti-clockwise (orientation experiment), had higher or lower contrast (contrast experiment), or had higher or lower luminance (luminance experiment). Prior to the experiment, each participant performed four trials in which they manually adjusted the orientation, contrast, or luminance of the central stimulus presented in isolation till it matched the perceived orientation, contrast, or luminance of the central stimulus presented in the surrounding context. In the subsequent experiment, the orientation, contrast, or luminance of the central stimulus presented in the surrounding context was kept constant, while that of the central stimulus presented in isolation was varied around this point of percep-

tual equality for seven different feature values. In a single experiment, a total of 112 trials (16 trials per feature value) were taken to produce a psychometric curve. The contextual illusion magnitude was calculated as the feature difference between the two central stimuli at the 50% threshold point of the psychometric curve where they appeared perceptually equal.

4.2.3 Phase-encoding retinotopic delineation of early visual cortices

Standard phase-encoded retinotopic mapping was applied to delineate early visual cortices (V1, V2) for both groups of participants [71]. Each participant took part in two experiment runs of polar-angle mapping and one experiment run of eccentricity mapping. The mapped visual field covered an eccentricity range from 0.25 to 7.2 degree of visual angle (the first group of participants) or 8.5 degree of visual angle (the second group of participants).

For polar-angle mapping, participants viewed full-contrast flickering checkerboard wedges (width = 40 degree) rotating smoothly around a small fixation cross for ten cycles per experiment run at a speed of twenty volumes per cycle. For eccentricity mapping, participants viewed full-contrast flickering checkerboard rings (width = 7.8% of the screen length) contracting smoothly around a small fixation cross for fifteen cycles per experiment run at a speed of fifteen volumes per cycle. To maintain participants' attention, at random temporal intervals the retinotopic mapping stimuli underwent a small pattern shift for 200 ms. Participants were asked to indicate whenever this happened with a button press while keeping their eyes fixated at the central cross during the whole experiment.

The polar-angle maps and the eccentricity maps were generated by applying Fast Fourier Transform to fMRI BOLD time series of each voxel that extracted the phase and the power at the stimulation frequency. The polar angle boundaries (representing vertical and horizontal meridians) were delineated manually according to the mirror reversals in the polar-angle maps. The eccentricity boundaries (representing 7.2 degree eccentricity for the first group of participants, representing 8.5 degree eccentricity for the second group of participants) were delineated automatically by thresholding the eccentricity maps.

4.2.4 Population-receptive-field retinotopic delineation of early visual cortices

To improve the reliability of retinotopic delineation, I conducted additional experiments for the first group of participants, where I applied population-receptive-field retinotopic mapping [122] to delineate early visual cortices (V1, V2). Each participant took part in two experiment runs. The mapped visual field covered an eccentricity range from 0.25 to 7.2 degree of

visual angle.

Participants viewed full-contrast flickering checkerboard bars (width = 1.8 degree of visual angle) moving smoothly in the visual field for eight cycles per experiment run at a speed of sixteen volumes per cycle (one visual field location per volume, sixty-four different visual field locations per experiment run, each visual field location repeated twice per experiment run). The bars were oriented at one of the four orientations (horizontal, vertical, 45 degree, 135 degree) and moved along the corresponding orthogonal direction (north/south for horizontal bar, west/east for vertical bar, northwest/southeast for 45 degree bar, northeast/southwest for 135 degree bar), where the orientation and the moving direction were counterbalanced across cycles. A blank screen was inserted into the last quarter of the second, fourth, sixth, and eighth cycle to provide a baseline condition that improved the measurement accuracy. To maintain participants' attention, at random temporal intervals the central fixation cross underwent a color change for 80 ms. Participants were asked to indicate whenever this happened with a button press while keeping their eyes fixated at the central cross during the whole experiment.

The polar-angle maps and the eccentricity maps were generated by fitting fMRI BOLD time series of each voxel with a two-dimensional Gaussian function f(x_0, y_0, σ) multiplied by the stimulus location function and convolved with hemodynamic response function [123, 124]. The two-dimensional Gaussian function characterized the visual field range (σ) that the voxel responded to and the visual field location (x_0, y_0) that the voxel responded strongest to [122]. Based on the two-dimensional Gaussian fit, the polar-angle maps and the eccentricity maps were calculated as $arctan(y_0/x_0)$ and $sqrt(x_0^2 + y_0^2)$, respectively. The polar angle boundaries (representing vertical and horizontal meridians) were delineated manually according to the mirror reversals in the polar-angle maps. The eccentricity boundaries (representing 7.2 degree eccentricity) were delineated automatically by thresholding the eccentricity maps.

4.2.5 Morphologic delineation of early visual cortices

As the retinotopic delineation covered a fraction rather than the overall extent of early visual cortices, it was potentially confounded by inter-individual variability in delineated fraction of early visual cortices. This potential confounding influence was assessed through additional experiments in the first group of participants, where I applied Freesurfer to delineate early visual cortices (Freesurfer pericalcarine segment and Freesurfer cuneus segment) according to the cortical folding patterns [125]. The morphologically delineated early visual cortices extended along the anterior-posterior axis from the rostral to the caudal ends of the calcarine

sulcus, and along the ventral-dorsal axis from the inferomedial end of the calcarine sulcus to the most medial portion of the occipital cortex.

4.3 Results

4.3.1 Variability in visual cortical surface area

The measure of visual cortical surface area was based on the retinotopic delineation of early visual cortices (V1, V2) [71, 48]. To improve the reliability of retinotopic delineation, I conducted two different retinotopic mapping experiments using phase-encoded paradigm [71] and population-receptive-field paradigm [122], respectively. I then compared the results from the two different experiments for each participant. Specifically, the polar-angle measures from the two different retinotopic mapping experiments were plotted against each other on a voxel basis, where voxels responding to similar polar angle were binned to generate 30 data points for each participant. I found that the measures were correlated between the two different retinotopic mapping paradigms ($r > 0.9$, $p < 0.0001$, N = 30 data points per participant). This high level of consistency demonstrated the robustness of retinotopic delineation against the delineation paradigm.

Based on the retinotopic delineation of early visual cortices, I applied the surface-based analysis to measure visual cortical surface area for each participant. In the surface-based analysis, structural MRI data were segmented into the white and the gray matter, from which the three-dimensional triangle-mesh models of the white and the pial cortical surfaces were built with each vertex of this mesh representing a single cortical location distinguishable by MRI [78]. Visual cortical surface area was calculated as the surface area summed over all visual cortical locations (vertices) delineated through retinotopic mapping. Consistent with previous reports [48], the retinotopically delineated surface area of early visual cortices exhibited a two-fold inter-individual variability (Figure 4.1A, V1 = 2213 mm^2 to 3328 mm^2, V2 = 1611 mm^2 to 2936 mm^2, summed across left and right hemispheres).

As the retinotopic delineation covered a fraction rather than the overall extent of early visual cortices, the measure of retinotopically delineated visual cortical surface area was potentially confounded by inter-individual variability in the delineated fraction of early visual cortices. To address this potential confounding influence, I estimated the delineation fraction for each participant, based on the distribution of mapped visual field eccentricity derived from the eccentricity map (Figure 4.1B). This distribution was best fitted with an exponential function $y = ae^{-bx}$. It reflected the number of voxels that responded to each visual field eccentric-

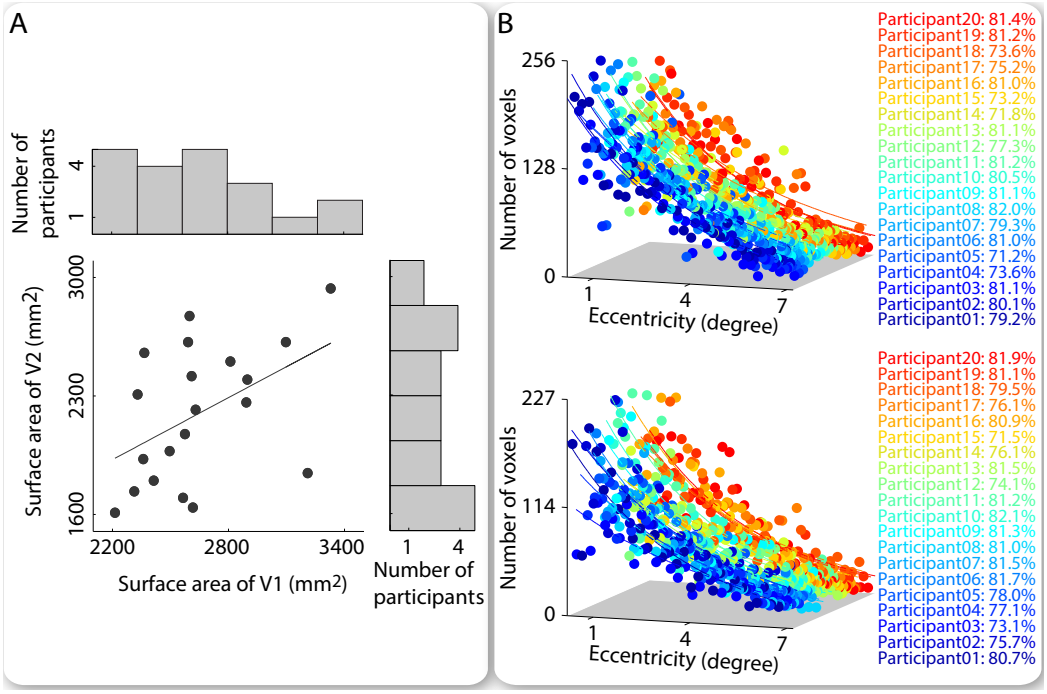

Figure 4.1: Variability in visual cortical surface area. Variability in visual cortical surface area was studied in a group of twenty participants, where retinotopic mapping was applied to delineate the part of early visual cortices (V1, V2) that responded to the visual field between 0.25 and 7.2 degree eccentricity. Based on the retinotopy delineation, visual cortical surface area was calculated as the surface area summed over all cortical locations in the retinotopically-delineated part of V1 or V2. This retinotopically-delineated visual cortical surface area exhibited a two-fold inter-individual variability (illustrated in the marginal histogram of A) that was correlated between V1 and V2 (illustrated in the scatter plot of A). To quantify the fraction of retinotopically delineated V1 or V2 to full V1 or V2, the distribution of mapped visual field eccentricity was plotted on a voxel basis, where voxels responding to similar eccentricity were binned to generate 30 data points for each participant (B). From the exponential fit to the eccentricity distribution, the retinotopically-delineated V1 or V2 was estimated as the area under the exponential fit between x equaled 0.25 and x equaled 7.2, and the full V1 or V2 as the area under the exponential fit between x equaled 0 and x approximated infinite. Data points are color coded according to the participant (B). Parameters reflect the fraction of retinotopically-delineated V1 or V2 (B).

ity. Given that different voxels were equal in volume, I estimated the retinotopically-delineated extent of early visual cortices as the area under the exponential curve from x equaled 0.25 to x equaled 7.2, and the overall extent of early visual cortices as the area under the exponential curve from x equaled 0 to x approximated infinite. I found that the retinotopic delineation

covered about three-fourths of the overall early visual cortices. Importantly, this delineation fraction was rather consistent across participants (V1: mean = 78.3%, std = 3.7%, N = 20 participants; V2: mean = 78.8%, std = 3.3%, N = 20 participants) and did not correlate with inter-individual variability in visual cortical surface area (V1: r = -0.120, 95% CI = [-0.53, 0.340], p = 0.564, N = 20 participants; V2: r = 0.080, 95% CI = [-0.38, 0.504], p = 0.768, N = 20 participants). Therefore, the retinotopically-delineated surface area of early visual cortices was more likely to reflect a true anatomical variability than a simple measurement artifact.

To further assess the reliability of retinotopic delineation, I performed morphologic delineation of early visual cortices based on the cortical folding patterns. The part of early visual cortices that extended along the anterior-posterior axis from the rostral to the caudal ends of the calcarine sulcus, and along the ventral-dorsal axis from the inferomedial end of the calcarine sulcus to the most medial portion of the occipital cortex, was delineated automatically in Freesurfer. I found that the morphologically delineated and the retinotopically delineated surface area of early visual cortices exhibited correlated inter-individual variability (V1: r = 0.709, 95% CI = [0.389, 0.876], $p < 0.001$, N = 20 participants; V2: r = 0.475, 95% CI = [0.042, 0.758], $p < 0.05$, N = 20 participants). The consistency with the morphologic delineation further demonstrated the reliability of retinotopic delineation in measuring visual cortical surface area.

4.3.2 Visual cortical surface area and perceptual variability

The analyses above revealed that the retinotopically delineated surface area of early visual cortices (V1, V2) exhibited a substantial degree of trait-like variability that was robust against the delineation paradigm. Building upon these observations, I explored how inter-individual variability in visual cortical surface area related with that in local or global perception of orientation, and whether such relationships, if observed, generalized to perception of contrast or luminance.

Across participants, I found that the retinotopically delineated surface area of V1 correlated negatively with the orientation discrimination threshold (Figure 4.2A, r = -0.700, 95% CI = [-0.87, -0.37], $p < 0.001$, N = 20 participants), suggesting that individuals with a larger V1 surface area were able to perform finer visual discrimination of local orientation details. Conversely, individuals with a larger V1 surface area tended to experience weaker visual illusion (modulation) by global orientation contexts, as the retinotopically delineated surface area of V1 correlated negatively with the orientation contextual illusion magnitude (Figure 4.2A, r =

-0.580, 95% CI = [-0.81, -0.19], $p < 0.01$, N = 20 participants). These correlations suggested that, as V1 increased in surface area across individuals, the scope of orientation perception shifted from global, context-oriented to local, detail-oriented.

Intriguingly, the correlations with orientation perception were not observed in V2, where the retinotopically delineated surface area of V2 exhibited no significant correlations with the orientation discrimination threshold (Figure 4.2B, r = -0.190, 95% CI = [-0.58, 0.275], p = 0.43, N = 20 participants) or the orientation contextual illusion magnitude (Figure 4.2B, r = -0.240, 95% CI = [-0.62, 0.226], p = 0.33, N = 20 participants). Moreover, the correlations between orientation perception and V1 surface area were significantly higher than the correlations between orientation perception and V2 surface area (T = 2.8, $p < 0.01$, N = 20 participants). These results hinted towards a selective dependence of orientation perception on V1 surface area that did not generalize to V2.

For test-retest reliability, I recruited a second group of twenty healthy participants. In this group of participants, I tested whether the relationships between visual cortical surface area and orientation perception were robust against the visual field coverage used in the retinotopic measure of visual cortical surface area. Specifically, I extended the visual field coverage from 7.2 degree eccentricity (the first group of participants) to 8.5 degree eccentricity (the second group of participants). The results in the second group of participants replicated these in the first group, where the orientation discrimination threshold and the orientation contextual illusion magnitude correlated significantly with the surface area of V1 (orientation discrimination threshold: r = -0.680, 95% CI = [-0.86, -0.34], $p < 0.001$, N = 20 participants; orientation contextual illusion magnitude: r = -0.580, 95% CI = [-0.81, -0.19], $p < 0.001$, N = 20 participants) but not V2 (orientation discrimination threshold: r = -0.340, 95% CI = [-0.68, 0.120], p = 0.14, N = 20 participants; orientation contextual illusion magnitude: r = -0.310, 95% CI = [-0.66, 0.153], p = 0.18, N = 20 participants). Thus, the relationships between the retinotopically delineated surface area of early visual cortices and the scope of orientation perception were robust against the exact visual field coverage used in the retinotopic measure of visual cortical surface area.

In the second group of participants, I also tested whether the relationships between visual cortical surface area and orientation perception were robust against the stimulus orientation used in the assessment of orientation perception. Specifically, I measured the orientation discrimination threshold and the orientation contextual illusion magnitude using two different setups where the grating stimuli were obliquely and cardinally oriented, respectively [126, 127].

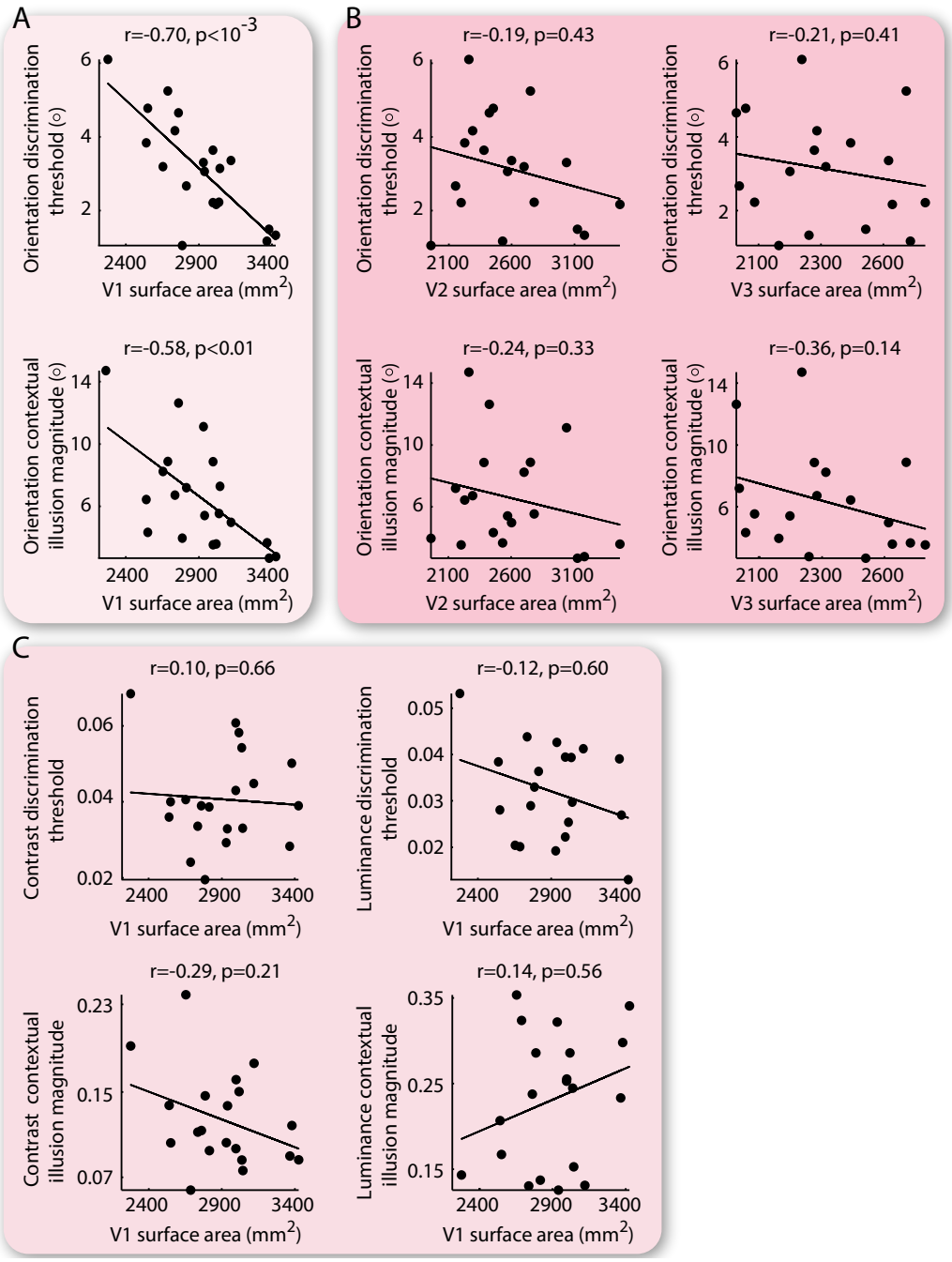

Figure 4.2: Visual cortical surface area and perceptual variability. Across a group of twenty participants, the orientation discrimination threshold and the orientation contextual illusion magnitude were plotted against the retinotopically defined surface area of V1, V2, or V3. The analysis revealed an inter-individual correlation between V1 surface area and orientation discrimination threshold or orientation contextual illusion magnitude (A), but a lack of correlation between V2 or V3 surface area and orientation perception (B). The discrimination threshold and the contextual illusion magnitude of contrast or luminance perception were plotted against V1 surface area, illustrating a lack of correlation between V1 surface area and contrast or luminance perception (C). Each point represents a single participant (N = 20) and the line is the best-fitting linear regression. Statistical values reflect Spearman's rho with FDR correction for multi-comparisons (α = 0.025).

I found that the correlations between V1 surface area and orientation perception were observed for both the oblique setup (orientation discrimination threshold: r = -0.680, 95% CI = [-0.86, -0.34], $p < 0.001$, N = 20 participants; orientation contextual illusion magnitude: r = -0.580, 95% CI = [-0.81, -0.19], $p < 0.001$, N = 20 participants) and the cardinal setup (orientation discrimination threshold: r = -0.590, 95% CI = [-0.82, -0.20], $p < 0.01$, N = 20 participants; orientation contextual illusion magnitude: r = -0.580, 95% CI = [-0.81, -0.19], $p < 0.01$, N = 20 participants). Therefore, the relationships between the retinotopically delineated surface area of early visual cortices and the scope of orientation perception were not affected by the stimulus orientation used in the assessment of orientation perception.

Finally, I explored whether the relationships between visual cortical surface area and orientation perception generalized to contrast or luminance perception. I measured the threshold of visual discrimination and the magnitude of contextual illusion for contrast and luminance. I found that the surface area of V1 exhibited no significant correlations with the contrast discrimination threshold (Figure 4.2C, r = 0.100, 95% CI = [-0.36, 0.519], p = 0.66, N = 20 participants), the contrast contextual illusion magnitude (Figure 4.2C, r = -0.290, 95% CI = [-0.65, 0.174], p = 0.21, N = 20 participants), the luminance discrimination threshold (Figure 4.2C, r = -0.120, 95% CI = [-0.53, 0.340], p = 0.60, N = 20 participants), or the luminance contextual illusion magnitude (Figure 4.2C, r = 0.140, 95% CI = [-0.32, 0.548], p = 0.56, N = 20 participants). Moreover, the correlations between V1 surface area and orientation perception were significant higher than the correlations between V1 surface area and contrast (T = 2.3, $p < 0.05$, N = 20 participants) or luminance perception (T = 3.1, $p < 0.01$, N = 20 participants). These results revealed a selective correlation between V1 surface area and orientation perception that did not generalize to luminance or contrast perception.

4.4 Discussion

In summary, my study revealed a substantial degree of inter-individual variability in visual cortical surface area that mediated an inter-individual perceptual trade-off between visual discrimination of local details and visual illusion (modulation) by global contexts. Specifically, I found that an inter-individual increase in V1 surface area was associated with a shift in the scope of orientation perception from global context-oriented to local detail-oriented, where individuals with a smaller V1 surface area experienced stronger visual illusion (modulation) by global orientation contexts and those with a larger V1 surface area performed finer visual discrimination of local orientation details. Intriguingly, this inter-individual correlation between

visual cortical surface area and perceptual trade-off was specific to V1 and to orientation perception; it was not observed for V2 or for contrast and luminance perception.

Such specificity of the anatomy-perception correlation to V1 and to orientation perception indicates that it is mediated by the unique way that V1 processes orientation. Compared to the cortical processing of contrast or luminance, the cortical processing of orientation is unique in its orderly representation where neurons selective for more similar orientation are more strongly connected [37, 38, 43]. In V1, this orderly orientation representation has a continuous coverage over the cortical surface [37]. As such, the change in V1 surface area would have a systematic influence on V1 connectivity, where the connectivity between V1 neurons with similar orientation selectivity would be scaled to a larger degree than the connectivity between neurons with opposite orientation selectivity. In V2, however, the orientation representation (thick stripe) is interleaved with the color representation (thin stripe) [35, 36]. As a result, the connectivity between V2 neurons with similar orientation selectivity is less likely to scale with V2 surface area but may instead vary with the stripe patterns. In contrast to the cortical processing of orientation, the cortical processing of contrast or luminance has no orderly representation [97]. Consequently, the connectivity between neurons with similar versus opposite feature (contrast, luminance) selectivity would be scaled to the same degree by the change in visual cortical surface area. Since local perception of feature details and global perception of feature contexts involve, respectively, discrimination and modulation between visual features close in values, the scaling of intracortical connectivity with the similarity in feature selectivity between connected neurons may be a mechanism through which visual cortical surface area influences visual feature perception.

My experiment observations therefore support my second hypothesis that visual cortical surface area influences perception of elementary visual features by an interaction between the scaling of effective stimulus size, where individuals with a larger visual cortical surface area in effect perceive the visual world through a magnifier relative to their colleagues, and the scaling of intracortical connectivity, where perception of different visual features is influenced differently depending on their cortical representations. Specifically, my experiment observations suggest that a continuous, orderly cortical representation of elementary visual features, where the net connectivity between neurons with similar feature selectivity scales systematically with visual cortical surface area, is essential for perception of this visual feature to be influenced by visual cortical surface area. Indeed, while there exists a relatively large number of different elementary visual features, visual cortices can only accommodate a limited number of

continuous, orderly representations [97]. Among these, the orientation representation in V1 is an ecologically robust pattern observable in many mammalian species from rodents to human [37, 41, 42, 97].

In addition to the continuous, orderly orientation representation in V1, other visual cortices also contain continuous, orderly representations of other elementary visual features. My hypothesis therefore suggests that the correlations between orientation perception and V1 surface area would be generalizable to perception of other elementary visual features and to surface area of other visual cortices, where that visual feature is represented in a continuous and orderly fashion in that visual cortex. For example, similar to orientation, ocular dominance has a continuous, orderly V1 representation that is prominently observed in mammalians from rodents to human [37, 97, 128]. As such, my hypothesis predicts that, an inter-individual increase in V1 surface area would lead to weakened intracortical inhibition between neurons with opposite ocular preference, and weakened interocular suppression in binocular rivalry where perception alternates between incompatible monocular stimuli [129, 130]. Indeed, an inter-individual correlation has been observed between the surface area of V1 and the level of intercoular suppression in binocular rivalry [131]. This observation supports my hypothesis, suggesting that the correlation with V1 surface area is not a specific property of orientation perception but is instead generalizable to perception of other elementary visual features with a continuous, orderly V1 representation.

While V2 does not have a continuous representation of orientation, it nonetheless contains a continuous representation of visual field location (retinotopy) that resembles the visual field representation in V1 [37]. As such, my hypothesis predicts a correlation between the surface area of V2 or V1 and perception of visual filed location. The relationship between visual cortical surface area and location discrimination was tested in the next chapter (Chapter Five), where I compared the thickness and the surface area of early visual cortices (V1, V2) in their contribution to perceptual variability. Apart from V1 and V2, V5/MT also contains continuous, orderly representations of elementary visual features, and in particular, of motion direction [132]. My hypothesis therefore predicts that individuals with a larger V5/MT surface area would perform finer discrimination of motion direction and individuals with a smaller V5/MT surface area would experience stronger contextual illusion (modulation) by motion direction. V5/MT can be delineated functionally using retinotopic mapping [72] or morphologically using myelination mapping [133]. It will be of interest for future studies to explore whether the correlation with inter-individual perceptual variability is generalizable to V5/MT

surface area.

By using psychophysical methods to assess visual perception and neuroimaging methods to assess visual cortical surface area, my experiments provided an implicit test for the involvement of intracortical connectivity in linking the surface area of early visual cortices to perception of elementary visual features. For an explicit test, in the next few chapters I addressed directly the role of intracortical connectivity. Specifically, in Chapter Six, I took a theoretical approach and built a visual cortical model, to test whether the simulated scaling of intracortical connectivity with model visual cortical surface area could reproduce the empirically observed correlations between visual cortical surface area and visual perception. Then, in Chapter Eight, I took an empirical approach and measured the intracortical connectivity in early visual cortices, to explore whether the weakening of intracortical connectivity indeed shifted the scope of visual perception from global context-oriented to local detail-oriented.

Chapter 5

Role of Visual Cortical Thickness

5.1 Introduction

The cerebral cortex is a sheet of neural tissue composed of vertical ontogenetic columns and horizontal laminar layers [46, 134]. As such, the morphology of cerebral cortex is characterized by two geometrically-orthogonal dimensions, the cortical surface area and the cortical thickness, shaped respectively by the proliferation of cortical columns and the generation of cortical layers [46, 134, 135, 136, 137]. Although the cortical surface area and the cortical thickness are controlled by independent sets of genetic-developmental factors, these two morphological dimensions jointly determine the cortical volume (i.e., the gray matter volume) [49, 57, 58, 46]. A lot of recent progress has been made in identifying the correlations between a larger cortical volume and a higher behavioral performance [1]. However, the fundamental question of whether a larger cortical volume is in essence behaviorally advantageous remains unclear. One approach to address this question is by studying whether the cortical surface area and the cortical thickness, which have the same contribution to the cortical volume, exert similar or different influence on behavioral performance.

In the last chapter (Chapter Four), I explored the influence of visual cortical surface area on perception of elementary visual features. In this chapter, I focused on the influence of visual cortical thickness and tested two alternative hypotheses. Intuitively, it is possible that increases in visual cortical volume, arising either from visual cortical surface area or visual cortical thickness, may influence visual perception by engaging responses from more neurons [138] and increasing the overall signal-to-noise ratio [139]. Such a hypothesis suggests that visual cortical surface area and visual cortical thickness would exert similar influence on visual perception. Alternatively, it is also possible that any influence on visual perception would differ between visual cortical surface area and visual cortical thickness, as these two morphological dimensions capture distinct aspects of cortical anatomy that may affect different components

of intracortical processing [45]. Specifically, visual cortical surface area captures the regional-level cortical anatomy, where it is determined jointly by all visual cortical locations and reflects the result of cortical arealization. By contrast, visual cortical thickness captures the point-level cortical anatomy, where it is determined independently for individual visual cortical location and reflects the result of tissue proliferation. Therefore, the variability in visual cortical surface area is likely to influence all the cortical columns within a visual cortical region and the inter-columnar processing between them, whereas the variability in visual cortical thickness is likely to influence only the local cortical column and the inter-laminar processing within it.

In addition to affecting different components of intracortical processing, visual cortical surface area and visual cortical thickness exhibit dissociable patterns of variability that further hint towards their different influence on visual perception. Specifically, from mice to humans, the cortical surface area has expanded over one thousand fold [46, 112], and even across healthy human adults, the surface area of a cortical region such as visual cortical surface area may vary up to three-fold [48]. In contrast to the substantial inter-individual variability exhibited by the cortical surface area, the cortical thickness differs marginally across human individuals and has only doubled from mice to humans [46, 112]. However, the cortical thickness exhibits substantial intra-individual variability, where it may vary over three-fold across different cortical locations within the same cortical region of the same individual [113, 114]. As such, the variability in visual cortical surface area may reflect the differences across individuals in visual processing over the visual cortex and is likely to underlie inter-individual perceptual variability, whereas the variability in visual cortical thickness may reflect the differences within individuals in visual processing at different visual field locations and is likely to underlie intra-individual perceptual variability.

To test these two hypotheses, I compared the surface area and the thickness of early visual cortices (V1, V2) in their contribution to perceptual variability. Inter-individual and intra-individual perceptual variability can be similarly measured using the visual discrimination threshold such as the location discrimination threshold (i.e., visual acuity). Specifically, by measuring the visual discrimination threshold at a set of non-overlapping visual field locations, one can assess not only the perceptual variability across individuals but also the perceptual variability within an individaul across the visual field [2, 99]. Moreover, by distributing the set of visual field locations along both the axis of eccentricity and the axis of polar angle, one can decompose the perceptual variability further into an eccentricity-dependent and an eccentricity-independent component that reflects respectively, how the visual discrimination

threshold varies along the visual field eccentricity and across different visual field locations at the same eccentricity.

Taken together, in this chapter, I explored the relationships between perceptual variability and visual cortical thickness in healthy human adults with three specific aims. First, I studied the extent to which visual cortical thickness varied across different visual cortical locations, and whether such variability represented robust anatomical traits. Then, I tested how the variability in visual cortical thickness related with the variability in location discrimination threshold, separately for the eccentricity-dependent and the eccentricity-independent component. Last, I addressed whether the influence of visual cortical thickness on location discrimination threshold resembled that of visual cortical surface area. To this end, I assessed the variability in visual cortical thickness, using different experimental paradigms where structural data were acquired from T1-weighted MRI imaging (in-vivo), quantitative-T1 MRI imaging (in-vivo), or histology sectioning (in-vitro), and then analyzed in SPM [140], FSL [141], Freesurfer [142], or MIPVA CBS [143]. I also assessed the perceptual variability, by measuring the location discrimination threshold at thirteen non-overlapping visual field locations covering three eccentricities (0, 4.7, 6.7 degree) and six polar angles (45, 90, 135, 225, 270, 315 degree).

5.2 Methods

5.2.1 Participants and Apparatus

A group of twenty healthy participants (aged 19 to 34, ten females, ten males), with normal or corrected-to-normal vision and no neurological history, gave written informed consent to take part in this study approved by the UCL ethics committee. All participants took part in the psychophysics experiments where I measured the location discrimination threshold at thirteen non-overlapping visual field locations, as well as the neuroimaging experiments where I measured visual cortical thickness from T1-weighted structural MRI data at 1 mm resolution. Eight of the participants further took part in the neuroimaging experiments where I measured visual cortical thickness from quantitative-T1 structural MRI data, at 1 mm and 0.8 mm resolution.

The psychophysics experiments took place in a dark room where the computer monitor provided the only significant source of light. The visual stimuli were presented on the computer monitor and viewed through a chin and forehead rest. For the monitor display, I sought to acquire a high spatial resolution (i.e., a small pixel size) that improved the measurement accuracy, as well as a large visual field coverage that facilitated the measure of intra-individual

perceptual variability. However, there is a natural trade-off between the spatial resolution and the visual field coverage of any display. Consequently, I employed two different monitor displays, one 17 inch monitor (size = 34.2 x 27.5 cm, viewing distance = 3 m, resolution = 1280 x 960 pixels) that offered a high spatial resolution (pixel size = 0.005 degree of visual angle) yet a limited visual field coverage (radius = 2.4 degree of visual angle), and one 22 inch monitor (size = 41 x 30.6 cm, viewing distance = 67 cm, resolution = 2048 x 1536 pixels) that offered a large visual field coverage (radius = 12.9 degree of visual angle) yet a limited spatial resolution (pixel size = 0.017 degree of visual angle). I used the 17 inch monitor for the measures at the visual field center, and the 22 inch monitor for the measures at the peripheral visual field.

The neuroimaging experiments took place in a Siemens Trio 3T MRI scanner with a 32-channel head-coil. The visual stimuli were projected onto a screen (size = 28.6 x 21.5 cm) in the back of the scanner and viewed through a mirror on the head-coil (viewing distance = 85 cm). The stimuli covered a portion of the visual field extending from 0.25 to 7.2 degree eccentricity. Structural MRI data were collected using a T1-weighted sequence at 1 mm resolution (TR = 7.92 ms, TE = 2.48 ms, matrix = 256 x 240), or a quantitative-T1 sequence at 1 mm resolution, or a quantitative-T1 sequence at 0.8 mm resolution. The quantitative-T1 sequence involved acquisitions of five different MRI signals, and in particular, the proton-density-weighted signals (1 mm resolution: TR = 23.7 ms, TE = 2.2 ms to 19.7 ms by steps of 2.5 ms, matrix = 256 x 240; 0.8 mm resolution: TR = 25.25 ms, TE = 2.39 ms to 18.91 ms by steps of 2.36 ms, matrix = 320 x 280), the magnetization-transfer-weighted signals (1 mm resolution: TR = 23.7 ms, TE = 2.2 ms to 14.7 ms by steps of 2.5 ms, matrix = 256 x 240; 0.8 mm resolution: TR = 29.25 ms, TE = 2.39 ms to 18.91 ms by steps of 2.36 ms, matrix = 320 x 280), the T1-weighted signals (1 mm resolution: TR = 18.7 ms, TE = 2.2 ms to 14.7 ms by steps of 2.5 ms, matrix = 256 x 240; 0.8 mm resolution: TR = 25.25 ms, TE = 2.39 ms to 18.91 ms by steps of 2.36 ms, matrix = 320 x 280), the radio-frequency transmit field B1+ signals (1 mm resolution: TR = 500 ms, TE = 18.53 ms / 37.06 ms, matrix = 64 x 48; 0.8 mm resolution: TR = 500 ms, TE = 19.69 ms / 39.38 ms, matrix = 64 x 48), and the static magnetic field B0 signals (TR = 1020 ms, TE = 10 ms / 12.46 ms, matrix = 64 x 64). From these five MRI signals, quantitative-T1 structural MRI data were calculated according to the methods developed by [144, 145] including corrections for imperfect spoiling [146] and field (B1+, B0) inhomogeneities [147, 148]. Functional MRI data were collected using a 3D EPI sequence at 1.5 mm resolution (volume TR = 3.2 s, TE = 32.86 ms, matrix = 128 x 128). Functional MRI data were preprocessed in SPM8 through bias correction, realignment, unwarping, coregistration, and physiology noise correction.

5.2.2 Psychophysics experiments

To assess inter-individual and intra-individual perceptual variability, I measured the threshold of visual field location discrimination (i.e., visual acuity) for each participant at thirteen non-overlapping locations across the visual field through thirteen independent experiments. These thirteen locations covered three eccentricities (0, 4.7, 6.7 degree) and six polar angles (45, 90, 135, 225, 270, 315 degree). The thirteen experiments differed only in the location of visual stimuli and shared the same experiment procedures. Specifically, I used the standard 2-up-1-down staircase procedure with a spatial forced-choice task, where participants judged the location difference between two concurrently presented bar stimuli (Vernier stimuli).

In a single experiment trial, one pair of collinear bars and one pair of horizontally offset bars (single bar width = 0.15 degree of visual angle, single bar length = 0.6 degree of visual angle, vertical distance between two bars = 0.3 degree of visual angle) were presented in succession on the computer screen with randomized order. The duration of each bar pair was 300 ms and the inter-stimulus-interval was 500 ms. While maintaining central fixation throughout the experiment, participants made an unspeeded forced choice regarding which temporal interval contained the pair of horizontally offset bars. The horizontal location difference between the pair of horizontally offset bars was varied in a 2-up-1-down staircase fashion that assessed the threshold value at which the discrimination performance converged to 70.7% correct. Specifically, two consecutive correct answers led to a one-step decrease in the horizontal location difference in the next trial, whereas one incorrect answer lead to a one-step increase in the feature difference. The experiment stopped after eighteen reversals, and the location discrimination threshold was calculated as the horizontal location difference averaged over the last ten reversals.

5.2.3 MRI measure of visual cortical thickness

To measure visual cortical thickness, I applied standard phase-encoded retinotopic mapping to delineate early visual cortices (V1, V2) for each participant through two experiment runs of polar-angle mapping and one experiment run of eccentricity mapping. For polar-angle mapping, participants viewed full-contrast flickering checkerboard wedges (width = 40 degree) rotating smoothly around a small fixation cross for ten cycles per experiment run at a speed of twenty volumes per cycle. For eccentricity mapping, participants viewed full-contrast flickering checkerboard rings (width = 7.8% of the screen length) contracting smoothly around a small fixation cross for fifteen cycles per experiment run at a speed of fifteen volumes per cycle. To maintain participants' attention, at random temporal intervals the retinotopic map-

ping stimuli underwent a small pattern shift for 200 ms. Participants were asked to indicate whenever this happened with a button press while keeping their eyes fixated at the central cross during the whole experiment. The polar-angle maps and the eccentricity maps were generated by applying Fast Fourier Transform to fMRI BOLD time series of each voxel that extracted the phase and the power at the stimulation frequency. The polar angle boundaries (representing vertical and horizontal meridians) were delineated manually according to the mirror reversals in the polar-angle maps. The eccentricity boundaries (representing 7.2 degree eccentricity) were delineated automatically by thresholding the eccentricity maps.

Based on the retinotopic delineation of early visual cortices, the thickness at individual visual cortical locations and the surface area summed over all visual cortical locations were measured, by applying the surface-based analysis to structural MRI data [78]. In the surface-based analysis, structural MRI data were preprocessed through skull stripping and non-uniform intensity correction, after which the data were segmented into the white and the gray matter according to intensity-based tissue classification. From the white and the gray matter segments, the three-dimensional triangle-mesh models of the white and the pial cortical surfaces were built with each vertex representing a single cortical location distinguishable by MRI. The three-dimensional triangle-mesh model is a collection of vertices (points), edges (connections between vertices), and triangle faces (closet sets of three edges) that defines the shape of a three-dimensional object. From the three-dimensional triangle-mesh models, the cortical thickness was computed as the distance between the white and the pial cortical surfaces, and the cortical surface area was computed as the summed surface area of triangle faces in a cortical region.

The MRI measure of visual cortical thickness was vulnerable to the confounding influence of data analysis software. To separate the contribution of software specific versus software independent factors, I repeated the analysis in four established software (SPM, FSL, Freesurfer, MIPVA CBS). For each participant, the pre-processing of raw data and the segmentation of cortical tissues were repeated in four different software (SPM, FSL, Freesurfer, MIPVA CBS), after which the reconstruction of cortical surfaces and the computation of cortical thickness were repeated in two different software (Freesurfer, MIPVA CBS). On a voxel basis, I compared the segmentation of cortical tissues across software by calculating the standard deviation of inner and outer cortical boundaries; I also compared the computation of cortical thickness (as well as the reconstruction of cortical surfaces) across software by calculating the correla-

tion in the cortical thickness measures.

Apart from the concern of data analysis software, the MRI measure of visual cortical thickness was also vulnerable to the confounding influence of data acquisition sequence. Specifically, despite being a widely used standard protocol, the T1-weighted sequence in fact detects a mixture of magnetic-field-specific and biological-tissue-specific signals. As a result, T1-weighted structural MRI data have inhomogenous intensity and low tissue contrast that are likely to bias the segmentation of cortical tissues and the computation of cortical thickness. To address the limited quality of the standard T1-weighted sequence, I further collected structural MRI data using the advanced quantitative-T1 sequence. Through the detection of multiple parametric signals, the quantitative-T1 sequence effectively factors out the magnetic-field-specific component and directly reflects the physical property (proton longitudinal relaxation rate, R1 = 1/T1) of the underlying biological tissue [145]. Consequently, quantitative-T1 structural MRI data have homogeneous intensity and high tissue contrast that greatly reduce potential bias in the surface-based analysis. The surface-based analysis of quantitative-T1 structural MRI data were carried out in MIPVA CBS, as the software was developed for high resolution structural data and had no constrain of voxel size [143]. On a voxel basis, I compared the measure of visual cortical thickness from 1 mm resolution T1-weighted structural MRI data, 1 mm resolution quantitative-T1 structural MRI data, and 0.8 mm resolution quantitative-T1 structural MRI data.

5.2.4 Histology measure of visual cortical thickness

Although structural MRI data offer a non-invasive in-vivo measure of visual cortical thickness, the measure is at the same time limited by its indirect nature. In contrast, a direct measure of visual cortical thickness (albeit in-vitro) is possible from histology data. To assess the reliability of the MRI measure of visual cortical thickness, I therefore acquired the measure of visual cortical thickness from histology data. To this end, I searched publicly available sources of histology data (e.g., brainmaps.org, LONI, Allen Institute) for a dataset with high resolution, fine alignment, and little distortion. Despite the efforts, I was not able to find a public dataset that met my needs. Nevertheless, through extensive search of private resources, I managed to access a dataset of high-resolution (40 μm isotropic pixel), whole-brain (4992 pixel x 3328 pixel), histology images (502 images in total), taken consecutively every 300 μm along the dorsoventral axis of a postmodern human body.

This dataset was generously shared by Drs. Yuchun Tang and Shuwei Liu (Research Cen-

ter for Sectional and Imaging Anatomy, Shandong University, China) under approval from local ethics committee. The postmodern body came from a deceased 38-year-old male who had donated his body for medical research purposes and had no neurological history. After the body was frozen and fixed, the head was dissected from the plane of thyroid cartilage and embedded in blue-stained gelatine. Serial transverse sectioning was performed along the dorsoventral axis using computerised freezing milling technique (milling machine: SKC500, Jinan, China; milling accuracy: 1 μm) [149]. A high-resolution digital camera (Canon EOS 1D MARK II, Japan) was used to take the histology images along with the images of length markers and color charts. The images of length markers and color charts were subsequently used as reference in affine alignment of the histology images. The results of affine alignment were independently checked by two experienced neuroanatomists (Yuchun Tang and Bo Sun) and confirmed through three-dimensional volume reconstruction of the head.

Compared to the standard 1000 μm resolution of structural MRI data, the 40 μm in-plane resolution of histology data enabled much more accurate measure of visual cortical thickness. However, conventional histology data analysis employs a slice-based approach that is constrained by the slice orientation and limited in sampling coverage. For example, the sliced-based measure of visual cortical thickness is only valid for histology slices orthogonal to the cortical surface. By contrast, conventional MRI data analysis employs a surface-based approach that is unrestricted by the slice orientation and offers an unbiased sampling coverage. Because the purpose of my analysis was to compare visual cortical thickness measured from structural MRI data with that from histology data, I tried to minimize the confounds associated with different sampling coverage of the two measures. Therefore, I developed a surface-based approach to analyze histology data. Similar to the surface-based analysis of structural MRI data, I performed tissue segmentation for each histology image, built the three-dimensional cortical surface models, and extracted the surface-based measure of visual cortical thickness.

As the first step of the surface-based analysis, I performed tissue segmentation for each of the 502 histology images. At first I tried to use automatic segmentation, since manual segmentation for 502 images would be labor-intensive and time-consuming. However, existing algorithms of automatic tissue segmentation all relied on the image intensity information and were developed mainly for structural MRI data, yet histology data differed substantially from structural MRI data in the image intensity distribution. This rendered MRI-based algorithms of automatic tissue segmentation unsuitable for histology data. Indeed, when I analyzed histology data in MRI-based software such as SPM and FSL, the results of automatic tissue segmentation

were rather inaccurate (Figure 5.1).

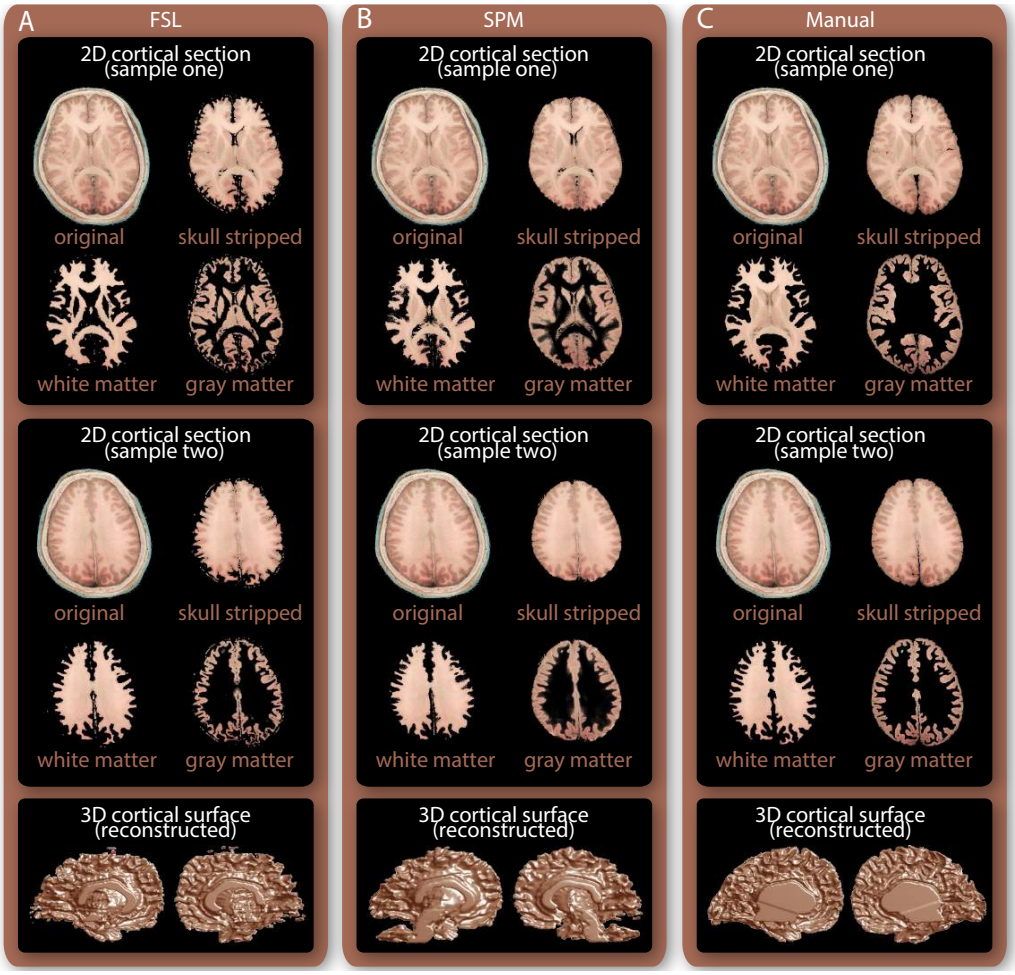

Figure 5.1: Histology measure of visual cortical thickness. To build the three-dimensional cortical surface models from the two-dimensional histology images, I segmented each histology image into the white and the gray matter. The approaches of automatic tissue segmentation, using existing software such as FSL (A) and SPM (B) or using custom-written code, all failed to reach satisfactory accuracy. Therefore, I took the approach of manual tissue segmentation (C). The differences between automatic and manual approaches in the performances of skull stripping, tissue segmentation, and cortical surface reconstruction, were illustrated in the two-dimensional cortical section images and the three-dimensional cortical surface images.

Consequently, I sought to write custom code that performed automatic tissue segmentation based on the color information and the consecutive nature of the histology images. To this end, I tried several approaches, including using the built-in functions of Mathematica (e.g., ImageForestingComponents, ClusteringComponents), using saliency detection algorithms (e.g., visual-feature-based, spectral-based), or a combination of both. However, neither of these approaches managed to reach satisfactory accuracy. Due to the failure of automatic tissue seg-

mentation, I resorted to manual tissue segmentation. I took advantage of the color information of the histology images, by performing manual segmentation on the red, green, and blue channel images in addition to the original image. Non-uniform intensity correction [150] was also applied, resulting in a total of eight images (corrected/uncorrected red/green/blue/all channel) per transverse section. Based on these images, I manually performed skull strip and tissue segmentation for each transverse section using the software Amira [151].

From these two-dimensional manual segments of the white and the gray matter, I built the three-dimensional triangle-mesh models of the white and the pial cortical surfaces in the software MIPVA CBS. During the analysis, the two-dimensional segments were binarized, downsampled to generate 300 μm isotropic voxels, and refined through three-dimensional topology correction. While traditional software such as Freesurfer was developed for low resolution structural data and had constrain of voxel size [142], this relatively new software MIPVA CBS was developed specifically for high resolution structural data and had no constrain of voxel size [143]. Using MIPVA CBS, I computed the cortical thickness was as the distance between the white and the pial cortical surfaces, with the biomechanics of cerebral cortex taken into consideration.

The surface-based analysis of histology data, although demanding, allowed direct comparison with structural MRI data in the measure of visual cortical thickness. To make the comparison, I delineated the occipital regions-of-interest in histology data according to the average retinotopic map acquired from the fMRI experiments. The regions-of-interest was transformed from the original image space to the histology image space through coregistration and reslice.

5.3 Results

5.3.1 Variability in visual cortical thickness

I acquired the measure of visual cortical thickness from the surface-based analysis on structural MRI data, where the cortical thickness was computed as the distance between the white and the pial cortical surfaces reconstructed from the white and the gray matter segments. This MRI measure of visual cortical thickness was potentially confounded by the choice of data analysis software. To assess the influence of data analysis software, I repeated the segmentation of cortical tissues in four different software (SPM, FSL, Freesurfer, MIPVA CBS), and the computation of cortical thickness (as well as the reconstruction of cortical surfaces) in two different software (Freesurfer, MIPVA CBS). Across software, I compared the segmentation of cortical tissues, by calculating the standard deviation of the inner cortical boundary

(white matter was given the value of one, gray matter the value of zero, the rest of the brain NaN) and that of the outer cortical boundary (gray or white matter was given the value of one, the rest of the brain the value of zero). The standard deviation was first calculated for individual voxel and then averaged across all voxels for individual participant. I also compared the computation of cortical thickness across software, by calculating the correlation in the cortical thickness measures. Specifically, the cortical thickness measured from Freesurfer was plotted against the cortical thickness measured from MIPVA CBS, where voxels with similar cortical thickness were binned to generate 30 data points. I found that the segmentation standard deviation in the occipital lobe [152] was low for both the inner cortical boundary (mean = 0.075, std = 0.009, N = 20 participants) and the outer cortical boundary (mean = 0.047, std = 0.009, N = 20 participants). Moreover, the measure of visual cortical thickness was highly correlated between different software ($r = 0.98$, $p < 0.0001$, N = 104158 voxels binned into N = 30 data points).

Such consistency suggested that the MRI measured thickness of early visual cortices was not biased by the specific choice of data analysis software. Nevertheless, the MRI measure of visual cortical thickness was still confounded by the choice of data acquisition sequence. Indeed, structural MRI data acquired using the standard T1-weighted sequence had inhomogenous intensity and low tissue contrast, as illustrated by the mixed peaks of white matter and gray matter in the image intensity histogram (Figure 5.2A). This could bias the segmentation of cortical tissues and the computation of cortical thickness. Nevertheless, the advanced quantitative-T1 sequence overcame this limitation and produced structural MRI data that had clearly separated peaks of white matter and gray matter in the image intensity histogram (Figure 5.2B). Moreover, by factoring out the magnetic-field-specific component and directly reflecting the biological-tissue-specific component, structural MRI data acquired using the quantitative-T1 sequence were highly reproducible across different scanning sessions and directly comparable across participants (Figure 5.2B). Such high image quality helped to reduce potential bias in the surface-based analysis. To assess the influence of data acquisition sequence, I compared visual cortical thickness measured from different acquisition sequences. I found that the MRI measure of visual cortical thickness was consistent between 1 mm resolution T1-weighted structural MRI data and 1 mm resolution quantitative-T1 structural MRI data ($r = 0.97$, $p < 0.0001$, N = 42538 voxels binned into N = 30 data points), as well as between 1 mm resolution quantitative-T1 structural MRI data and 0.8 mm resolution quantitative-T1 structural MRI data ($r = 0.97$, $p < 0.0001$, N = 42538 voxels binned into N = 30 data points).

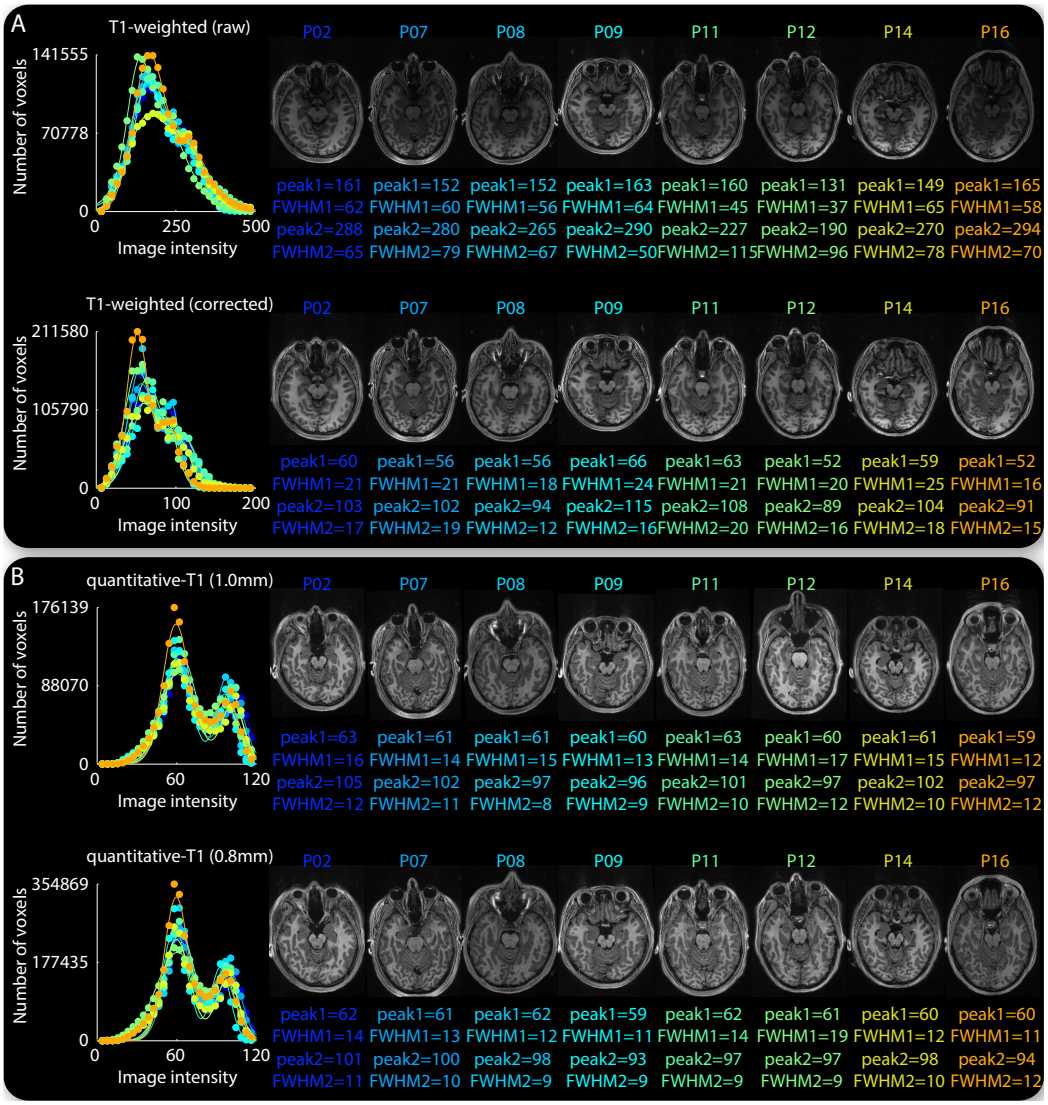

Figure 5.2: MRI measure of visual cortical thickness. Two different MRI sequences, the standard T1-weighted sequence and an advanced quantitative-T1 sequence, were used to collect the structural MRI images for eight of the twenty participants. The distribution of image intensity was plotted on a voxel basis, where voxels with similar intensity value were binned to generate 30 data points for each participant. The double Gaussian fit to the image intensity distribution revealed mixed peaks of white matter and gray matter in the T1-weighted MRI images, not only before but also after non-uniform intensity correction (A). By contrast, the quantitative-T1 MRI images showed clearly separated peaks of white matter and gray matter with consistent intensity values between 1 mm resolution and 0.8 mm resolution (B). These improvements in intensity homogeneity and tissue contrast from the T1-weighted MRI images to the quantitative-T1 MRI images were further illustrated in the sample cortical slices. Data points are color coded according to the participant. Parameters are derived from the double Gaussian fit to the image intensity distribution.

These correlations suggested that although the standard T1-weighted sequence did not offer high image quality, the MRI measured thickness of early visual cortices was robust against this limitation.

Based on the MRI measure, I studied the variability in visual cortical thickness. Compared to the substantial degree of inter-individual variability in visual cortical surface area [48], the average thickness of early visual cortices varied across participants in a much smaller degree from 2 mm to 2.5 mm. Nevertheless, within individual participants, the cortical thickness varied across different visual cortical locations from 1 mm to 4 mm following a Gaussian distribution (Figure 5.3). In addition to this general intra-individual variability in visual cortical thickness, I observed an intra-individual increase in visual cortical thickness from sulci to gyri and from parafovea (central 2.0 degree eccentricity) to perifovea. This increase in visual cortical thickness from parafovea to perifovea was observed for both sulci (V1: T = 6.533, $p < 0.0001$, N = 20 participants; V2: T = 8.359, $p < 0.0001$, N = 20 participants) and gyri (V1: T = 6.509, $p < 0.0001$, N = 20 participants; V2: T = 8.874, $p < 0.0001$, N = 20 participants). In a similar fashion, the increase in visual cortical thickness from sulci to gyri was observed for both parafovea (V1: T = 7.113, $p < 0.0001$, N = 20 participants; V2: T = 8.357, $p < 0.0001$, N = 20 participants) and perifovea (V1: T = 9.972, $p < 0.0001$, N = 20 participants; V2: T = 9.471, $p < 0.0001$, N = 20 participants).

These observations revealed that the MRI measured thickness of early visual cortices exhibited a substantial degree of trait-like variability that was robust against data analysis software and data acquisition sequence. As such, the variability was unlikely to represent a simple measurement error. Nevertheless, the MRI measure of visual cortical thickness was limited by its indirect nature. To address whether the variability in visual cortical thickness observed from structural MRI data represented a true anatomical trait, I studied the variability in visual cortical thickness measured from histology data. I found that the histology measure of visual cortical thickness exhibited a substantial degree of intra-individual variability that was similar in extent to the MRI measure of visual cortical thickness (V1: peak=1.896, FWHM=0.905; V2: peak=2.121, FWHM=0.820). Moreover, the dependence of visual cortical thickness on cortical folding and visual field eccentricity that I observed in structural MRI data was recaptured by histology data. Specifically, visual cortical thickness increased from sulci to gyri for parafovea (V1: T = 13.498, $p < 0.0001$, N = 87455 voxels; V2: T = 18.179, $p < 0.0001$, N = 86466 voxels) as well as for perifovea (V1: T = 23.822, $p < 0.0001$, N = 230387 voxels; V2: T = 9.507, $p < 0.0001$, N = 50348 voxels), and increased from parafovea to perifovea for sulci

(V1: T = 83.929, p < 0.0001, N = 146834 voxels; V2: T = 56.089, p < 0.0001, N = 72410 voxels) as well as for gyri (V1: T = 97.783, p < 0.0001, N = 171008 voxels; V2: T = 49.674, p < 0.0001, N = 64404 voxels).

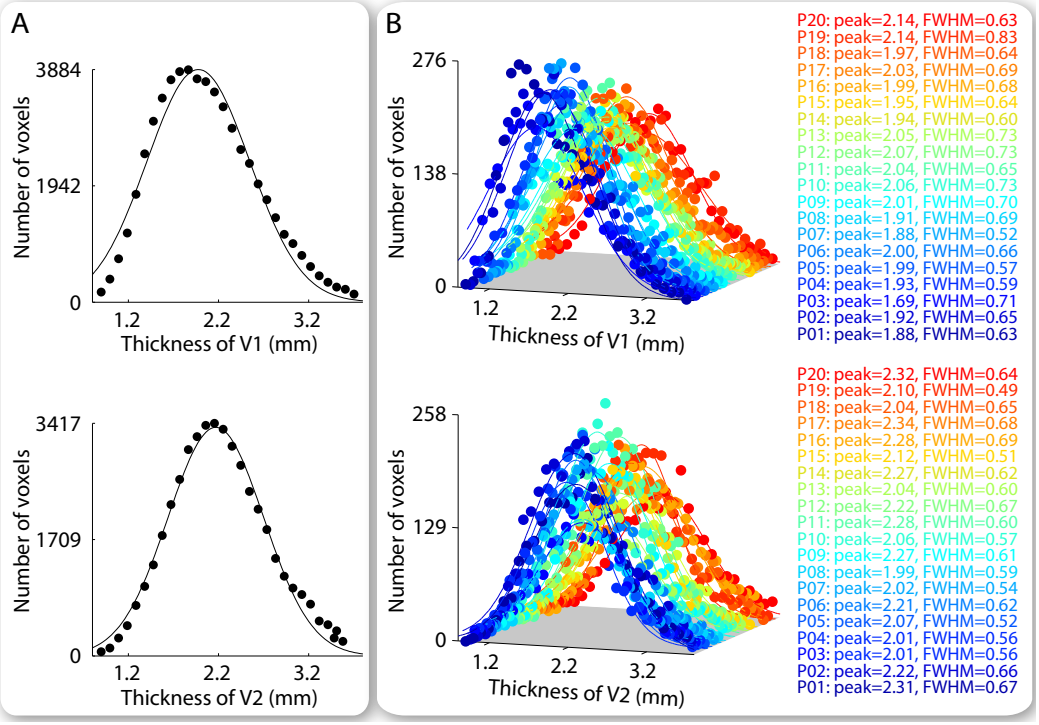

Figure 5.3: Variability in visual cortical thickness. Variability in visual cortical thickness was studied in a group of twenty participants, where retinotopic mapping was applied to delineate the part of early visual cortices (V1, V2) that responded to the visual field between 0.25 and 7.2 degree eccentricity. Based on the retinotopy delineation, visual cortical thickness was calculated as the vertical distance between the white and the pial surfaces for individual cortical locations in the retinotopically-delineated part of V1 or V2. The distribution of V1 or V2 thickness was plotted on a voxel basis, where voxels with similar cortical thickness were binned to generate 30 data points for the group of twenty participants (A) or for each participant in the group (B). The mean and the standard deviation of V1 or V2 thickness derived from the Gaussian fit to the thickness distribution illustrated the variability in visual cortical thickness across different visual cortical locations. Data points are color coded according to the participant (B). Parameters are derived from the Gaussian fit to the thickness distribution (B).

The consistency with the histology measure reassured the application of structural MRI data in measuring visual cortical thickness. As such, the observed variability in the MRI measured thickness of early visual cortices was likely to reflect a true anatomical trait. Building upon this observation, I explored how the variability in visual cortical thickness (mea-

sured using structural MRI data) related with that in location discrimination threshold (measured using psychophysics methods), and whether such relationships, if observed, resembled the relationships between visual cortical surface area and location discrimination threshold. The variability in location discrimination threshold had an eccentricity-dependent and an eccentricity-independent component. Therefore, I conducted separate analysis to study the influence that visual cortical anatomy exerted on the change in location discrimination threshold along the visual field eccentricity (eccentricity-dependent component) and the variability in location discrimination threshold across different visual field locations at the same eccentricity (eccentricity-independent component).

5.3.2 Visual cortical thickness and perceptual variability at fixed eccentricity

To explore the influence of V1 thickness on the eccentricity-independent variability in location discrimination threshold, I analyzed the relationships between V1 thickness and location discrimination threshold at a fixed visual field eccentricity (4.7 degree). Specifically, I plotted the location discrimination threshold measured at six different visual field locations of 4.7 degree eccentricity against the thickness at corresponding V1 locations, across the group of twenty participants. I observed a positive correlation between location discrimination threshold and V1 thickness ($r = 0.307$, 95% CI = [0.136, 0.460], $p < 0.001$, N = 20 participants x 6 visual field locations), which hinted towards finer discrimination at visual field locations that corresponded to thinner parts of V1.

This correlation, however, reflected a combined contribution of intra-individual and inter-individual factors. To separate the contribution of the two factors, I conducted further analysis where I calculated, for each participant, the location discrimination threshold as well as V1 thickness averaged across the six visual field locations, and for each visual field location, the location discrimination threshold as well as V1 thickness averaged across the twenty participants. By subtracting the averages of individual participants', I factored out inter-individual variability and studied intra-individual relationships. Similarly, by subtracting the averages of individual visual field locations', I factored out intra-individual variability and studied inter-individual relationships. In both cases, I still observed a positive correlation between location discrimination threshold and V1 thickness (intra-individually, $r = 0.339$, 95% CI = [0.171, 0.488], $p < 0.001$, N = 20 participants x 6 visual field locations; inter-individually, $r = 0.311$, 95% CI = [0.140, 0.464], $p < 0.001$, N = 20 participants x 6 visual field locations), suggesting

that the correlation existed both within and across individuals.

The positive correlation between location discrimination threshold and V1 thickness revealed that a larger V1 volume, if came from a larger V1 thickness, was associated with a lower performance in visual field location discrimination (i.e., a higher location discrimination threshold). To test whether the surface area of V1 would have a similar or a different contribution to visual field location discrimination, I analyzed the relationships between V1 surface area and location discrimination threshold at a fixed visual field eccentricity (4.7 degree). Specifically, across the group of twenty participants, I plotted the location discrimination threshold measured at six different visual field locations of 4.7 degree eccentricity against the surface area of participants' V1. I observed a negative correlation between location discrimination threshold and V1 surface area ($r = -0.318$, 95% CI = [-0.47, -0.15], $p < 0.001$, N = 20 participants x 6 visual field locations), suggesting that individuals with a larger V1 surface area were able to perform finer visual field location discrimination. As such, a larger V1 volume, if came from a larger V1 surface area, was associated with a higher performance in visual field location discrimination (i.e., a lower location discrimination threshold).

These correlations between location discrimination threshold and V1 anatomy revealed that the visual discrimination threshold for a specific visual field location was affected jointly by the thickness at corresponding V1 locations and the surface area of V1. To explore the influence that the thickness and the surface area of V2 might exert on the location discrimination threshold, I applied a similar analysis where I plotted the location discrimination threshold measured at six different visual field locations of 4.7 degree eccentricity against the thickness at corresponding V2 locations or the surface area of participants' V2. Similar to the observations in V1, a larger location discrimination threshold was observed at visual field locations that corresponded to V2 locations with a larger thickness ($r = 0.205$, 95% CI = [0.027, 0.370], $p < 0.05$, N = 20 participants x 6 visual field locations; intra-individually, $r = 0.200$, 95% CI = [0.022, 0.366], $p < 0.05$, N = 20 participants x 6 visual field locations; inter-individually, $r = 0.193$, 95% CI = [0.015, 0.359], $p < 0.05$, N = 20 participants x 6 visual field locations). Conversely, a smaller location discrimination threshold was observed in participants with a larger V2 surface area ($r = -0.315$, 95% CI = [-0.47, -0.14], $p < 0.001$, N = 20 participants x 6 visual field locations).

5.3.3 Visual cortical thickness and perceptual variability along eccentricity

My analyses above revealed an opposite relationship between visual cortical thickness and visual cortical surface area in their contribution to perceptual variability. This observation was made on the variability in location discrimination threshold across different visual field locations at the same eccentricity (eccentricity-independent component). To explore whether this observation was specific to certain visual field eccentricity or was generalisable across the visual field, I compared visual cortical thickness and visual cortical surface area in their contribution to the change in location discrimination threshold along the visual field eccentricity (eccentricity-dependent component). For this purpose, the location discrimination threshold, measured at thirteen non-overlapping visual field locations covering three eccentricities (0, 4.7, 6.7 degree) and six polar angles (45, 90, 135, 225, 270, 315 degree), was projected onto early visual cortices to produce a cortical map of location discrimination threshold (Figure 5.4A). This cortical projection allowed me to relate the location discrimination threshold at different visual field locations with the anatomy (thickness, surface area) of corresponding visual cortical locations on a vertex basis.

To explore the influence of V1 surface area on the eccentricity-dependent variability in location discrimination threshold, I plotted the location discrimination threshold at individual V1 locations (vertices) against the visual field eccentrics these locations responded to and V1 surface area of the participants, on a vertex basis. The data were binned into a data grid where individual data point represented the location discrimination threshold averaged over V1 locations (vertices) that were from the same participant and responded to similar eccentricities (Figure 5.4A). This three-dimensional data grid allowed me to separately address the influence that the visual field eccentricity and V1 surface area exerted on the location discrimination threshold. Along the axis of V1 surface area, I fitted individual plots of location discrimination threshold - visual field eccentricity with linear regression functions, where each plot represented the data from a single participant (Figure 5.4B). I found that the slope (r = -0.532, 95% CI = [-0.79, -0.19], $p < 0.05$, N = 20 participants) and the intercept (r = -0.675, 95% CI = [-0.86, -0.33], $p < 0.01$, N = 20 participants) of the fit both correlated negatively with the surface area of V1, while the goodness of the fit did not exhibit such correlation (r = -0.089, 95% CI = [-0.51, 0.368], p = 0.709, N = 20 participants). These observations suggested that participants with a larger V1 surface area had not only a smaller location discrimination threshold at fovea but also a slower increase in the location discrimination threshold along the visual field eccentricity. As such, the correlation between location discrimination threshold and V1 surface area

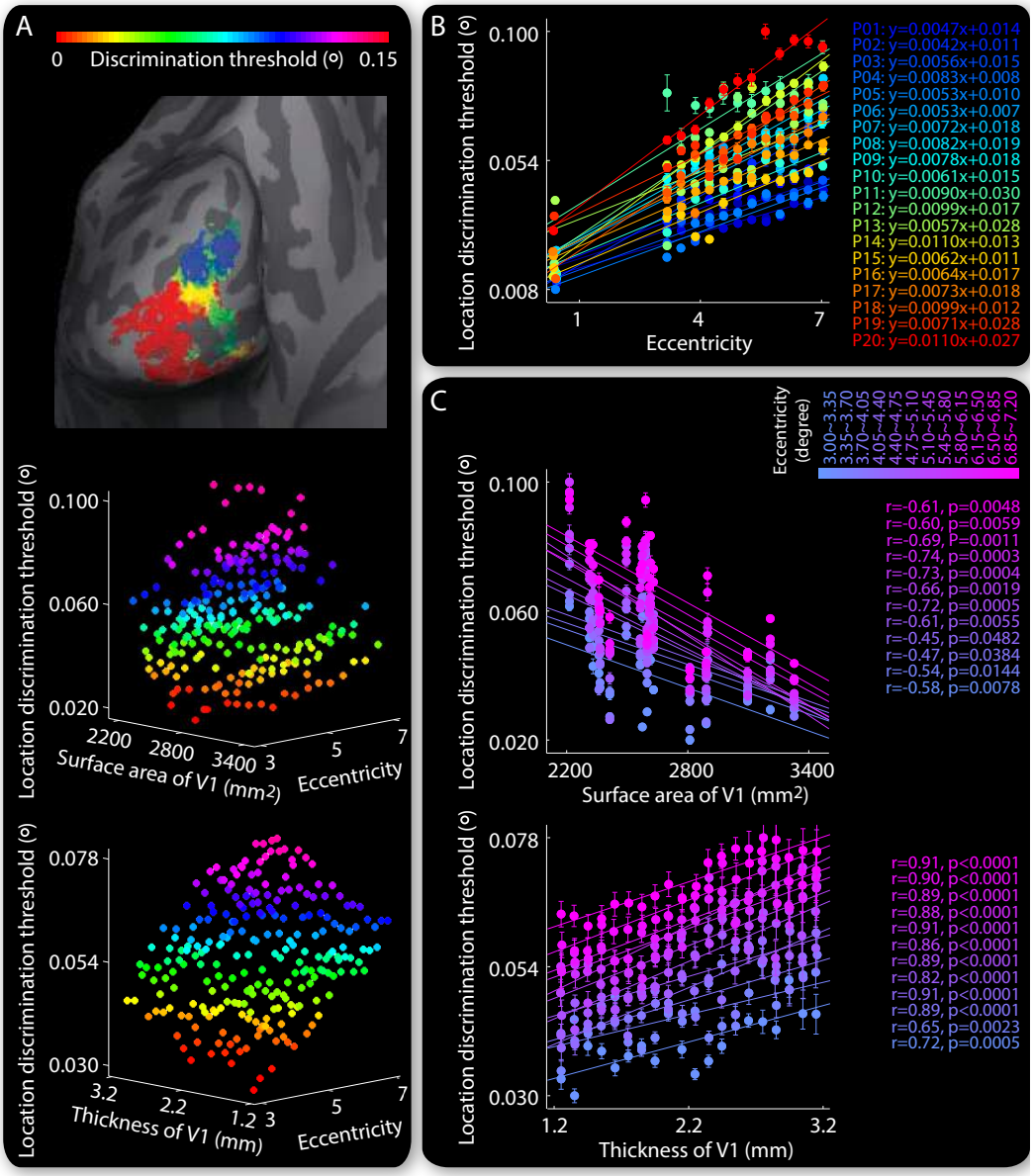

Figure 5.4: Visual cortical thickness and perceptual variability. The location discrimination threshold, measured at thirteen non-overlapping visual field locations, was projected onto V1 to generate a cortical surface map, based on which the location discrimination threshold at individual V1 locations was plotted against visual field eccentricities these locations responded to and V1 anatomy at these locations (A). Along the axis of V1 surface area, each plot of location discrimination threshold - visual field eccentricity represented the data from a single participant and illustrated the increase in location discrimination threshold with visual field eccentricity (B). Along the axis of visual field eccentricity, each plot of location discrimination threshold - V1 anatomy represented the data from a single eccentricity range and illustrated the dependence of location discrimination threshold on V1 surface area or V1 thickness (C). Data points are color coded according to the location discrimination threshold (A), the participant (B), or the visual field eccentricity (C). Equations reflect linear fit to the plot of location discrimination threshold - visual field eccentricity (B). Statistical values reflect permutation-based Spearman's rank correlation with FWE correction for multiple comparisons (C).

was not specific to certain visual field eccentricity but was instead generalisable across the visual field. Indeed, when I applied correlation analysis along the axis of visual field eccentricity directly on individual plots of location discrimination threshold - V1 surface area, I observed a negative correlation between location discrimination threshold and V1 surface area, for each range of visual field eccentricity.

To explore the influence of V1 thickness on the eccentricity-dependent variability in location discrimination threshold, I applied a similar analysis where I plotted the location discrimination threshold at individual V1 locations (vertices) against the visual field eccentrics these locations responded to and V1 thickness at these locations. The data were binned into a data grid characterising the increase in location discrimination threshold along the visual field eccentricity, as well as the relationships between location discrimination threshold and V1 thickness within individual ranges of visual field eccentricity (Figure 5.4A). In contrast to the negative correlation with V1 surface area, the location discrimination threshold correlated positively with V1 thickness, for each range of visual field eccentricity (Figure 5.4C).

These correlations between location discrimination threshold and V1 anatomy suggested that the observations at a fixed visual field eccentricity (4.7 degree), where the thickness and the surface area of V1 exhibited opposition relationships with location discrimination threshold, were generalisable across the visual field. To explore whether such generalization was observable in V2, I plotted the location discrimination threshold at individual V2 locations (vertices) against the visual field eccentricities these locations responded to and V2 anatomy (surface area, thickness) at these locations. Mirroring the observations in V1, V2 surface area correlated negatively with the location discrimination threshold, and specifically, with its value near fovea (r = -0.596, 95% CI = [-0.82, -0.21], $p < 0.01$, N = 20 participants) as well as its slope of increase along the visual field eccentricity (r = -0.642, 95% CI = [-0.84, -0.28], $p < 0.01$, N = 20 participants). Conversely, V2 thickness exhibited a positive correlation with the location discrimination threshold, for each range of visual field eccentricity.

5.4 Discussion

In summary, my study revealed a substantial degree of variability in visual cortical thickness that mediated the perceptual variability in visual field location discrimination. Specifically, I found that visual cortical thickness correlated positively with the threshold of visual field location discrimination, where finer visual field location discrimination was observed at visual field locations corresponding to thinner parts of early visual cortices, regardless of the

influence of visual field eccentricity. As such, a larger visual cortical volume, if it came from a larger visual cortical thickness, was associated with a lower performance in visual field location discrimination. Intriguingly, the exact opposition was observed for visual cortical surface area, where participants with a larger visual cortical surface area performed finer visual field location discrimination. Therefore, a larger visual cortical volume, if it came from a larger visual cortical surface area, was associated with a higher performance in visual field location discrimination.

The opposite relationship between visual cortical thickness and visual cortical surface area in their contribution to perceptual variability supports my second hypothesis, suggesting that the influence of visual cortical anatomy on visual perception is not mediated by the volume of cortical tissue involved in visual processing, but instead by the neural response function associated with intracortical processing. Indeed, the performance in visual discrimination is underpinned by the feature selectivity of visual cortical neurons that is in turn formed through the inter-laminar processing between cortical layers and modulated by the inter-columnar processing between cortical columns [103, 153, 154, 155, 156]. A thinned visual cortex with an enlarged surface area is likely to optimize the feature selectivity of visual cortical neurons, by maximizing the number of inter-columnar processing units and minimizing the time (delay) of inter-laminar processing [45, 46, 134, 136, 137].

Specifically, the thickening of visual cortex is likely to burden the intracortical processing, as the axons and the dendrites of inter-laminar connections would need to double and quadruple in diameter to improve the inter-laminar conduction speed and maintain the same inter-laminar processing time (delay) [45]. Due to the physical constrains on wiring costs, the inter-laminar connections tend to fall behind the increase in cortical thickness, with the consequence of lengthened inter-laminar processing time (delay) [44, 45, 157, 158, 159]. This lengthening of inter-laminar processing time (delay) with visual cortical thickness would then facilitate the response synchronization between different cortical columns, and in turn decrease the functional specificity (feature selectivity) of individual cortical columns [44, 45, 160, 161, 162]. Therefore, a larger visual cortical thickness is likely to be associated with a lower feature selectivity of visual cortical neurons, and correspondingly, a lower performance in visual discrimination.

By contrast, the enlargement of visual cortical surface area is likely to benefit the intracortical processing through an increase in the number of cortical columns available for inter-columnar processing. As the absolute length of inter-columnar connections is physically constrained and remains independent of visual cortical anatomy [44, 45, 46, 134, 136, 137], the

increased number of cortical columns would be accompanied by a proportionally weakened inter-columnar connectivity (i.e., a decrease in the proportion of cortical columns with which an individual cortical column connects). This weakening of inter-columnar connectivity with visual cortical surface area would then lower the response synchronization between different cortical columns, and in turn increase the functional specificity (feature selectivity) of individual cortical columns. Therefore, a larger visual cortical surface area is likely to be associated with a higher feature selectivity of visual cortical neurons, and correspondingly, a higher performance in visual discrimination.

Limited by the current resolution of non-invasive neuroimaging methods, an empirical assessment of the inter-columnar and the inter-laminar processing would be difficult in human participants. Nevertheless, a theoretical assessment would be possible, by using a visual cortical model to simulate the intracortical processing. As a proof of concept, in the next chapter (Chapter Six), I built such a visual cortical model and tested whether the simulated lengthening of inter-laminar processing time (delay) with model visual cortical thickness and the simulated weakening of inter-columnar connectivity with model visual cortical surface area could reproduce the empirically observed relationships between visual cortical anatomy and visual perception. Then, in the chapter after next (Chapter Seven), the predictions from the visual cortical model were tested empirically, where I used neuroimaging methods to measure the feature selectivity of visual cortical neurons and explored its dependence on visual cortical anatomy.

Chapter 6

Computational Model of Cortical Scaling

6.1 Introduction

In the last two chapters (Chapter Four, Chapter Five), I explored the neurobiological basis of inter-individual and intra-individual variability in perception of elementary visual features, using a combined approach of psychophysics, in-vivo MRI imaging, and in-vitro histology sectioning. I found that perception of local and global visual features, as assessed respectively from visual discrimination of local feature details and visual illusion induced by global feature contexts, exhibits a ten-fold inter-individual variability that correlates with the anatomy (surface area, thickness) of early visual cortices. Specifically, an increase in visual cortical surface area was associated with a shift in the scope of visual perception from global context-oriented to local detail-oriented, where individuals with a smaller visual cortical surface area experienced stronger illusion and individuals with a larger visual cortical surface area performed finer discrimination. Intriguingly, an increase in visual cortical thickness had the opposite influence, where discrimination of local feature details was finer at visual field locations corresponding to thinner parts of early visual cortices.

These correlations between visual cortical anatomy and visual perception were not generic but were instead contingent upon the cortical representation of visual features. Among different elementary visual features (orientation, visual field location, contrast, luminance) and different early visual cortices (V1, V2) studied, these correlations were observed specifically between orientation perception and V1 anatomy, as well as between visual field location perception and V1 or V2 anatomy. Compared to the cortical processing of luminance or contrast, the cortical processing of orientation or visual field location was unique in its orderly representation where neurons selective for more similar orientation or more similar visual field location were also more strongly connected. Moreover, while this orderly representation of visual field location was continuous over both V1 and V2 surface, the representation of orientation was continuous

in V1 but interleaved with the representation of color in V2.

As such, it seems that a continuous, orderly representation of elementary visual features in early visual cortex, where the intracortical connectivity between neurons with similar feature selectivity scales systematically with visual cortical anatomy, is essential for perception of this visual feature to be influenced by the anatomy (surface area, thickness) of this visual cortex. My experiment observations provide implicit support for my hypothesis that visual cortical anatomy influences visual perception through the scaling of intracortical processing. Specifically, I hypothesize that, as visual cortical surface area increases, the weakened inter-columnar connectivity would lower the response synchronization between different cortical columns. For visual features without a continuous, orderly cortical representation, the synchronization between cortical columns responsive to similar feature values and the synchronization between cortical columns responsive to opposite feature values would in contrast be equally lowered and counteract each other; for visual features with a continuous, orderly cortical representation, the weakened inter-columnar connectivity would predominantly lower the synchronization between cortical columns responsive to similar feature values, and in turn shift the scope of visual neural responses or the scope of visual perception from a stronger modulation (illusion) by global contexts to a finer selectivity (discrimination) for local details. By contrast, when visual cortical thickness increases, the lengthened inter-laminar processing time (delay) would facilitate the response synchronization between different cortical columns, and have the opposite functional impacts as the increase in visual cortical surface area.

For an explicit test of my hypothesis, in this chapter I focused directly on the role of intracortical processing, where I examined how the scaling of inter-laminar processing time with visual cortical thickness and the scaling of inter-columnar connectivity with visual cortical surface area influenced visual perception. Given the limited resolution of non-invasive neuroimaging methods, an empirical assessment of intracortical processing is difficult. Therefore, I took a theoretical approach where I applied an empirically based visual cortical model to simulate the intracortical scaling and to examine whether such theoretical simulation reproduced the empirically observed relationships between visual cortical anatomy and visual perception. The two aspects of visual perception - visual discrimination of local details and visual illusion by global contexts - correspond respectively to the feature selectivity and the contextual modulation of visual neural responses [102, 154]. This correspondence allows (indirect) interpretations of visual perception from modeling of visual neural responses.

To model the feature selectivity and the contextual modulation of visual neural responses,

one can apply models that belong in general to three categories - the structural models based on intracortical architecture [88, 163], the functional models based on neural computations (e.g., normalization) [164], and the statistical models based on visual input statistics [165]. Since my hypothesis concerned intracortical architecture, I applied the structural models and in particular, the neural field model. Motivated by empirical observations, the neural field model treats the brain as a dynamic system and simulates the spatiotemporal dynamics of neural responses based on the intracortical processing [88, 134, 157, 163, 166, 167, 168, 169]. Compared to other structural models such as the large-scale cortical model, the neural field model retains the same explanatory power yet relied on many fewer free parameters [170, 171]. Moreover, by incorporating neurovascular coupling, the neural field model can be extended to simulate the hemodynamic responses underlying fMRI BOLD signal [87, 172]. The focus of the neural field model provides a good match for my hypothesis, and the potential of the neural field model to simulate the hemodynamic responses further allows empirical test of the model predictions in human participants using fMRI.

Taken together, in this chapter, I explored the role of intracortical processing in linking visual cortical anatomy to visual perception with two specific aims. First, I studied whether a neural field model of intracortical processing that incorporated neurovascular coupling could capture the profile of neural responses with laminar-layer-specific onset of action potential and the profile of hemodynamic responses with initial dip. Then, I addressed whether this neural field model could recapitulate the empirically observed relationships between visual cortical anatomy and visual perception. Specifically, I assessed how the simulated scaling of inter-laminar processing time with model visual cortical thickness and the simulated scaling of inter-columnar connectivity with model visual cortical surface area would influence the feature selectivity and the contextual modulation of the model response, which corresponded respectively with visual discrimination for local details and visual illusion by global contexts. Moreover, I assessed whether such influence would differ for different elementary visual features (orientation, visual field location, contrast, luminance), depending on their cortical representations.

6.2 Methods

6.2.1 Intracortical processing in neural field model

The model visual cortex is constituted of inter-connected cortical columns where an individual cortical column is composed of inter-connected laminar layers. The inter-laminar

connections follow an empirically-based circuitry design, where layer IV sends input signals from hierarchically lower cortical region to layer V/VI through layer II/III, and layer V/VI sent back signals to layer IV through layer II/III [134, 166, 167, 168, 169]. Within an individual cortical column, layer II/III is the output layer that sends inter-columnar signals to other cortical columns (Figure 6.1). The inter-columnar connections follow an empirically-based Gaussian design where the inter-columnar connectivity decreases with the cortical distance between connected cortical columns [88, 157, 171].

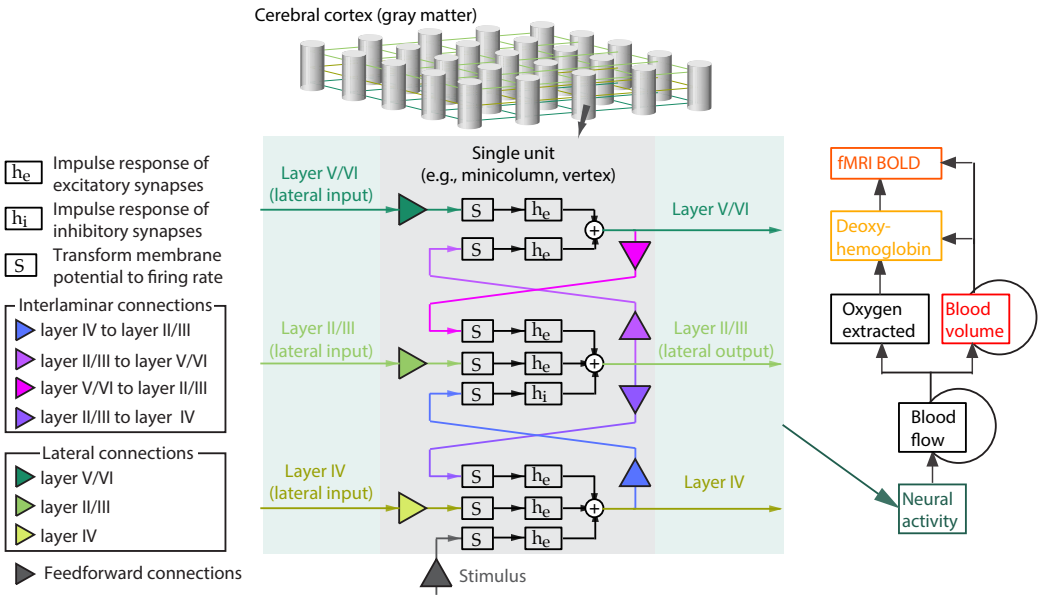

Figure 6.1: Model of intracortical processing. A visual cortical model based on mammalian cortical structure and neurovascular coupling was built to capture the spatiotemporal dynamics of cortical activity. The diagrammatic representation of the model illustrated the modulation of neural activity by inter-laminar connections and inter-columnar connections, as well as the modulation of hemodynamic activity by neurovascular events.

The synaptic activities in layer IV, layer II/III, and layer V/VI of an individual cortical column, represented respectively by $x_1(t)$, $x_2(t)$, and $x_3(t)$, are described in the equations below. These equations capture the inter-laminar and the inter-columnar modulation of synaptic activities. Specifically, the gain of reciprocal inter-laminar connections between layer II/III and layer IV or layer V is represented by G_{21} (G_{12}) or G_{23} (G_{32}). The gain of inter-columnar connections within layer IV, layer II/III, or layer V/VI is represented by G_{11}, G_{22}, or G_{33}, and the Gaussian kernel, a_1, a_2, or a_3, describes the extent of inter-laminar connections in layer IV, layer II/III, or layer V. The signal conduction speed is represented by δ, while H_e (H_i) and τ_e (τ_i) describe the amplitude and the time constant of excitatory (inhibitory) postsynaptic

potential. The transformation from synaptic activity $v(t)$ to neural firing rate $S(v(t))$ follows a sigmoid function.

$$\frac{\tau_e}{H_e}x_1(t)''+\frac{2}{H_e}x_1(t)'+\frac{1}{H_e\tau_e}x_1(t) = G_{21}S(x_2(t-\frac{\delta D}{3}))+G_{11}\sum_{j=1}^{L} e^{-\frac{j^2}{2a_1^2}}S(x_2(t-\delta j))+S(u(t)) \tag{6.1}$$

$$\frac{\tau_e}{H_e}x_{2e}(t)''+\frac{2}{H_e}x_{2e}(t)'+\frac{1}{H_e\tau_e}x_{2e}(t) = G_{12}S(x_1(t-\frac{\delta D}{3}))+G_{22}\sum_{j=1}^{L} e^{-\frac{j^2}{2a_2^2}}S(x_2(t-\delta j)) \tag{6.2}$$

$$\frac{\tau_i}{H_i}x_{2i}(t)'' + \frac{2}{H_i}x_{2i}(t)' + \frac{1}{H_i\tau_i}x_{2i}(t) = G_{32}S(x_3(t-\frac{2\delta D}{3})) \tag{6.3}$$

$$\frac{\tau_e}{H_e}x_3(t)''+\frac{2}{H_e}x_3(t)'+\frac{1}{H_e\tau_e}x_3(t) = G_{23}S(x_2(t-\frac{2\delta D}{3}))+G_{33}\sum_{j=1}^{L} e^{-\frac{j^2}{2a_3^2}}S(x_2(t-\delta j)) \tag{6.4}$$

$$x_2(t) = x_{2e}(t) - x_{2i}(t) \tag{6.5}$$

$$S(v(t)) = \frac{0.005}{1+e^{-560v(t)}} - 0.0025 \tag{6.6}$$

In the model visual cortex, the input signals from hierarchically lower cortical region to an individual cortical column $u(t)$ equal the convolution between the postsynaptic potential and the effective visual stimulus $Stimulus(t)$, where the effective visual stimulus is determined jointly by the feature selectivity of the cortical column (θ) and the feature value of the visual stimulus (θ_0). Specifically, for orientation, visual field location, or luminance, the effective visual stimulus is described by the Gaussian function, whereas for contrast, the effective visual stimulus is described by the Naka-Rushton function [38, 96, 98].

$$u(t) = (\frac{H_e}{\tau_e}e^{-\frac{t}{\tau_i}}) * Stimulus(t) \tag{6.7}$$

$$Stimulus(t) = e^{-\frac{(\theta-\theta_0)^2}{2a_0^2}} \tag{6.8}$$

$$Stimulus(t) = \frac{\theta_0^{a_0}}{\theta^{a_0}+\theta_0^{a_0}} \tag{6.9}$$

In the model visual cortex, the length of inter-laminar connections and inter-columnar connections is physically constrained and remains independent of the change in model visual cortical anatomy. Consequently, an increase in model visual cortical thickness is associated with an increase in inter-laminar processing time, whereas an increase in model visual cortical surface area is associated with a proportional decrease in inter-columnar connectivity (i.e., a decrease in the proportion of cortical columns with which an individual cortical column connects). This change in inter-columnar connectivity has different influence for different elementary visual features (orientation, visual field location, contrast, luminance), depending on

their cortical representations. Specifically, the cortical representation of orientation or visual field location is in an orderly fashion where adjacent cortical columns responded to adjacent orientations or adjacent visual field locations [38, 43]. As the inter-columnar connectivity covaries with the similarity in feature selectivity between connected cortical columns, a change in model visual cortical surface area influences the connectivity between cortical columns with similar feature selectivity to a larger degree than the connectivity between cortical columns with opposite feature selectivity. By contrast, the cortical representation of luminance or contrast is in a randomized fashion where the distance in cortical space does not reflect the distance in feature space [37, 97]. As the inter-columnar connectivity remains independent of the feature selectivity, the connectivity between cortical columns with similar versus opposite feature selectivity is affected to the same degree by the change in model visual cortical surface area.

6.2.2 Neurovascular coupling in neural field model

These neural responses, shaped by these inter-laminar and inter-columnar processing, in turn drive the hemodynamic responses through neurovascular coupling (Figure 6.1) [87, 172, 173, 174, 175, 176]. Specifically, following an arteriolar vasodilation, an increase in local cerebral blood flow (local oxygen delivery) is induced by synaptic activities. This increase in local oxygen delivery (local cerebral blood flow), however, exceeds the increase in local oxygen consumption and leads to an increase in oxyhemoglobin concentration. At the same time, the increase in local cerebral blood flow effectively inflates a venous balloon, where the deoxygenated blood is diluted at a greater rate and causes a decrease in deoxyhemoglobin concentration. As the dilution of deoxygenated blood falls behind the increased delivery of deoxygenated blood to veins, deoxyhemoglobin concentration exhibits an initial increase before its subsequent decrease.

These interactions between neural responses (synaptic activities) $v(t)$, cerebral blood flow $CBF(t)$, cerebral blood volume $CBV(t)$, deoxyhemoglobin concentration $HbR(t)$, and oxyhemoglobin concentration $HbO(t)$ are described in the equations below. The equations capture how the synaptic activates drive local cerebral blood flow and local cerebral blood volume, which in turn modulate deoxyhemoglobin concentration and oxyhemoglobin concentration. Specifically, the time constant and the efficacy for the synaptic-activity-induced change in cerebral blood flow are represented respectively by τ_1 and H_0, while the time constant for the auto-regulation of cerebral blood flow is represented by τ_2. The transit time τ_0 reflects the time constant for the inflation of venous balloon, which equals the resting cerebral blood flow divided by the resting cerebral blood volume. E_0 represents the fraction of resting oxygen

extraction, and α_0 the capacity of the venous balloon in diluting blood.

$$\frac{1}{H_0}CBF(t)'' + \frac{1}{H_0\tau_1}CBF(t)' + \frac{1}{H_0\tau_2}CBF(t) = v(t) + \frac{1}{H_0\tau_2} \tag{6.10}$$

$$\frac{1}{\tau_0}CBV(t)' + CBV(t)^{\frac{1}{\alpha_0}} = CBF(t) \tag{6.11}$$

$$\frac{1}{\tau_0}HbR(t)' + CBV(t)^{\frac{1-\alpha_0}{\alpha_0}}HbR(t) = CBF(t)\frac{1-(1-E_0)^{\frac{1}{CBF(t)}}}{E_0} \tag{6.12}$$

$$-HbO(t) + CBV(t) = HbR(t) \tag{6.13}$$

$$BOLD(t) = 7CBV_0E_0 + 2E_0 + 1.8 - 7CBV_0E_0HbR(t) - \frac{2HbR(t)}{CBV(t)} - (2E_0 - 0.2)CBV(t) \tag{6.14}$$

$$ISOI(t) = LE_{HbR}HbR(t) + LE_{HbO}HbO(t) \tag{6.15}$$

Based on these modeling of oxyhemoglobin concentration and deoxyhemoglobin concentration, the neural field model is extended to simulate the hemodynamic responses including fMRI BOLD signal and optical imaging signal. Specifically, fMRI BOLD signal is a function of deoxyhemoglobin concentration HbR and local cerebral blood volume CBV. Optical imaging signal, on the other hand, captures the absorption of near-infrared light by oxyhemoglobin and deoxyhemoglobin. According to Lambert-Beer law, the absorption of light through a substance depends on the absorption coefficient of the substance, the concentration of the substance, and the distance the light travels through the substance (the path length). Therefore, optical imaging signal is simulated as a function of E_{HbR} (E_{HbO}) and L, where E_{HbR} (E_{HbO}) reflects the absorption coefficient of deoxyhemoglobin (oxyhemoglobin) and L reflects the path length. E_{HbR} and E_{HbO} are dependent on the wavelength of near-infrared light applied for collecting optical imaging signal. When the wavelength is short (e.g., 530nm), E_{HbR} and E_{HbO} are close in value, and as a result, deoxyhemoglobin and oxyhemoglobin concentrations contribute roughly equally to optical imaging signal. At a longer wavelength (e.g., 600nm), however, E_{HbR} gets much greater than E_{HbO}, and thus, optical imaging signal reflects largely the deoxyhemoglobin concentration.

6.2.3 Analysis of neural field model

The neural field model describes in essence the spatiotemporal dynamics of a neural system that falls into the scope of dynamic system and control theory. This allows classical system analyses of the neural field model using knowledge from the control theory. For example, one could apply the root-locus analysis to reveal the system stability from the zeros (the points

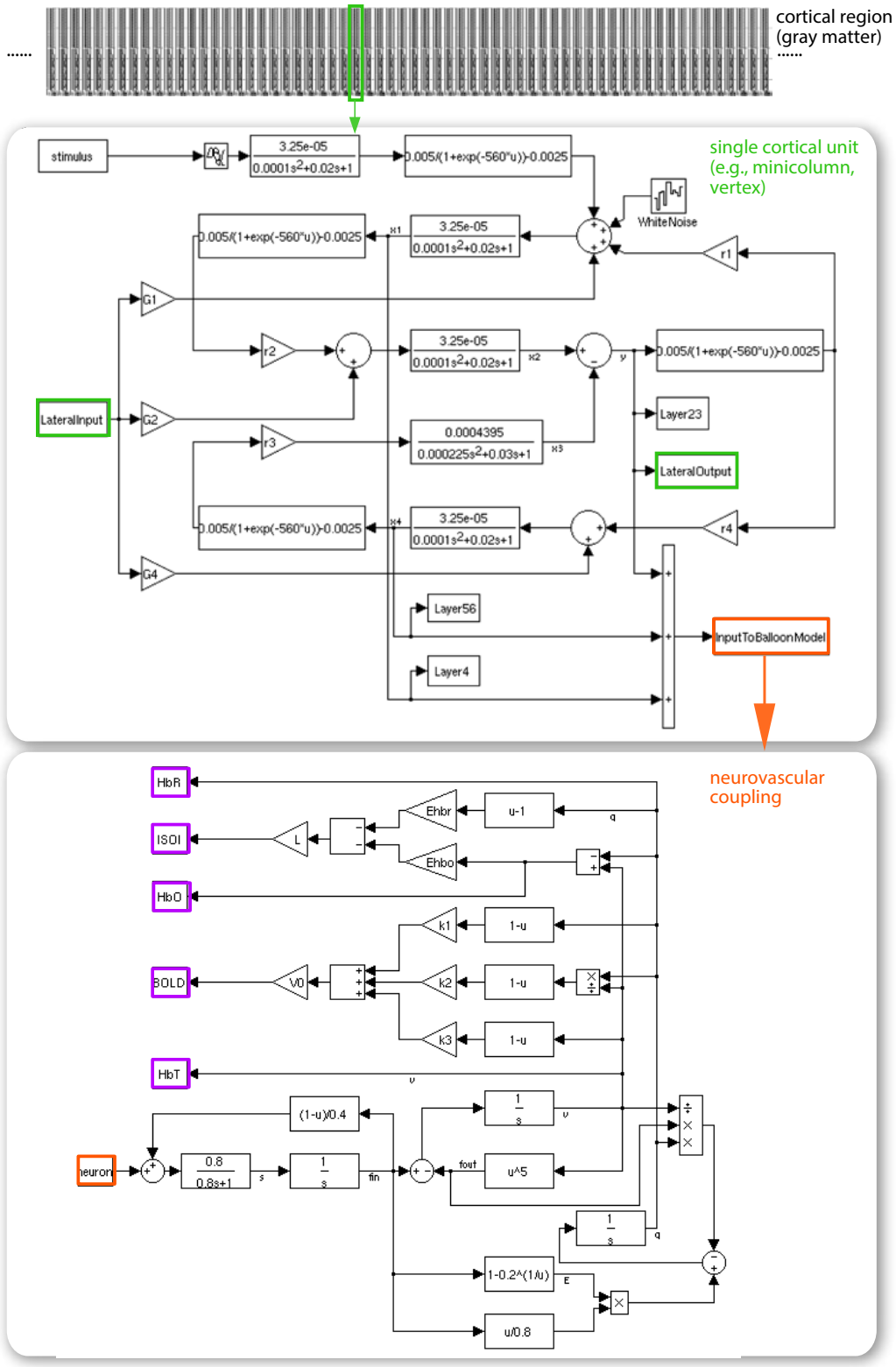

Figure 6.2: Model diagram. The snapshots illustrated the block diagram of the visual cortical model built in MATLAB Simulink. The block diagram was based on Laplace transform to the differential equations in time domain, and it showed the signal flow in the model system as well as the interrelationships among system components.

where the numerator of the transfer function equals to zero) and the poles (the points where the denominator of the transfer function equals to zero). One could also apply the frequency response analysis to visualize the system behavior in Bode plot, Nyquist plot, or Nichols plot [177].

Applying Laplace transform to the differential equations that described the model in the time domain, I acquired the transfer functions that described the model in the complex domain, as well as the block diagram that illustrated the signal flow among different model components (Figure 6.2). Based on this block diagram, I built the neural field model in MATLAB Simulink (simulation solver = Fixed-step Ode4, step size = 0.1 ms), using empirically derived model parameters.

6.3 Results

6.3.1 Simulation of neural responses and hemodynamic responses

As a basic inspection of model performance, I studied the temporal dynamics of the model response and its dependence on the stimulus duration. First, I tested whether the model simulation could capture the profile of neural responses with laminar-layer-specific onset of action potential and the profile of hemodynamic responses with initial dip. A model visual cortex with default surface area (1600 mm^2) and default thickness (2 mm) was simulated by a single pulse stimulus that uniformly activated all the model cortical columns and effectively equaled a full-field visual stimulus. I found that the simulated neural responses captured the temporal profile of action potential (Figure 6.3), where the signal onset at different laminar layers followed the information flow from layer IV to layer II/III to layer V/VI [134, 166, 167, 168, 169]. Moreover, the simulated hemodynamic responses captured the temporal profile of fMRI BOLD signal and optical imaging signal (Figure 6.3), where the signal underwent an initial dip due to the initial increase in deoxyhemoglobin concentration [87, 173].

Next, I tested how the model response was influenced by the stimulus duration. A model visual cortex with default surface area (1600 mm^2) and default thickness (2 mm) was simulated by a repetitive pulse stimulus (frequency: 2 Hz) that lasted from two to twenty-four pulses and effectively equaled a full-field visual stimulus of one to twelve seconds. I found that with the increase in stimulus duration, the amplitude of simulated hemodynamic responses increased and became saturated (Figure 6.4). By contrast, the amplitude of simulated neural responses remained relatively independent from the change in stimulus duration (Figure 6.4). This saturated dependence of hemodynamic response amplitude on stimulus duration was consistent

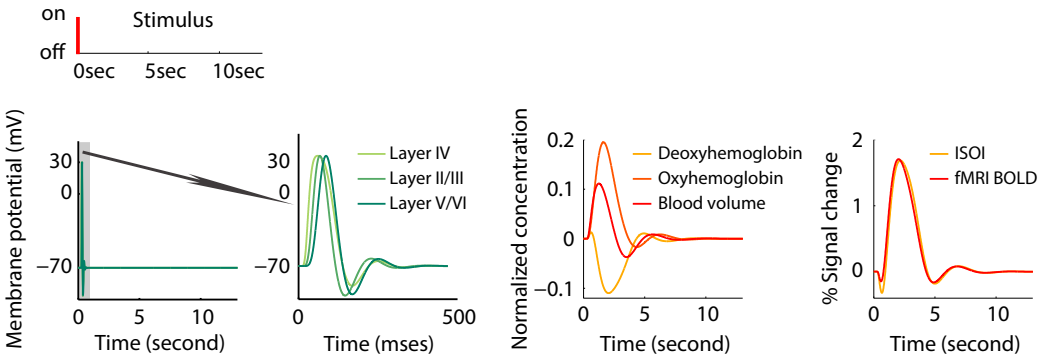

Figure 6.3: Simulation of neural responses and hemodynamic responses. The visual cortical model was simulated with a pulse stimulus. The modeled synaptic activity captured the profile of action potential and its laminar-dependent onset delay that followed the information flow from layer IV to layer II/III to layer V/VI. The modeled fMRI BOLD signal or intrinsic optical imaging signal (ISOI) captured the profile of hemodynamic response including initial dip and undershoot.

with the empirical observations in human early visual cortices [178].

6.3.2 Simulation of visual discrimination and contextual illusion

As a theoretical investigation of intracortical processing, I studied the spatial dynamics of the model response and its dependence on the intracortical scaling. First, I explored whether the scaling of inter-columnar connectivity with model visual cortical surface area could recapitulate the empirically observed relationships between visual cortical surface area and visual perception (Chapter Four), where an increase in visual cortical surface area was found to correlate with a shift in the scope of orientation perception, from a stronger modulation (illusion) by global orientation contexts, to a finer discrimination of local orientation details, and no such correlation with visual cortical surface area was found for luminance or contrast perception.

A model visual cortex with variable surface area (1600 mm^2 to 3400 mm^2) and default thickness (2 mm) was simulated by stimuli corresponding to those used in my psychophysics experiments (Chapter Four, Chapter Five). Specifically, to assess the feature selectivity of the model response (reflecting visual discrimination of local details), the model visual cortex was simulated by a set of stimuli that varied in single feature value (orientation, luminance, contrast). The model response was compared between these stimuli with different feature values, where the difference in the model response increased with the feature difference between these stimuli (Figure 6.5A). This difference in the model response was taken to represent the ability to discriminate these stimuli. The point where the response difference reached 50% was

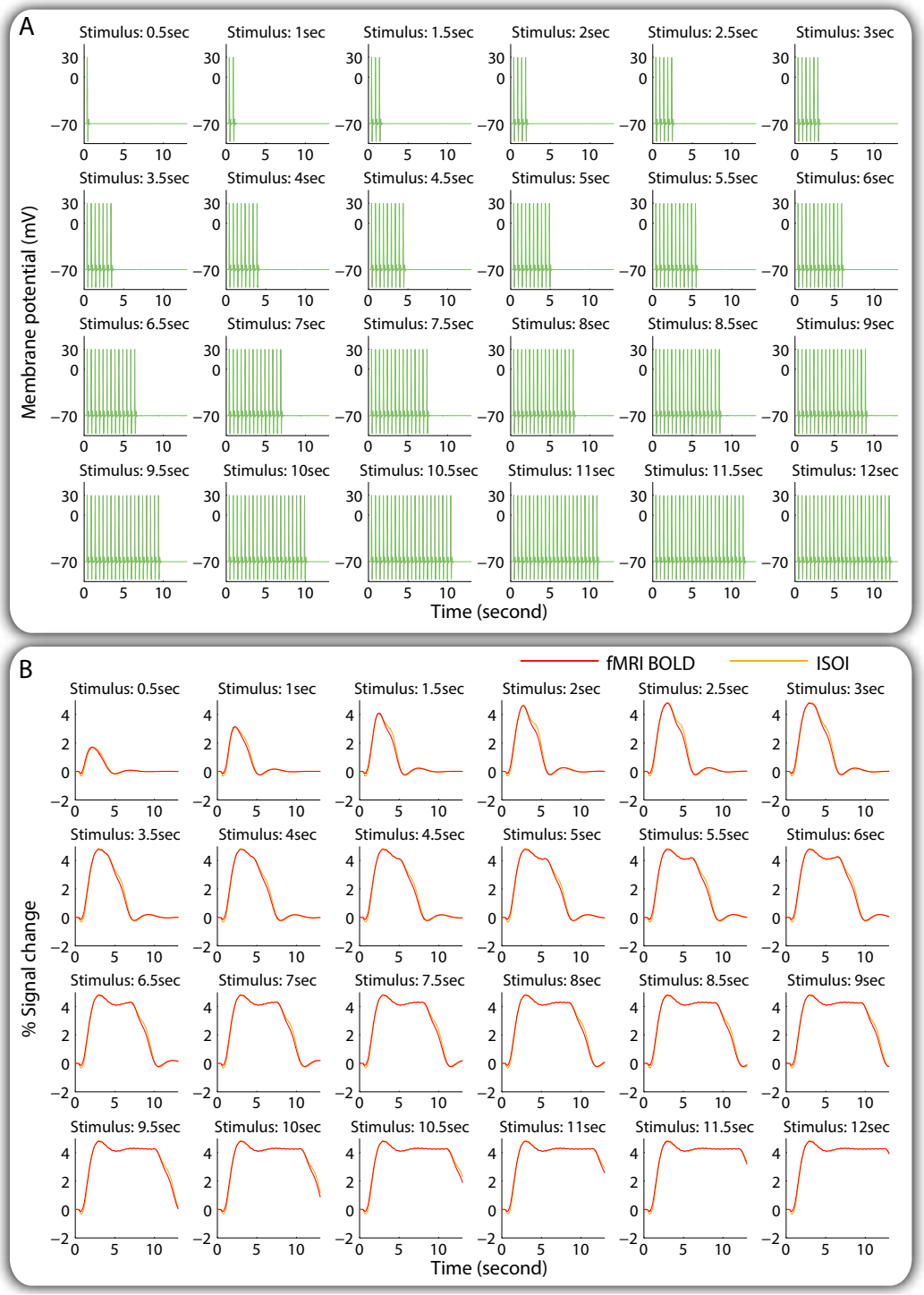

Figure 6.4: Influence of stimulus duration. The visual cortical model was simulated with a repetitive pulse stimulus that repeated every 500 msec for 1 to 24 times and thereby effectively lasted for 0.5 to 12 sec. The amplitude of synaptic activity (A) did not increase with stimulus duration, whereas the amplitude of hemodynamic activity (B) increased with stimulus duration and was consistent with empirical finding [178].

quantified as the model's visual discrimination threshold. To assess the contextual modulation of the model response (reflecting visual illusion induced by global contexts), the model visual cortex was simulated by a central stimulus surrounded in a contextual stimulus of different feature value (orientation, luminance, contrast). The model response to the central stimulus was repulsively shifted by the presence of the contextual stimulus through inter-columnar modulations (Figure 6.5B). This repulsive shift in the model response was taken to represent the phenomenon of contextual illusion, where the perceived feature value of a central stimulus differed from its physical value due to the contextual stimulus. The extent of the response shift was quantified as the model's contextual illusion magnitude.

Mirroring the empirical observations in earlier chapters (Chapter Four, Chapter Five), the surface area of the model visual cortex correlated negatively with the orientation discrimination threshold, but not with the luminance or the contrast discrimination threshold (Figure 6.6). Moreover, a negative correlation was observed between the surface area of the model visual cortex and the orientation contextual illusion magnitude, but no correlation was observed between the surface area of the model visual cortex and the luminance or the contrast contextual illusion magnitude (Figure 6.6). Taken together, the model simulation revealed a trade-off between visual discrimination of local orientation details and visual modulation (illusion) by global orientation contexts, which was not evident in luminance or contrast perception.

Next, I explored whether the scaling of inter-laminar processing time (delay) with model visual cortical thickness could recapitulate the empirically observed relationships between visual cortical thickness and visual perception (Chapter Five), where an increase in visual cortical thickness was found to associate with a lower performance in visual field location discrimination. As a control, I also explored whether the scaling of inter-columnar connectivity with model visual cortical surface area could recapitulate the empirical observations that an increase in visual cortical surface area had the opposite functional impacts as an increase in visual cortical thickness and was associated instead with a higher performance in visual field location discrimination.

A model visual cortex with variable surface area (1600 mm^2 to 3400 mm^2) and variable thickness (1 mm to 4.5 mm) was simulated by stimuli corresponding to those used in my psychophysics experiments (Chapter Four, Chapter Five), and specifically, by a set of stimuli that varied in visual field locations. The model response was compared between stimuli at different visual field locations, and the point where the difference in the model response reached 50% was quantified as the model's location discrimination threshold. The model simulation revealed

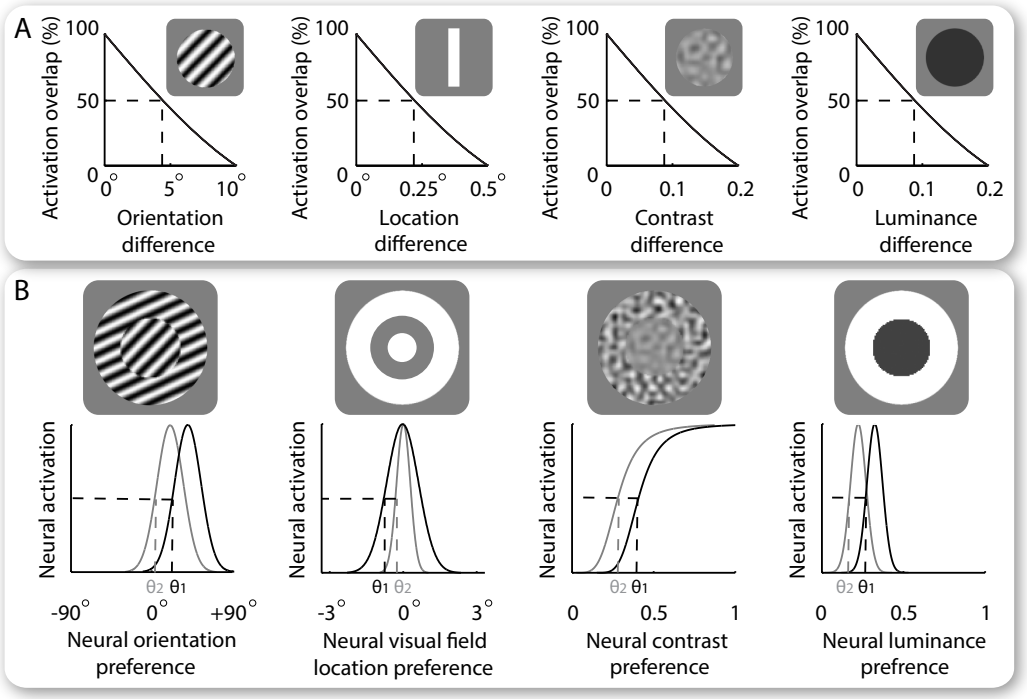

Figure 6.5: Simulation of visual discrimination and contextual illusion. (A) To quantify visual discrimination threshold, the visual cortical model was simulated with a set of stimuli that differed in only a single feature (orientation, location, contrast, luminance). The activation pattern of the model visual cortex was compared for different stimuli along each feature dimension, where the degree of overlap in activation pattern decreased with the feature difference between stimuli. The feature difference at the threshold where the activation overlap decreased to 50% was quantified as the model's visual discrimination threshold. (B) To quantify contextual modulation magnitude, the visual cortical model was simulated with contextual illusion stimuli where a circular stimulus was surrounded by an annular stimulus. The response of model neurons to the circular stimulus was modulated by the response of their neighboring neurons to the annular stimulus, where the inhibitory connections from neighboring neurons caused a repulsive shift in the model's response to the circular stimulus (from black to grey line). The extent of this shift was quantified as the model's contextual modulation magnitude.

an increase in location discrimination threshold with model visual cortical thickness and a decrease in location discrimination threshold with model visual cortical surface area (Figure 6.7).

6.4 Discussion

In summary, my study revealed that a visual cortical model based on intracortical processing was able to reproduce the profile of neural and hemodynamic responses, as well as

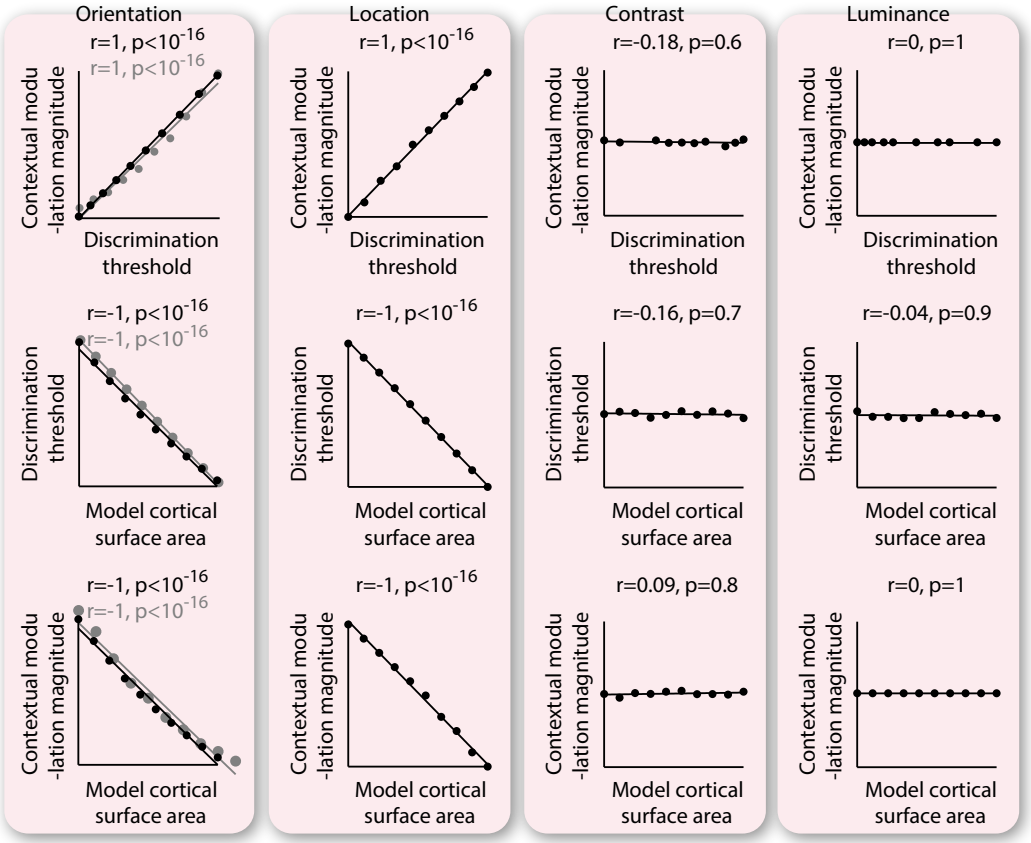

Figure 6.6: Influence of visual cortical surface area. The surface area of the model visual cortex was varied to investigate its influence on the model's visual discrimination threshold and contextual modulation magnitude. When the model visual cortex expanded in surface area, the cortical representation of visual field location expanded accordingly, and the cortical representation of orientation expanded as well through an increase in either the number or the size of orientation hypercolumns (the simulation results of which were marked with black and grey color respectively). Mirroring the empirical observations, the model simulations revealed a tradeoff between discrimination threshold and contextual modulation magnitude that correlated with the surface area of the model visual cortex. This tradeoff and its correlation with the model visual cortical surface area were only evident in the domain of orientation or visual field location, and were not observed in the domain of luminance or contrast. Each point represents a single simulation (N = 10) and the line is the best-fitting linear regression. Statistical values reflect Spearman's rho with FDR correction for multi-comparisons (α = 0.025).

to capture the empirically observed relationships between visual cortical anatomy and visual perception. First, I showed that the visual cortical model reproduced the profile of neural responses with laminar-layer-specific onset of action potential, as well as the profile of hemodynamic responses with initial dip and amplitude saturation. These basic inspections of model

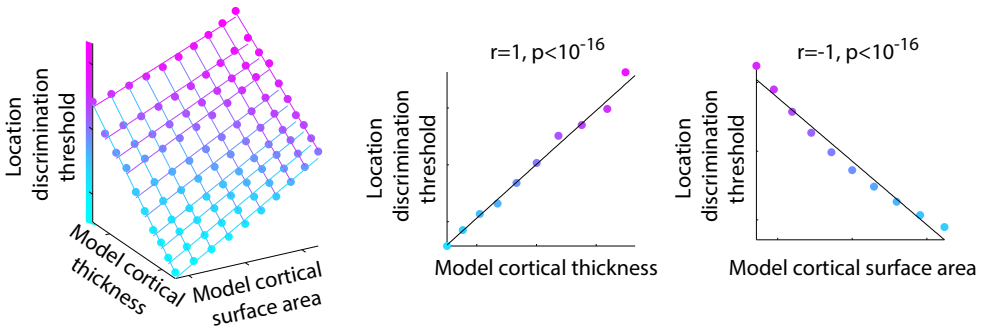

Figure 6.7: Influence of visual cortical thickness. The surface area and the thickness of the model visual cortex were varied to compare their influences on the model's location discrimination threshold. When the model visual cortex expanded in surface area, the inter-columnar connectivity was weakened, and when the model visual cortex increased in thickness, the inter-laminar processing time (delay) was lengthened. Mirroring the empirical observations, the model simulations revealed a positive correlation between the location discrimination threshold and the model visual cortical thickness as well as a negative correlation between the location discrimination threshold and the model visual cortical surface area. Data points are color coded according to the location discrimination threshold. Each point represents a single simulation (N = 10) and the line is the best-fitting linear regression. Statistical values reflect Spearman's rho with FDR correction for multi-comparisons (α = 0.025).

performance demonstrated the validity of theoretical simulation. Building upon this, I showed that the simulated scaling of inter-columnar connectivity with model visual cortical surface area and the simulated scaling of inter-laminar processing time with model visual cortical thickness were able to capture the empirical observations, where an increase in visual cortical surface area was found to associate with a perceptual shift from global context-oriented to local detail-oriented, for elementary visual features with a continuous orderly cortical representation (Chapter Four), and an increase in visual cortical thickness was found to have the opposite functional impacts (Chapter Five).

The model simulation suggests that through the scaling of intracortical processing, visual cortical anatomy selectively influences perception of elementary visual features that have a continuous, orderly cortical representation. For such visual features, the weakening of inter-columnar connectivity with increasing visual cortical surface area would lower the synchronization between cortical columns responsive to similar feature values, and in turn shift the scope of visual neural responses or the scope of visual perception from a stronger modulation by global contexts to a finer selectivity of local details. By contrast, the lengthening of inter-

laminar processing time with increasing visual cortical thickness would facilitate response synchronization between cortical columns, and in turn shift the scope of visual neural responses or the scope of visual perception in the opposite direction. On the other hand, for visual features without a continuous, orderly cortical representation, the influence on the synchronization between cortical columns responsive to similar feature values would be counter-balanced by that between cortical columns responsive to opposite feature values, and in turn lead to no net change in the scope of visual neural responses or the scope of visual perception. Therefore, the nonlinear scaling of intracortical processing with the similarity in feature selectivity between connected cortical columns may be the mechanism through which visual cortical anatomy influences visual perception.

In the model, visual cortical thickness influences visual perception via inter-laminar processing time. The variability in cortical thickness would not make much difference to the absolute value of inter-laminar processing time (e.g., for a conduction speed of 1mm/ms, a cortex that is 1mm thick would gain only 1ms compared to a cortex that is 2mm thick). However, this is not incompatible with my hypothesis. The hypothesis I tested in my model was that, the decrease in inter-laminar processing time with cortical thickness would facilitate the de-synchronization among different cortical columns and in turn increase the feature selectivity of individual cortical column. As such, compared to the absolute value of inter-laminar processing time, the relative value of inter-laminar to inter-columnar processing time would be more relevant. Since the inter-laminar and the inter-columnar distances are on the same scale, the change in inter-laminar processing time with cortical thickness would not be entirely trivial to intracortical processing.

While the visual cortical model reliably captures the profile of neural responses and reproduces my empirical observations, it is important to note that as with other theoretical studies, the model is based on assumptions not fully validated. This is particularly the case given that the relationships between macroscopic-level cortical anatomy (surface area, thickness) and microscopic-level neural parameters (column number, conduction speed) remain largely unclear. Specifically, the model is based on the assumption that the length of intracortical connections is physically constrained and remains relatively independent of the change in visual cortical anatomy, as such, an increase in visual cortical thickness would be associated with an increase in inter-laminar processing time, whereas an increase in visual cortical surface area would be associated with a decrease in inter-columnar connectivity (i.e., a decrease in the proportion of cortical columns with which an individual cortical column connects). Although

these assumptions are biologically plausible, especially in comparison to their oppositions such as an association between larger visual cortical thickness and shorter inter-laminar processing time, there are in reality many other plausible assumptions that are not fully addressed in the model.

Therefore, at its best, the visual cortical model served as a proof of concept for the possible mechanisms underlying the empirically observed correlations between visual cortical anatomy and visual perception. To provide support for the model, I further conducted an empirical test of the predictions from the model. In particular, the model suggested that visual cortical anatomy might influence the performance in visual discrimination through the feature selectivity of visual cortical neurons that was in turn shaped by the intracortical processing. As such, the feature selectivity of visual cortical neurons would exhibit opposite dependence on visual cortical thickness versus visual cortical surface area, and a higher selectivity would be associated with a smaller visual cortical thickness or a larger visual cortical surface area. This hypothesis was tested empirically in the next chapter (Chapter Seven), where I measured the feature selectivity of visual cortical neurons through non-invasive neuroimaging methods and explored its dependence on visual cortical anatomy.

Regardless of these efforts, the model provided only a theoretical support for the involvement of intracortical processing in linking visual cortical anatomy to visual perception. To further address the role of intracortical processing, it would be helpful to acquire an empirical measure. However, given the limited resolution of non-invasive neuroimaging methods, a direct measure of intracortical processing (e.g., connectivity, processing time) in human participants is difficult. Nevertheless, the method of Dynamic Causal Modeling allows an indirect estimate of intracortical connectivity from non-invasive neuroimaging signals that reflects the effective strength of intracortical connections from one neural population to another [80]. Therefore, in the chapter after next (Chapter Eight), I measured the intracortical connectivity in early visual cortices using the method of Dynamic Causal Modeling, and explored whether the weakening of intracortical connectivity indeed shifted the scope of visual perception from global context-oriented to local detail-oriented.

Chapter 7

Role of Visual Neural Selectivity

7.1 Introduction

My experiment observations in the last few chapters (Chapter Three / Four / Five) revealed a substantial degree of variability in the anatomy (surface area, thickness) of early visual cortices that gave rise to the variability in perception of elementary visual features. Parallel to my experiment observations, several recent studies have reported correlations between cortical anatomy and behavioral performance [1]. These observations suggested that the anatomical variability in cerebral cortex is not a genetic-developmental artifact, but is instead of neurobiological relevance and behavioral significance. Despite these progresses, the influence of anatomical variability on neural response properties is unclear. Moreover, it remains unexplored whether it is through the mediation by neural responses that the cortical anatomy gets to influence the behavioral performance.

Such lack of understanding may result from the limitation in non-invasive measure of neural response properties. Indeed, given the resolution of fMRI BOLD signals, different neurons within a single voxel tend to exhibit heterogeneous responses that render the neural population responses qualitatively different from the single neural responses. For example, neurons in early visual cortices respond selectively to a variety of visual features including visual field location, orientation, contrast, luminance, and many others. However, the neural responses to most of these visual features have either no orderly cortical representation or a periodic cortical representation beyond the resolution of fMRI BOLD signals [97]. Consequently, a single voxel usually contains neurons selective for opposite feature values, which in turn leads to a discrepancy between neural population selectivity and single neural selectivity.

An exception to this limitation is the responses of early visual cortical neurons to visual field location. Neurons in early visual cortices respond selectively to visual field location in an

orderly, continuous fashion where cortically adjacent neurons are selective for spatially adjacent visual field locations [39, 71]. Such response similarity between different neurons within a single voxel allows the estimation of single neural selectivity from the measure of neural population selectivity. Specifically, neural population selectivity for visual field location can be measured from fMRI BOLD signals using the method of population-receptive-field mapping, which, by presenting a visual stimulation at sixty-four evenly distributed visual field locations, estimates the visual field range to which a single voxel responds [122]. This measure of visual field response range represents neural population selectivity for visual field location, where a small (localized) response range corresponds to a high selectivity and a large (globalised) response range corresponds to a low selectivity.

Utilizing the method of population-receptive-field mapping, I explored the influence of visual cortical anatomy on neural population selectivity for visual field location and tested three different hypotheses. My theoretical (model) study in the last chapter (Chapter Six) suggests that the feature selectivity of visual cortical neurons mediates the empirically observed influence of visual cortical anatomy on visual perception, where a larger visual cortical surface area is associated with a finer visual discrimination and a larger visual cortical thickness is associated instead with a poorer visual discrimination. Therefore, mirroring the correlations between visual discrimination and visual cortical anatomy, neural population selectivity would correlate positively with visual cortical surface area but negatively with visual cortical thickness. This hypothesis suggests an opposition between visual cortical surface area and visual cortical thickness in their influence on neural population selectivity. Alternatively, it is possible that neural population selectivity is determined by visual cortical volume and therefore exhibits the same relationship with visual cortical surface area as with visual cortical thickness. Equally, it is plausible that neural population selectivity neither relates with visual cortical anatomy nor mediates the influence of visual cortical anatomy on visual discrimination.

To test these hypotheses, I compared visual cortical thickness and visual cortical surface area in their contribution to neural population selectivity for visual field location. The thickness of early visual cortices, determined independently for individual visual cortical locations, exhibited a substantial degree of intra-individual variability and reflected differences between visual field locations in the cortical architecture at corresponding visual cortical locations. By contrast, the surface area of early visual cortices, determined jointly by all visual cortical locations, exhibited a substantial degree of inter-individual variability and reflected differences between individuals in the proportion of cortex devoted to early visual processing. Therefore,

I studied how the thickness at individual visual cortical locations related to neural population selectivity for corresponding visual field locations, and how the surface area summed over different visual cortical locations influenced neural population selectivity across the visual field in general.

Taken together, in this chapter, I explored the relationships between visual cortical anatomy and neural population selectivity in healthy human adults with three specific aims. First, using the method of population-receptive-field mapping, I measured neural population selectivity for visual field location from fMRI BOLD signals, and assessed how this measure was confounded by fMRI signal properties. Then, based on this measure, I studied the variability in neural population selectivity along the visual field eccentricity (eccentricity-dependent component) and across different visual field locations at the same eccentricity (eccentricity-independent component). Last, I addressed the contribution of visual cortical thickness and visual cortical surface area to the variability in neural population selectivity, separately for its eccentricity-dependent and its eccentricity-independent component. To this end, I acquired the measure of neural population selectivity for visual field location from high spatial resolution (1.5 mm) fMRI data, and quantified fMRI signal properties from high temporal resolution (1.52 second) fMRI data. I also assessed the variability in visual cortical anatomy using T1-weighted structural MRI data.

7.2 Methods

7.2.1 Participants and Apparatus

A group of twenty healthy participants (aged 19 to 34, ten females, ten males), with normal or corrected-to-normal vision and no neurological history, gave written informed consent to take part in this study approved by the UCL ethics committee. All participants took part in the main experiments where I assessed visual cortical anatomy using T1-weighted structural MRI data, and measured neural population selectivity for visual field location using high spatial resolution (1.5 mm) fMRI data. Eight of the participants took part in the control experiments where I assessed fMRI signal properties using high temporal resolution (1.52 second) fMRI data.

The experiments took place in a Siemens Trio 3T MRI scanner with a 32-channel head-coil. The visual stimuli were projected onto a screen (size = 28.6 x 21.5 cm) in the back of the scanner and viewed through a mirror on the head-coil (viewing distance = 85 cm). The stimuli covered a portion of the visual field extending from 0.25 to 7.2 degree eccentricity. Structural

MRI data were collected using a T1-weighted sequence at 1 mm resolution (TR = 7.92 ms, TE = 2.48 ms, matrix = 256 x 240). In the main experiments, functional MRI data were collected using a 3D EPI sequence at 1.5 mm and 3.2 second resolution (volume TR = 3.2 s, TE = 32.86 ms, matrix = 128 x 128). In the control experiments, functional MRI data were first collected using the same 3D EPI sequence at 1.5 mm and 3.2 second resolution, then repeated with a new 3D EPI sequence at 1.5 mm and 1.52 second resolution (volume TR = 1.52 s, TE = 37.3 ms, matrix = 128 x 128). The high temporal resolution (1.52 second) of the 3D EPI sequence allowed fine estimation of fMRI signal properties, but was accompanied by a reduced field-of-view as a trade-off. To accommodate the reduced field-of-view, the data for the left and the right hemispheres were collected separately in different experimental runs. Functional MRI data were preprocessed in SPM8 through bias correction, realignment, unwarping, coregistration, and physiology noise correction.

7.2.2 Measure of visual cortical anatomy

Standard phase-encoded retinotopic mapping was applied to delineate early visual cortices (V1, V2), where each participant took part in two experiment runs of polar-angle mapping and one experiment run of eccentricity mapping. For polar-angle mapping, participants viewed full-contrast flickering checkerboard wedges (width = 40 degree) rotating smoothly around a small fixation cross for ten cycles per experiment run at a speed of twenty volumes per cycle. For eccentricity mapping, participants viewed full-contrast flickering checkerboard rings (width = 7.8% of the screen length) contracting smoothly around a small fixation cross for fifteen cycles per experiment run at a speed of fifteen volumes per cycle. To maintain participants' attention, at random temporal intervals the retinotopic mapping stimuli underwent a small pattern shift for 200 ms. Participants were asked to indicate whenever this happened with a button press while maintaining eye fixation at the central cross.

The polar-angle maps and the eccentricity maps were generated by applying Fast Fourier Transform to fMRI BOLD time series of each voxel that extracted the phase and the power at the stimulation frequency. The polar angle boundaries (representing vertical and horizontal meridians) were delineated according to the mirror reversals in the polar-angle maps. The eccentricity boundaries (representing 7.2 degree eccentricity) were delineated by thresholding the eccentricity maps. Based on the retinotopic delineation of early visual cortices, the thickness at individual visual cortical locations and the surface area summed over all visual cortical locations were measured through the surface-based analysis on structural MRI data. In the surface-based analysis, structural MRI data were preprocessed using skull stripping and non-

uniform intensity correction, after which the data were segmented into the white and the gray matter according to intensity-based tissue classification. From the white and the gray matter segments, the three-dimensional triangle-mesh models of the white and the pial cortical surfaces were built, with the cortical thickness computed as the distance between the white and the pial cortical surfaces, and the cortical surface area computed as the summed surface area of triangle faces in a cortical region.

7.2.3 Measure of neural selectivity

Population-receptive-field mapping was applied to measure neural population selectivity for visual field location, where each participant took part in two experiment runs. In a single experiment run, participants viewed full-contrast flickering checkerboard bars (width = 1.8 degree of visual angle) moving smoothly in the visual field for eight cycles at a speed of sixteen volumes per cycle (one visual field location per volume, sixty-four different visual field locations, each visual field location repeated twice). The bars were oriented at one of the four orientations (horizontal, vertical, 45 degree, 135 degree) and moved along the corresponding orthogonal direction (north/south for horizontal bar, west/east for vertical bar, northwest/southeast for 45 degree bar, northeast/southwest for 135 degree bar), where the orientation and the moving direction were counterbalanced across cycles. A blank screen was inserted into the last quarter of the second, fourth, sixth, and eighth cycle to provide a baseline condition that improved the measurement accuracy. To maintain participants' attention, at random temporal intervals the central fixation cross underwent a color change for 80 ms. Participants were asked to indicate whenever this happened with a button press while maintaining eye fixation at the central cross.

The fMRI BOLD time series of each voxel were deconvolved with a canonical hemodynamic response function $h(t) = (t/5.4)^6 e^{-(t-5.4)/0.9} - 0.35 * (t/10.8)^{12} e^{-(t-10.8)/0.9}$ [123, 124] and then fitted with a two-dimensional Gaussian function f(x_0, y_0, σ) multiplied by the stimulus location function. The two-dimensional Gaussian function characterized the visual field range (σ) to which the voxel responded and the visual field location (x_0, y_0) to which the voxel responded the strongest. The parameters x_0, y_0 (limit = 7.2 degree eccentricity) and σ (lower limit = 0.001 degree of visual angle, upper limit = 7.2 degree of visual angle) were estimated for each voxel by finding the least square fit. The measure of visual field response range (σ) represented neural population selectivity for visual field location, where a small (localized) response range indicated a high selectivity and a large (globalized) response range indicated a low selectivity. Therefore, the inverse of this visual field response range ($1/\sigma$)

was used to quantify neural population selectivity for visual field location.

7.2.4 Measure of fMRI signal properties

Although the method of population-receptive-field mapping allowed a non-invasive measure of neural population selectivity from fMRI BOLD signals, the measure was confounded by fMRI signal properties, including the signal-to-noise ratio and the hemodynamic response function. To assess these potential confounding influence, in control experiments I measured the signal-to-noise ratio from the resting state BOLD responses, and the hemodynamic response function from the visually evoked BOLD responses. These control data were collected using the 3D EPI sequence at 3.2 second and 1.52 second resolution, in separate experiment runs.

To quantify the signal-to-noise ratio, the resting state BOLD responses were collected for a continuous 10 minutes, during which participants maintained awake through eye fixation at a central cross on a black screen under the monitor of an eye tracker. From the resting state data, the signal-to-noise ratio was calculated for each voxel as the mean divided by the standard deviation of the fMRI BOLD time series [179]. The signal-to-noise ratio was calculated respectively before and after the application of physiological noise correction. To measure the hemodynamic response function, the visually evoked BOLD responses were collected using the 3D EPI sequence at 3.2 second resolution or the 3D EPI sequence at 1.52 second resolution, during which a full-contrast flickered checkerboard ring (inner radius = 0.25 degree eccentricity, outer radius = 7.2 degree eccentricity) was presented on the screen for 3.2 or 3.04 second, followed by a blank screen of 28.8 or 27.36 second, and repeated for 20 or 40 cycles. Participants maintained their attention and fixation by detecting color change of the central fixation cross. From the visually evoked data, the hemodynamic response function $h(t) = (t/t_1)^{(5.6*t_1^2/w_1^2)}e^{-(t-t_1)*(5.6*t_1/w_1^2)} - d*(t/t_2)^{(5.6*t_2^2/w_2^2)}e^{-(t-t_2)*(5.6*t_2/w_2^2)}$ was estimated for each voxel by varying the peak t_1, t_2 (limit = 12 second), the full-width-half-maximum w_1, w_2 (limit = 30 second), and the dip d (limit = 1) to find the least square fit.

7.3 Results

7.3.1 Measurement confound for neural selectivity

The measure of neural population selectivity for visual field location was based on the method of population-receptive-field mapping [122]. By presenting visual stimulation at a set of evenly distributed visual field locations, the method assessed, for each voxel, the visual field

range to which it responded. This visual field response range represented neural population selectivity for visual field location, where a small (localized) response range corresponded to a high selectivity and a large (globalised) response range corresponded to a low selectivity. Therefore, the inverse of this visual field response range was used to quantify neural population selectivity for visual field location.

However, limited by the spatial resolution of fMRI BOLD signals, the measure of neural population selectivity for visual field location reflected a combined contribution from single neural selectivity and the response heterogeneity between different neurons within a voxel. To lower the intra-voxel response heterogeneity, I collected fMRI data at a high spatial resolution (1.5 mm). For tissue volumes as small as 1.5 mm, the response heterogeneity between different neurons in the tissue volume was smaller than single neural selectivity and correlated with the average of single neural selectivity in the tissue volume [39]. As such, the measure of neural population selectivity in effect reflected single neural selectivity. Indeed, neural population selectivity measured here in human early visual cortices (0.6 ± 0.35 degree of visual angle) was comparable with single neural selectivity in macaque visual cortices (0.35 degree of visual angle) [39].

In addition to lowering the intra-voxel response heterogeneity, the high spatial resolution of fMRI data also contributed to minimizing the inter-voxel heterogeneity in spatial sampling. To evaluate the influence of spatial sampling, three different voxels, at upper, middle, and lower cortical layers, were sampled for each visual cortical location with a high cortical thickness, two different voxels, at upper and lower cortical layers, were sampled for each visual cortical location with a medium cortical thickness, and one voxel was sampled for each visual cortical location with a low cortical thickness (Figure 7.1). At visual cortical locations where more than one voxel was sampled, the measure of neural population selectivity was compared across voxels from different cortical depths. This analysis revealed that the exact cortical depth of the sampled voxel did not affect the measure.

Together the control studies above suggested that the measure of neural population selectivity for visual field location was not biased by the spatial resolution of fMRI BOLD signals. Apart from confound in spatial domain, the measure was confounded in temporal domain by the neurovascular coupling between neural responses and hemodynamic responses. This confound was taken into consideration during the analysis, where the fMRI BOLD time series of each voxel were deconvolved with a canonical hemodynamic response function before fitting with the two-dimensional Gaussian characterization of neural population selectivity. Since the

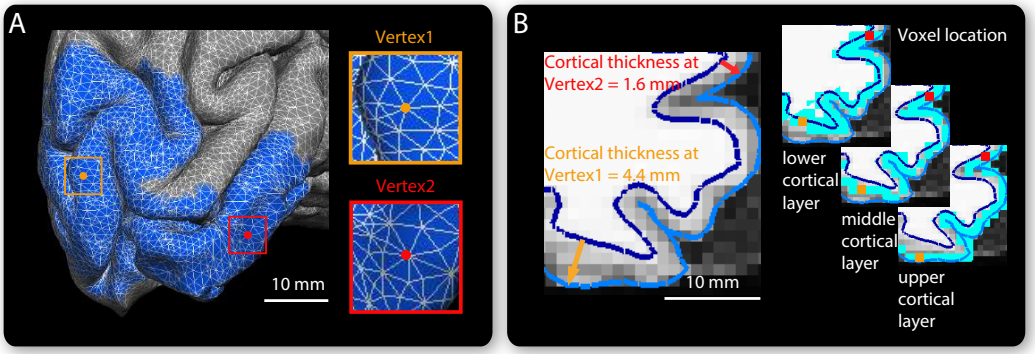

Figure 7.1: MRI measure of neural selectivity. The triangle-mesh model illustrated the three-dimensional cortical surface reconstruction in a representative participant, where individual vertex of this triangle-mesh model represented a single cortical surface location separable by MRI (A). To assess the influences of fMRI spatial sampling on the measure of neural population selectivity, three different voxels, at upper, middle, and lower cortical layers, were sampled for each cortical surface location with high thickness, two different voxels, at upper and lower cortical layers, were sampled for each cortical surface location with medium thickness, and one voxel was sampled for each cortical surface location with low thickness (B).

fMRI BOLD time series had a temporal resolution (3.2 second) larger than the full-width-half-maximum and the time-to-peak of the hemodynamic response function, the effective hemodynamic response function, namely the discrete function sampled every 3.2 second, was a Dirac delta function that lagged the measure of visual field response peak uniformly for all voxels without influencing the measure of visual field response range. Therefore, in theory, the measure of neural population selectivity for visual field location reflected the neural rather than the hemodynamic contributions.

Nevertheless, to improve the reliability of the measure, I conducted a control analysis where I replaced the canonical hemodynamic response function in the original analysis with a voxel-level estimated hemodynamic response function. In the control analysis, the visually evoked BOLD responses were collected, from which the hemodynamic response function was estimated for each voxel by varying the parameters (t_1, t_2, w_1, w_2, d) to find the least square fit. This voxel-level estimated hemodynamic response function was then applied to reanalyze the data from the population-receptive-field mapping experiment, where the fMRI BOLD time series of each voxel were deconvolved with this voxel-level estimated hemodynamic response function before fitting with the two-dimensional Gaussian characterization of neural population selectivity. I found that the measure of neural population selectivity was highly consistent between the original analysis using the canonical hemodynamic response and this control anal-

ysis using the voxel-level estimated hemodynamic response function (r = 0.9355, p $<$ 0.0001, N = 42538 voxels binned into N = 30 data points). Moreover, the parameters of this voxel-level estimated hemodynamic response function (mean of t_1 = 5.4, mean of t_2 = 10.7, mean of w_1 = 5.3, mean of w_2 = 7.8, mean of d = 0.36) were close in value to the parameters of the canonical hemodynamic response function (t_1 = 5.4, t_2 = 10.8, w_1 = 5.2, w_2 = 7.4, d = 0.35), suggesting that the canonical hemodynamic response function was representative of the voxel-level estimated hemodynamic response function.

Despite these efforts, both the original analysis and the control analysis replied on the application of the hemodynamic response model $h(t, t_1, t_2, w_1, w_2, d)$. To test whether the choice of hemodynamic response model might confound the measure of neural population selectivity for visual field location, I conducted a further analysis using a hemodynamic-model-free approach. In this analysis, the fMRI BOLD time series from the population-receptive-field mapping experiment were deconvolved directly with the visually evoked BOLD responses (rather than with the hemodynamic response function estimated from the visually evoked BOLD responses) before fitting with the two-dimensional Gaussian characterization of neural population selectivity. I found that the measure of neural population selectivity exhibited high level of consistency between this hemodynamic-model-free analysis and the hemodynamic-model-dependent analysis (r = 0.9394, p $<$ 0.0001, N = 42538 voxels binned into N = 30 data points), suggesting that the measure was not affected by the choice of hemodynamic response model.

Together the consistency between the analysis using the canonical hemodynamic response function, the analysis using the voxel-level estimated hemodynamic response function, and the hemodynamic-model-free analysis suggested that the measure of neural population selectivity for visual field location was not biased by the neurovascular coupling between neural responses and hemodynamic responses. In addition to confound in spatial or temporal domain, the measure was confounded by the signal-to-noise ratio of fMRI data. To address this confound, in control experiments I measured the signal-to-noise ratio from the resting state BOLD responses, independently for each voxel. Across voxels, I found that the signal-to-noise ratio did not vary with the measure of neural population selectivity (r = -0.229, p = 0.114, N = 42538 voxels binned into N = 30 data points). Moreover, while the physiological noise correction improved the signal-to-noise ratio by 35.95%, the degree of improvement did not correlate with the measure of neural population selectivity (r = -0.219, p = 0.144, N = 42538 voxels binned into N = 30 data points). These analyses suggested that the measure of neural population

selectivity for visual field location was not biased by the signal-to-noise ratio of fMRI data.

7.3.2 Variability in neural selectivity

These control studies reassured the reliability of population-receptive-field method in measuring neural population selectivity for visual field location. Based on this, I studied the variability in neural population selectivity. Consistent with previous reports [122], I observed an intra-individual decrease in neural population selectivity along the visual field eccentricity from parafovea to perifovea, for both sulci (V1: T = 20.894, $p < 0.0001$, N = 20 participants; V2: T = 22.849, $p < 0.0001$, N = 20 participants) and gyri (V1: T = 16.458, $p < 0.0001$, N = 20 participants; V2: T = 20.240, $p < 0.0001$, N = 20 participants). In addition to this eccentricity-dependent change, neural population selectivity also varied intra-individually across different visual field locations at the same eccentricity. Moreover, even for the same visual field location, neural population selectivity still exhibited a substantial degree of variability across participants.

Therefore, resembling the variability in visual discrimination threshold, the variability in neural population selectivity could be decomposed into an eccentricity-dependent and an eccentricity-independent component. Correspondingly, I conducted separate analysis to address, the influence that the anatomy (thickness, surface area) of early visual cortices (V1, V2) exerted on the change in neural population selectivity along the visual field eccentricity (eccentricity-dependent component), and the influence that the anatomy (thickness, surface area) of early visual cortices (V1, V2) exerted on the variability in neural population selectivity across different visual field locations at the same eccentricity (eccentricity-independent component).

7.3.3 Visual cortical anatomy and neural selectivity at fixed eccentricity

To control for the factor of eccentricity and explore the influence of V1 anatomy on the eccentricity-independent variability in V1 neural population selectivity, I analyzed the relationships between V1 anatomy and V1 neural population selectivity at a fixed visual field eccentricity (4.7 degree). Similar to the analysis on the relationships between V1 anatomy and visual discrimination threshold, I plotted V1 neural population selectivity for six different visual field locations (45, 90, 135, 225, 270, 315 degree in polar angle) from the same eccentricity (4.7 degree) against the thickness at corresponding V1 locations or the surface area of participants' V1, across the group of twenty participants.

I found that neural populations in V1 with a larger surface area exhibited a higher se-

lectivity (r = 0.249, 95% CI = [0.074, 0.409], $p < 0.01$, N = 20 participants x 6 visual field locations). In contrast to this positive correlation with V1 surface area, V1 neural population selectivity correlated negatively with V1 thickness, where neural populations at V1 locations with a greater thickness exhibited a lower selectivity (r = -0.465, 95% CI = [-0.59, -0.31], $p < 0.0001$, N = 20 participants x 6 visual field locations). This negative correlation between V1 neural population selectivity and V1 thickness reflected a combined contribution of intra-individual and inter-individual factors. To separate the contribution of the two factors, I conducted further analysis where I calculated, for each participant, V1 neural population selectivity as well as V1 thickness averaged across the six visual field locations, and for each visual field location, V1 neural population selectivity as well as V1 thickness averaged across the twenty participants. By subtracting the averages of individual participants', I factored out inter-individual variability and studied the contribution of intra-individual factor. Similarly, by subtracting the averages of individual visual field locations', I factored out intra-individual variability and studied the contribution of inter-individual factor. The analysis revealed that the negative correlation between V1 neural population selectivity and V1 thickness existed both within individuals (r = -0.394, 95% CI = [-0.54, -0.23], $p < 0.0001$, N = 20 participants x 6 visual field locations) and across individuals (r = -0.423, 95% CI = [-0.56, -0.26], $p < 0.0001$, N = 20 participants x 6 visual field locations).

These correlations suggested that V1 neural population selectivity for a specific visual field location was affected jointly by the thickness at corresponding V1 locations and the surface area of V1, where the exact influence on V1 neural population selectivity opposed between V1 thickness and V1 surface area. To explore the influence that V2 anatomy might exert on V2 neural population selectivity, I applied a similar analysis, where I plotted V2 neural population selectivity for six different visual field locations (45, 90, 135, 225, 270, 315 degree in polar angle) from the same eccentricity (4.7 degree) against the thickness at corresponding V2 locations or the surface area of participants' V2. Similar to the observations in V1, I found that V2 neural population selectivity correlated positively with V2 surface area (r = 0.295, 95% CI = [0.123, 0.450], $p < 0.01$, N = 20 participants x 6 visual field locations) but negatively with V2 thickness (r = -0.322, 95% CI = [-0.47, -0.15], $p < 0.001$, N = 20 participants x 6 visual field locations; intra-individually, r = -0.366, 95% CI = [-0.51, -0.20], $p < 0.0001$, N = 20 participants x 6 visual field locations; inter-individually, r = -0.276, 95% CI = [-0.43, -0.11], $p < 0.01$, N = 20 participants x 6 visual field locations).

7.3.4 Visual cortical anatomy and neural selectivity along eccentricity

My analyses above at a fixed visual field eccentricity (4.7 degree) suggested that the thickness and the surface area of human early visual cortices (V1, V2) had joint but opposite influence on the variability in neural population selectivity across different visual field locations at the same eccentricity (eccentricity-independent component). To study whether this observation was specific to certain visual field eccentricity or was generalisable across the visual field, I compared visual cortical thickness and visual cortical surface area in their contribution to the variability in neural population selectivity along the visual field eccentricity (eccentricity-dependent component). Specifically, by fitting neural population selectivity as a function of visual field eccentricity, I explored how visual cortical anatomy (thickness, surface area) related to the slope and the intercept of the fit. A relationship with the slope of the fit would suggest that neural population selectivity got more dependent on visual cortical anatomy towards the peripheral visual field, whereas a relationship with the intercept of the fit would indicate an increased dependence towards the central visual field.

To explore the influence of V1 surface area on the eccentricity-dependent variability in V1 neural population selectivity, I plotted neural population selectivity at individual V1 locations (vertices) against the visual field eccentrics these locations responded to and V1 surface area of the participants, across the group of twenty participants and the retinotopy coverage of the visual field (0.25 - 7.2 degree eccentricity). The data were binned into a data grid where individual data point represented neural population selectivity averaged over V1 locations (vertices) that were from the same participant and responded to similar eccentricities (Figure 7.2A). This three-dimensional data grid allowed me to separately address the influence that the visual field eccentricity and V1 surface area exerted on V1 neural population selectivity. Along the axis of V1 surface area, I fitted individual plots of neural population selectivity - visual field eccentricity with linear regression functions, where each plot represented the data from a single participant (Figure 7.2B). I found that the slope ($r = 0.549$, 95% CI = [0.141, 0.797], $p < 0.05$, N = 20 participants) and the intercept ($r = 0.614$, 95% CI = [0.236, 0.830], $p < 0.01$, N = 20 participants) of the fit both correlated positively with the surface area of V1, while the goodness of the fit did not exhibit such correlation ($r = -0.272$, 95% CI = [-0.63, 0.193], $p = 0.245$, N = 20 participants). Therefore, neural population selectivity in V1 with a larger surface area had not only a higher value near fovea but also a faster increase along the visual field eccentricity. These observations suggested that the correlation between V1 neural population selectivity and V1 surface area was not specific to certain visual field eccentricity but

was instead generalisable across the visual field. Indeed, when I applied correlation analysis along the axis of visual field eccentricity directly on individual plots of V1 neural population selectivity - V1 surface area, I observed a positive correlation between V1 neural population selectivity and V1 surface area, for each range of visual field eccentricity (Figure 7.2C).

To explore the influence of V1 thickness on the eccentricity-dependent variability in V1 neural population selectivity, I applied a similar analysis where I plotted neural population selectivity at individual V1 locations (vertices) against the visual field eccentrics these locations responded to and V1 thickness at these locations, across the group of twenty participants and the retinotopy coverage of the visual field (0.25 - 7.2 degree eccentricity). The data were binned into a data grid where individual data point represented neural population selectivity averaged over V1 locations (vertices) that were similar in thickness and responded to similar eccentricities (Figure 7.2A). Through this three-dimensional data grid, I separately addressed the influence that the visual field eccentricity and V1 thickness exerted on V1 neural population selectivity. Along the axis of V1 thickness, I fitted individual plots of neural population selectivity - visual field eccentricity with linear regression functions, where each plot represented the data from a single thickness range of 0.1 mm. I found that the slope (r = -0.528, 95% CI = [-0.78, -0.11], $p < 0.05$, N = 20 participants) and the intercept (r = -0.935, 95% CI = [-0.97, -0.84], $p < 0.0001$, N = 20 participants) of the fit both correlated negatively with the thickness of V1, while the goodness of the fit did not co-vary with V1 thickness (r = 0.147, 95% CI = [-0.32, 0.553], p = 0.534, N = 20 participants). The influence of V1 thickness on both the slope and the intercept of the fit suggested that the dependence of V1 neural population selectivity on V1 thickness was not specific to certain visual field eccentricity but was instead generalisable across the visual field. To verify this, I applied correlation analysis along the axis of visual field eccentricity directly on individual plots of V1 neural population selectivity - V1 thickness. I observed a negative correlation between V1 neural population selectivity and V1 thickness, for each range of visual field eccentricity (Figure 7.2C).

These correlations between V1 neural population selectivity and V1 anatomy suggested that the observations at a fixed visual field eccentricity (4.7 degree), where the thickness and the surface area of V1 exerted opposite influence on V1 neural population selectivity, were generalisable across the visual field. To explore whether such generalization was observable in V2, I plotted neural population selectivity at individual V2 locations (vertices) against the visual field eccentrics these locations responded to and V2 anatomy (surface area, thickness) at these locations. The data were binned into data grids characterising the increase in V2 neural

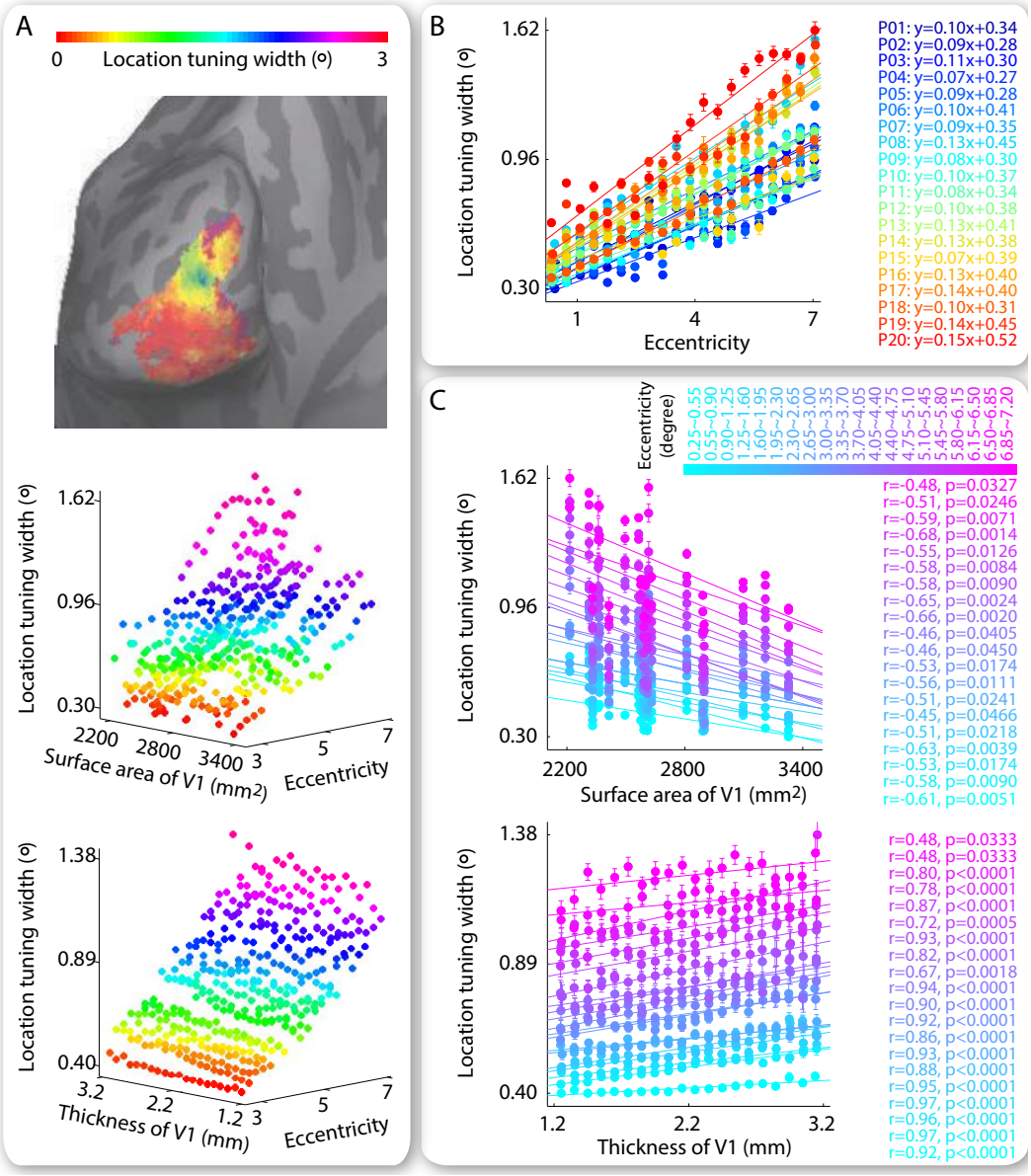

Figure 7.2: Visual cortical anatomy and neural population selectivity. The width of neural population tuning for visual field location, measured at individual V1 locations, was plotted against visual field eccentricities these cortical locations responded to and V1 anatomy at these cortical locations (A). Along the axis of V1 surface area, each plot of location tuning width - visual field eccentricity represented the data from a single participant and illustrated the increase in location tuning width with visual field eccentricity (B). Along the axis of visual field eccentricity, each plot of location tuning width - V1 anatomy represented the data from a single eccentricity range and illustrated the dependence of location tuning width on V1 surface area or V1 thickness (C). Data points are color coded according to the location tuning width (A), the participant (B), or the visual field eccentricity (C). Equations reflect linear fit to the plot of location tuning width - visual field eccentricity (B). Statistical values reflected Spearman's rank correlation with FWE correction for multiple comparisons (C).

population selectivity along the visual field eccentricity, as well as the relationships between V2 neural population selectivity and V2 anatomy within individual ranges of visual field eccentricity. Mirroring the observations in V1, V2 surface area correlated positively with V2 neural population selectivity, and specifically, with its value near fovea (r = 0.729, 95% CI = [0.423, 0.885], $p < 0.001$, N = 20 participants) as well as its slope of increase along the visual field eccentricity (r = 0.705, 95% CI = [0.382, 0.874], $p < 0.001$, N = 20 participants). Conversely, V2 thickness exhibited a negative correlation with V2 neural population selectivity, for each range of visual field eccentricity.

7.4 Discussion

In summary, my study revealed a substantial degree of intra- and inter-individual variability in neural population selectivity that was shaped jointly by visual cortical thickness and visual cortical surface area. I found that neural population selectivity for a visual field location was dependent on the anatomy of corresponding visual cortical location, where the exact pattern of dependence opposed between visual cortical thickness and visual cortical surface area. Specifically, higher neural population selectivity was observed at thinner parts of early visual cortices or in early visual cortices with a larger surface area, regardless of the influence of visual field eccentricity. As such, a larger visual cortical volume, if it came from a larger visual cortical thickness, was associated with a lower neural population selectivity, and if it came from a larger visual cortical surface area, was associated with a higher neural population selectivity.

A lot of recent progress has been made in identifying the relationships between cortical anatomy (surface area, thickness, volume) and behavioral performance. By contrast, the relationships between cortical anatomy and neural response properties remain largely unclear. Such lack of understanding may result from the difficulty in non-invasive measure of neural response properties, especially by comparison to the easiness in measuring behavioral performance. Indeed, due to the discrepancy between the coarse resolution of non-invasive neuroimaging signals and the fine resolution of neural responses, the neuroimaging signals usually detect the aggregate responses from neurons with very different or even opposite response properties, which render the neural population responses qualitatively different from the single neural responses. An exception to this limitation is the neural responses to visual field location in early visual cortices, where cortically adjacent neurons respond selectively to spatially adjacent visual field locations [71]. The orderly cortical representation of visual

field location improves the response similarity between different neurons within a voxel, and this intra-voxel response similarity is further improvable by increasing the resolution of neuroimaging signals. Such combination of orderly cortical representation for visual field location and high resolution in neuroimaging signals therefore allows the estimation of single neural selectivity from the measure of neural population selectivity for visual field location.

To measure neural population selectivity for visual field location, the method of population-receptive-field mapping was developed [122]. This method relies on the presentation of a visual stimulation at a set of different visual field locations distributed evenly in the visual field. By fitting the BOLD responses to such visual stimulation with a two-dimensional Gaussian function, the method estimates the visual field range to which each voxel responds, as a reflection of neural population selectivity for visual field location. This method is conceptually similar to the method of spike-triggered average (reverse correlation) used in extracellular recording that measures single neural selectivity for visual field location (spatial receptive field). Both methods depend on the assumption of a linear spatial summation where the response to a stimulus equals the sum of the responses to the stimulus components. This linearity of spatial summation is observed in early visual cortices, which supports the method of population-receptive-field mapping for measuring neural population selectivity [180]. Indeed, my experiment observations demonstrate that the method offers a reliable measure of neural population selectivity unbiased by fMRI signal properties including the signal-to-noise ratio, the hemodynamic response function, and the spatial resolution.

Such a reliable measure of neural population selectivity allowed me to explore the relationships between visual cortical anatomy and neural response properties. My experiment observations in this chapter, that an opposition existed between visual cortical surface area and visual cortical thickness in their influence on neural population selectivity, mirrored the empirically observed relationships between visual cortical anatomy and visual discrimination threshold in Chapter Five, where a larger visual cortical surface area was found to associate with a finer visual discrimination and a larger visual cortical thickness was found to associate with a poorer visual discrimination. Together these findings suggest that a larger cortical volume is not always advantageous. Instead, a perceptually advantageous visual cortical design seems to involve a thinned visual cortex with an enlarged surface area. This is consistent with the developmental trend that the sensory experience drives the expansion of sensory cortical map but the thinning of sensory cortex [139, 181]. Moreover, the association between a thinner visual cortex and a finer visual function is consistent with a similar trend in the retina. In the

retina, the part with the highest visual acuity, the fovea, is also the thinnest. The fovea has only one photoreceptor layer that minimizes the absorption of light along the retinal pathway [182]. As such, a finer visual function may in general be achieved through the optimization of tissue distribution rather than the simple increase in tissue volume.

The similarity between neural population selectivity and visual discrimination threshold in their dependence on visual cortical anatomy was consistent with the predictions from the visual cortical model in Chapter Six. Specifically, the visual cortical model, based on the scaling of intracortical processing with visual cortical anatomy, suggested that visual cortical anatomy influenced visual discrimination threshold through the feature selectivity of visual cortical neurons that was in turn shaped by the intracortical processing, and as a result, neural population selectivity and visual discrimination threshold would exhibit similar dependence on visual cortical anatomy. The consistency between the model predictions and the experiment observations consolidated the model, and thereby provided an implicit support for the involvement of intracortical processing in linking visual cortical anatomy to visual perception. For an explicit test, in the next chapter, I measured the intracortical connectivity in early visual cortices using the method of Dynamic Causal Modeling [80]. I then explored whether the weakening of intracortical connectivity indeed shifted the scope of visual perception from global context-oriented to local detail-oriented.

Chapter 8

Role of Visual Cortical Connectivity

8.1 Introduction

Perception of a visual stimulus is rarely a true reflection of its physical properties but is often modulated by the spatial contexts surrounding the stimulus. Such contextual modulation of perception is widespread in everyday vision and can be easily demonstrated by contextual illusions. For example, in orientation contextual illusion (tilt illusion), the perceived orientation of a central stimulus is shifted away from its physical orientation when surrounded by a tilted context [102]. Similar illusions exist for perception of other elementary visual features such as contrast and luminance. The magnitude of these contextual illusions reflects the degree to which perception of elementary visual features is global, context-oriented. However, despite representing a key aspect to visual perception, little is known about the neural mechanisms underlying such contextual modulation of visual perception.

In Chapter Four, I found that the magnitude of contextual illusion for elementary visual features exhibited a ten-fold inter-individual variability that correlated with the surface area of early visual cortices. Importantly, among different elementary visual features (orientation, contrast, luminance) and different early visual cortices (V1, V2) studied, this correlation between contextual illusion magnitude and visual cortical surface area was observed specifically between orientation and V1. Such specificity suggested that one approach towards understanding the neural mechanisms of contextual illusions was to ask what was unique about the cortical processing of orientation in V1 that was not observed for the cortical processing of orientation in V2 or the cortical processing of contrast or luminance. Compared to the cortical processing of contrast or luminance, the cortical processing of orientation was unique in its orderly representation where neurons selective for more similar orientation were more strongly connected [37]. Moreover, while this orderly representation of orientation was continuous over the cortical surface of V1, it was interleaved with the representation of color over the cortical surface

of V2. Consequently, the change in V1 surface area would affect the orderly representation of orientation in V1, which would in turn scale the intracortical connectivity between V1 neurons selective for similar orientation. By contrast, this systematic relationship between the surface area of early visual cortices and the intracortical processing of elementary visual features would not apply to V2, or to contrast or luminance. My experiment observations therefore hinted towards an involvement of intracortical connections in contextual modulation of visual perception, where the change in contextual illusion magnitude with visual cortical surface area was underlied by the scaling of intracortical connectivity.

In fact, long before my studies, it was hypothesized that visual contexts modulated perception through visual cortical connections, such as through intracortical connections in early visual cortices [102, 105, 183]. These hypotheses were inspired by empirical studies in animal models showing the involvement of visual cortical connections in contextual modulation of visual neural responses. Consistent with these hypotheses, I showed, in Chapter Six using model simulation, that the scaling of intracortical connectivity with visual cortical surface area was able to affect contextual modulation of visual neural responses in a fashion that mirrored the empirically observed impacts of visual cortical surface area on contextual modulation of visual perception. However, although contextual modulation of visual perception resembled contextual modulation of visual neural responses, they might not share similar mechanisms. This was particularly the case given that visual perception and neural responses did not exhibit exactly the same dependence on visual contexts [102]. Since it was difficult to acquire a non-invasive assessment of cortical connections in human participants and it was equally difficult to acquire a direct measure of visual perception in animal models, there existed no empirical study addressing directly the role of visual cortical connections in contextual modulation of visual perception, despite the rich theoretical literatures.

Nevertheless, with the recent advances in Dynamic Causal Modeling (DCM), it is now possible to acquire a non-invasive assessment of cortical effective connectivity in human participants from fMRI BOLD signals. Specifically, by taking into consideration the biophysical basis of fMRI BOLD signals and the temporal dynamics of neural interactions, DCM estimates the effective strength of synaptic connections from one neural population to another (effective connectivity) [82]. In contrast to the functional connectivity that merely describes the statistical dependency in the neuroimaging signals without inferring the underlying neural causes, the effective connectivity reflects the coupling between the hidden neural states that give rise to the neuroimaging signals. As such, DCM allows the separation of signals reflecting differ-

ent cortical connections (e.g., intracortical, feedforward, feedback), which has been validated by concurrent fMRI-intracranial recordings demonstrating the consistency between the DCM measure of cortical connectivity and the intracranial measure of neural coupling [84].

Applying DCM, I measured the intracortical, feedforward, feedback connectivity between the foveal and peripheral visual cortical regions that responded to the central stimulus and its surrounding context, respectively. I then explored the role of these visual cortical connections in contextual modulation of visual neural responses, by studying their change from non-contextual stimulation (where the central stimulus or its surrounding context was presented in isolation) to contextual stimulation (where the central stimulus and its surrounding context were presented simultaneously). I also explored the role of these visual cortical connections in contextual modulation of visual perception, by studying their co-variance with the magnitude of contextual illusion. A classical approach to vary the contextual illusion magnitude was by changing the feature (e.g., orientation) difference between the central stimulus and the surrounding context. This approach, however, had the pitfall of confounding the perceptual variability in contextual illusion magnitude with the physical variability in contextual illusion stimulus, which rendered it difficult to disentangle whether any correlation between visual cortical connectivity and contextual illusion magnitude reflected the perceptual or the physical effect. To overcome this, I took a novel approach utilizing the perceptual variability across individuals in contextual illusion magnitude, and studied how such perceptual variability was shaped by inter-individual variability in visual cortical connectivity.

Taken together, in this chapter, I explored the role of visual cortical connections in visual contextual modulation with two specific aims. First, using DCM, I measured the intracortical, feedforward, feedback connectivity in early visual cortices, and studied how these visual cortical connections changed within individuals from non-contextual stimulation to contextual stimulation. Then, I studied how these visual cortical connections varied across individuals, and addressed the contribution of their inter-individual variability to inter-individual variability in contextual illusion magnitude. To this end, I focused on contextual modulation in orientation domain, because neurons in early visual cortices are connected according to their selectivity for orientation [38, 43] and their connectivity may in turn shape their modulation by orientation contexts. I acquired the DCM measure of visual cortical connectivity under different experiment task (passive viewing, active judging), which addressed whether the DCM measure was task-invariant. I also acquired the psychophysics measure of contextual illusion magnitude under different experiment configurations of stimulus size and stimulus contrast, which

addressed whether inter-individual variability in contextual illusion magnitude represented a stimulus-independent trait.

8.2 Methods

8.2.1 Participants and Apparatus

A group of twenty healthy participants (aged 19 to 34, ten females, ten males), with normal or corrected-to-normal vision and no neurological history, gave written informed consent to take part in this study approved by the UCL ethics committee. All participants took part in the neuroimaging experiments where I measured visual cortical connectivity using the experiment task of passive viewing, and the psychophysics experiments where I tested the influence of stimulus size on the measure of tilt illusion magnitude. Ten of the participants further took part in the neuroimaging experiments where I measured visual cortical connectivity using the experiment task of active judging, and the psychophysics experiments where I tested the influence of stimulus contrast on the measure of tilt illusion magnitude.

The psychophysics experiments took place in a dark room where the computer monitor provided the only significant source of light. The visual stimuli were presented on a 22" computer monitor (size = 41 x 30.6 cm, resolution = 2048 x 1536 pixels) and viewed through a chin and forehead rest (viewing distance = 67 cm). The neuroimaging experiments took place in a Siemens Trio 3T MRI scanner with a 32-channel head-coil. The visual stimuli were projected onto a screen (size = 28.6 x 21.5 cm) in the back of the scanner and viewed through a mirror on the head-coil (viewing distance = 85 cm). The stimuli covered a portion of the visual field extending from 0.25 to 7.2 degree eccentricity. Structural MRI data were collected using a T1-weighted sequence at 1 mm resolution (TR = 7.92 ms, TE = 2.48 ms, matrix = 256 x 240). Functional MRI data were collected using a 3D EPI sequence at 1.5 mm resolution (volume TR = 3.2 s, TE = 32.86 ms, matrix = 128 x 128). Functional MRI data were preprocessed in SPM8 through bias correction, realignment, unwarping, coregistration, and physiological noise correction.

8.2.2 Psychophysics experiments

To assess inter-individual variability in tilt illusion magnitude, the orientation difference between the central stimulus and the surrounding context was optimized to provide the maximum tilt illusion. Specifically, the central stimulus and the surrounding context were sinusoidal gratings (spatial frequency = 1.5 cycles per degree of visual angle) that had orientation of 45

and 60 degree, respectively. In the main experiments, the central stimulus had an eccentricity coverage from 0.25 to 1.75 degree of visual angle and a contrast of 70%, whereas the surrounding context had an eccentricity coverage from 2.4 to 7.2 degree of visual angle and a contrast of 70%. To test whether inter-individual variability in tilt illusion magnitude was dependent on the stimulus size, I conducted control experiments where the eccentricity coverage of the central stimulus and the surrounding context were from 0 to 0.75 degree of visual angle, and from 0.75 to 3 degree of visual angle, respectively. To test whether inter-individual variability in tilt illusion magnitude was accounted for by inter-individual variability in effective contrast of visual stimulation [184, 185], I conducted further control experiments where the contrast of the central stimulus and the surrounding context were individualized for each participant according to their contrast detection threshold measured in independent experiments.

These experiments measuring the tilt illusion magnitude differed only in the visual stimuli and shared the same experiment procedures, where the standard method of constant stimuli was used. In a single experiment trial, two central stimuli, one with and one without a surrounding context, were presented in succession on the computer monitor. The interval (first or second) where the surrounding context appeared was randomized but counter-balanced across trials. The duration of each stimulus was 300 ms and the inter-stimulus-interval was 500 ms. While maintaining central fixation throughout the experiment, participants made an unspeeded forced-choice regarding whether the central stimulus in the second interval, compared with the one in the first interval, was rotated clockwise or anti-clockwise. Prior to the experiment, each participant performed four trials in which they manually adjusted the orientation of the central stimulus presented in isolation till it matched the perceived orientation of the central stimulus presented in the surrounding context. In the subsequent experiment, the orientation of the central stimulus presented in the surrounding context was kept constant, while that of the central stimulus presented in isolation was varied around this point of perceptual equality for seven different orientation values. In a single experiment, a total of 112 trials (16 trials per orientation value) were taken to produce a psychometric curve. The tilt illusion magnitude was calculated as the orientation difference between the two central stimuli at the 50% threshold point of the psychometric curve where they appeared perceptually equal.

Independent of these experiments measuring the tilt illusion magnitude, I measured the contrast detection threshold, separately for the central stimulus and the surrounding context, using the standard 2-up-1-down staircase procedure. In a single experiment trial, a low-contrast sinusoidal grating (spatial frequency = 1.5 cycles per degree of visual angle, eccentricity cov-

erage = 0.25 to 1.75 degree of visual angle for the central stimulus, 2.4 to 7.2 degree of visual angle for the surrounding context), oriented at 45 degree either towards left or towards right of the vertical, was presented for 300ms. The orientation of the stimulus (left or right) was randomized across trials. While maintaining central fixation throughout the experiment, participants made an unspeeded forced-choice regarding whether the stimulus was left or right oriented. The contrast of the stimulus was varied in a 2-up-1-down staircase fashion that assessed the contrast detection threshold at which the performance converged to 70.7% correct [109]. Specifically, two consecutive correct answers led to a one-step decrease in the stimulus contrast in the next trial, whereas one incorrect answer lead to a one-step increase in the stimulus contrast. The experiment stopped after eighteen reversals, and the contrast detection threshold was calculated as the stimulus contrast averaged over the last ten reversals.

8.2.3 Neuroimaging experiments

To measure visual cortical connectivity between the foveal and peripheral regions-of-interest that responded respectively to the central stimulus and the surrounding context, the visual stimuli were presented in a block design where participants viewed a central stimulus alone, a surrounding context alone, a central stimulus together with a surrounding context, or a blank screen, in different experiment blocks. Two types of surrounding context were used, one tilted (orientation = 60 degree) from the central stimulus (orientation = 45 degree) and induced the tilt illusion, as well as one iso-oriented (orientation = 45 degree) to the central stimulus (orientation = 45 degree) and induced no tilt illusion. For both types, the surrounding context had eccentricity coverage from 2.4 to 7.2 degree of visual angle, whereas the central stimulus had eccentricity coverage from 0.25 to 1.75 degree of visual angle. The eccentricity gap between the central stimulus and the surrounding context contributed to the reliable separation of the foveal and peripheral regions-of-interest, whereas the eccentricity gap within the central stimulus helped to avoid the activation of the foveal confluence where the boundaries of early visual cortices were difficult to delineate.

Using the block design presentation of visual stimuli, the fMRI BOLD time series were collected under two different experiment tasks that addressed the influence of experiment task on the measure of visual cortical connectivity. The first experiment task was designed to minimize inter-individual variability in attention allocation, and involved passive viewing of the stimulus orientation. Specifically, participants passively viewed the visual stimuli, while maintaining eye fixation at a central cross through the detection of its color change. The second experiment task was designed to match the psychophysics experiment task, and involved active

judging of the stimulus orientation. Specifically, participants actively judged the orientation of the central stimulus, which underwent a clockwise or anti-clockwise change at random interval for 400 ms, while maintaining eye fixation at a central cross under the monitor of an eye tracker. The degree of orientation change was individualized for each participant according to their orientation discrimination threshold measured in independent experiments using the standard 2-up-1-down staircase procedure. This procedure of individualization helped to ensure that the detection of orientation change was equally difficult for different participants. However, as a pitfall, the fMRI BOLD time series contained not only a common block component, but also an individualized event-related component that might confound the measure of inter-individual variability. Therefore, this individualized event-related component was filtered out from the fMRI BOLD time series through a low-pass Butterworth filter.

From the collected fMRI BOLD time series, the foveal and peripheral regions-of-interest were delineated in early visual cortices using two different approaches that addressed the influence of regions-of-interest delineation on the measure of visual cortical connectivity. In the first approach, fMRI BOLD signals evoked by the central stimulus were contrasted against fMRI BOLD signals evoked by the surrounding context at a threshold of $p<0.001$ (uncorrected), to delineate the foveal and peripheral regions-of-interest. In the second approach, the delineated foveal and peripheral regions-of-interest were further refined according to the visual field response range of individual fMRI voxels measured in independent experiments using the method of population-receptive-field mapping [122]. Specifically, the fMRI voxels whose visual field response range overlapped with the surrounding context were excluded from the foveal region-of-interest, whereas the fMRI voxels whose visual field response range overlapped with the central stimulus were excluded from the peripheral region-of-interest. This procedure of refinement helped to avoid the spillover between the foveal and peripheral regions-of-interest. In both approaches, the delineated foveal and peripheral regions-of-interest were then projected with the boundaries of early visual cortices (V1, V2, V3), measured in independent experiments using the standard phase-encoded retinotopic mapping [71], to define foveal V1, peripheral V1, foveal V2, peripheral V2, foveal V3, and peripheral V3 for uses in the DCM analysis.

Based on the regions-of-interest delineation, DCM was applied to estimate the effective connectivity between any two of the six regions-of-interest (foveal V1, peripheral V1, foveal V2, peripheral V2, foveal V3, peripheral V3), and to study how the effective connectivity changed from non-contextual stimulation to contextual stimulation. To this end, anatomi-

cally plausible DCM models comprising the six inter-connected regions-of-interest were constructed, where each DCM model tested a hypothesis of the change in effective connectivity from non-contextual stimulation to contextual stimulation. These different DCM models could be grouped into three different families that hypothesized a change in intracortical connectivity within each early visual cortex (the first family), or a change in intercortical connectivity between different early visual cortices (the second family), or a change in both (the third family). Specifically, the first DCM family contained three different DCM models hypothesizing, respectively, a change in intracortical connectivity from peripheral to foveal regions-of-interest, a change in intracortical connectivity from foveal to peripheral regions-of-interest, and a change in both (Figure 8.1A). The second DCM family contained fifteen different DCM models hypothesizing a change in feedback connectivity from peripheral to foveal regions-of-interest, a change in feedback connectivity from foveal to peripheral regions-of-interest, a change in feedforward connectivity from peripheral to foveal regions-of-interest, a change in feedforward connectivity from foveal to peripheral regions-of-interest, or any of these combined (Figure 8.1B). The third DCM family contained eight different DCM models (Figure 8.1C) hypothesizing a combination of the change in intracortical connectivity (as in the first family) and the change in intercortical connectivity (as in the second family).

After the construction of DCM models, Bayesian model selection was applied to identify the DCM family with the highest posterior probability (family-level inference), and in that family, the DCM model with the highest posterior probability (model-level inference). Based on the winning DCM model in the winning DCM family, the effective connectivity was measured between different regions-of-interest (foveal V1, peripheral V1, foveal V2, peripheral V2, foveal V3, peripheral V3) for different visual stimulation (non-contextual, tilted contextual, iso-oriented contextual). From this DCM measure of visual cortical connectivity, I explored intra-individual change in visual cortical connectivity from non-contextual stimulation to contextual stimulation, as well as inter-individual relationship between visual cortical connectivity and contextual illusion magnitude.

8.3 Results

8.3.1 Visual cortical connectivity under contextual stimulation

To explore the influence of visual stimulation (non-contextual versus contextual) on visual cortical connectivity, I constructed different DCM models where each tested a hypothesis about the change in visual cortical connectivity from non-contextual stimulation (where the cen-

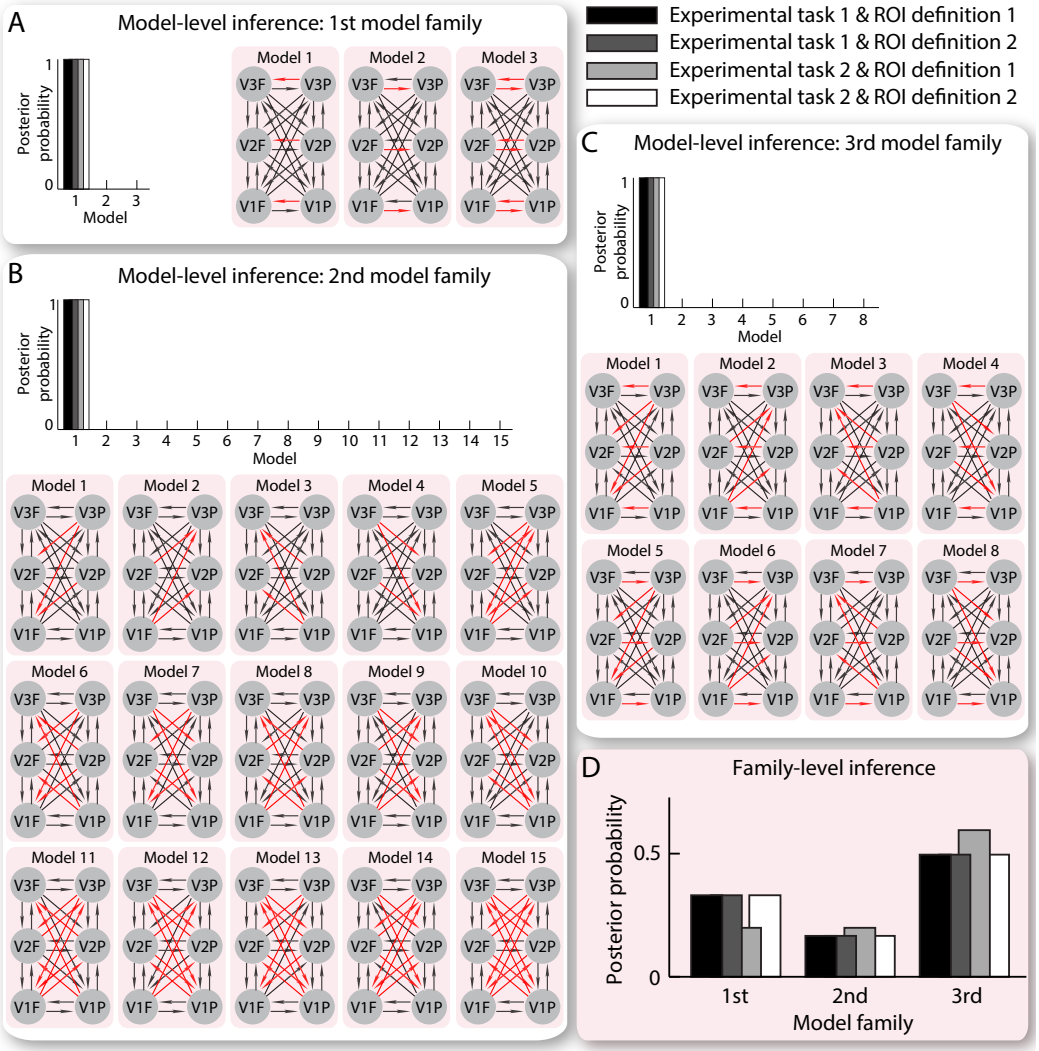

Figure 8.1: DCM measure of visual cortical connectivity. Dynamic Causal Modeling (DCM) analysis was applied to estimate the effective connectivity between foveal and peripheral regions of early visual cortices that responded to a central stimulus and its surrounding context, respectively. Three families of DCM models were constructed hypothesizing changes in intracortical connectivity within each early visual cortex (A), or changes in intercortical connectivity between different early visual cortices (B), or changes in both (C), when the central stimulus and its surrounding context were presented together as compared to in isolation. Within each model family, different DCM models were constructed incorporating different directionality of hypothesized changes in effective connectivity, as illustrated by the red arrows in the schematic depictions of model structures. Bayesian model comparison was applied to select the model with the highest posterior probability within each model family (model-level inference), and the model family with the highest posterior probability (family-level inference). DCM analysis for each of the four combinations of ROI definition and experimental task was carried out independently and returned highly consistent results (D).

tral stimulus and its surrounding context was presented in isolation) to contextual stimulation (where the central stimulus and its surrounding context was presented together). Specifically, three families of DCM models were constructed, hypothesizing a sole change in intracortical connectivity within each early visual cortex (the first DCM family), or a sole change in intercortical connectivity between different early visual cortices (the second DCM family), or a change in both intracortical and intercortical connectivity (the third DCM family).

Within each DCM family, Bayesian model selection was applied to identify the DCM model with the highest posterior probability (model-level inference). The analysis revealed that, in the first DCM family, the DCM model hypothesizing a change in intracortical connectivity from peripheral to foveal regions-of-interest had a high posterior probability (close to one), whereas the DCM models hypothesizing a change in intracortical connectivity from foveal to peripheral regions-of-interest had a low posterior probability (close to zero). In the second DCM family, the DCM model hypothesizing a change in feedback connectivity from peripheral to foveal regions-of-interest had a high posterior probability (close to one), whereas the DCM models hypothesizing a change in feedback connectivity from foveal to peripheral regions-of-interest, or a change in feedforward connectivity, or a change in any combination of feedback and feedforward connectivity, all had a low posterior probability (close to zero). In the third DCM family, the DCM model hypothesizing a change in intracortical and feedback connectivity from peripheral to foveal regions-of-interest had a high posterior probability (close to one), whereas the DCM models hypothesizing a change in other combination of intracortical and intercortical connectivity all had a low posterior probability (close to zero).

Across different DCM families, Bayesian model selection was applied to identify the DCM family with the highest posterior probability (family-level inference). The analysis revealed that, the third DCM family, which hypothesized a change in both intracortical and intercortical connectivity, had a higher posterior probability than the other two DCM families, which hypothesized either a sole change in intracortical connectivity or a sole change in intercortical connectivity. Together the model-level inference and the family-level inference consistently suggested that, contextual stimulation affected both intracortical and feedback connectivity from peripheral to foveal visual cortical regions, while it had no influence on other intracortical or intercortical connectivity between the foveal and peripheral visual cortical regions. These results provided a qualitative estimation of the change in visual cortical connectivity from non-contextual stimulation to contextual stimulation.

To provide a quantitative estimation of the change in visual cortical connectivity from

non-contextual stimulation to contextual stimulation, I acquired the measure of visual cortical connectivity, from the wining DCM model in the winning DCM family, separately for the condition of non-contextual stimulation where either an isolated central stimulus, or an isolated surrounding context, or a blank screen, was presented, and for the condition of contextual stimulation where the central stimulus was presented together with the surrounding context. The analysis revealed that, the intracortical and feedback connectivity from peripheral to foveal visual cortical regions was very weak under non-contextual stimulation (Figure 8.2, 95% confidence interval overlapped with zero), but underwent a substantial increase from non-contextual stimulation to contextual stimulation (Figure 8.2). Moreover, this increase was observed regardless of whether the surrounding context had the same orientation (iso-oriented) or a different orientation (tiled) to the central stimulus, which suggested an involvement of generic (instead of orientation-dependent) intracortical and feedback connections in contextual modulation of visual neural responses.

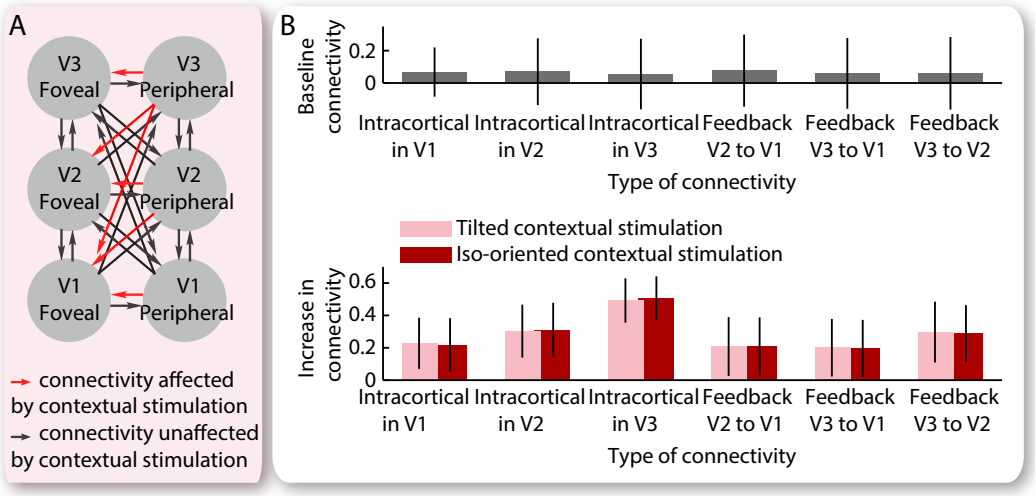

Figure 8.2: Visual cortical connectivity under contextual stimulation. Bayesian model comparison revealed that contextual stimulation changed intracortical and feedback connectivity from peripheral to foveal regions of early visual cortices (A). At the baseline condition where a blank screen or an isolated central stimulus or an isolated surrounding context was presented, the intracortical and feedback connectivity from peripheral to foveal regions of early visual cortices was not significantly different from zero. Under contextual stimulation, a significant increase was observed in intracortical and feedback connectivity from peripheral to foveal regions of early visual cortices, regardless of whether the surrounding context and the central stimulus had different or identical orientation. Bar chart reflects the mean and 95% confidence interval of the maximum a posteriori (MAP) estimates across participants (N = 20).

Reported above were the results from the fMRI data where the experiment task involved passive viewing of the stimulus orientation (the first experiment task), and the regions-of-interest were delineated according to general linear model contrast alone (the first regions-of-interest delineation approach). To address the influence of experiment task and regions-of-interest delineation on the DCM measure of visual cortical connectivity, I applied the same DCM analysis to the fMRI data where the experiment task involved active judging of the stimulus orientation (the second experiment task), or the regions-of-interest were stringently confined according to population-receptive-field map (the second regions-of-interest delineation approach). The results from these additional analyses (Figure 8.1) were highly consistent with the original ones, suggesting that the DCM measure of visual cortical connectivity was reliable, and the observed change in visual cortical connectivity from non-contextual stimulation to contextual stimulation was robust.

8.3.2 Visual cortical connectivity and perceptual variability

The change in intracortical and feedback connectivity from non-contextual stimulation to contextual stimulation suggested an involvement of these visual cortical connections in contextual modulation of visual neural responses. To explore the role of these visual cortical connections in contextual modulation of visual perception, I studied their co-variance with the magnitude of contextual illusion. Specifically, I took an inter-individual variability approach examining whether such a co-variance between brain signals and perception existed across participants, as this approach allowed me to vary the contextual illusion magnitude without changing the contextual illusion stimulus.

Using psychophysics methods, I measured the magnitude of orientation contextual illusion (tilt illusion). All twenty participants were shown the same tilt illusion stimulus, yet the tilt illusion magnitude varied across participants over several folds. As the tilt illusion magnitude is dependent on the stimulus size and the stimulus contrast [121], I addressed whether inter-individual variability in tilt illusion magnitude was also stimulus-specific. I compared the measure of tilt illusion magnitude across different stimulus size (small versus large) and different stimulus contrast (non-individualized versus individualized). I found that, while an increase in the stimulus size led to a weaker tilt illusion ($t(19) = 3.8$, $p < 0.005$, N = 20 participants), the measure of tilt illusion magnitude under large stimulus correlated significantly with that under small stimulus ($r = 0.69$, 95% CI = [0.357, 0.867], $p < 0.001$, N = 20 participants). Moreover, when the stimulus contrast was individualized for each participant according to their contrast detection threshold, I still observed a substantial degree of inter-individual variability

in the measure of tilt illusion magnitude, which correlated with the measure of tilt illusion magnitude under non-individualized stimulus (r = 0.77, 95% CI = [0.497, 0.904], $p < 0.05$, N = 20 participants).

These results that the tilt illusion magnitude varied inter-individually in a stimulus-independent fashion hinted towards an underlying basis in the neurobiological variability across individuals. Indeed, inter-individually, the magnitude of tilt illusion correlated significantly with the value of visual cortical connectivity under contextual stimulation (Figure 8.3, r = 0.62, 95% CI = [0.245, 0.833], $p < 0.005$, N = 20 participants), or the change in visual cortical connectivity from non-contextual stimulation to contextual stimulation (Figure 8.3, r = 0.46, 95% CI = [0.022, 0.749], $p < 0.05$, N = 20 participants). This correlation between visual cortical connectivity and tilt illusion magnitude exhibited circuitry specificity, in that it was specific to the measure of intracortical connectivity from peripheral to foveal V1, as opposed to the measure of other intracortical or intercortical connectivity between the foveal and peripheral visual cortical regions (Figure 8.3). Moreover, this correlation exhibited orientation specificity, in that it was specific to the measure of V1 intracortical connectivity under tilted contextual stimulation, as opposed to the measure of V1 intracortical connectivity under iso-oriented contextual stimulation (Figure 8.3). Such circuitry specificity and orientation specificity hinted towards an involvement of orientation-dependent (instead of generic) intracortical connections in contextual modulation of orientation perception.

In addition to addressing the contribution of visual cortical connections, I further studied whether inter-individual variability in tilt illusion magnitude could be explained by other measures of visual cortical processing, and in particular, by the level of visually evoked BOLD responses in the six regions-of-interest (foveal V1, peripheral V1, foveal V2, peripheral V2, foveal V3, peripheral V3). I found that while the level of BOLD responses evoked by tilted contextual stimulation and the change in BOLD responses from non-contextual stimulation to tilted contextual stimulation both varied substantially across participants, neither exhibited correlation with the magnitude of tilt illusion (Figure 8.3, $r < 0.20$, $p > 0.39$, N = 20 participants). Therefore, whereas the level of visually evoked BOLD responses was traditionally viewed as the neural correlates for the contents of visual perception [186, 187], my experiment observations suggested that visual cortical connectivity might serve more reliably as the neural correlates, at least for inter-individual variability in perception of tilt illusion.

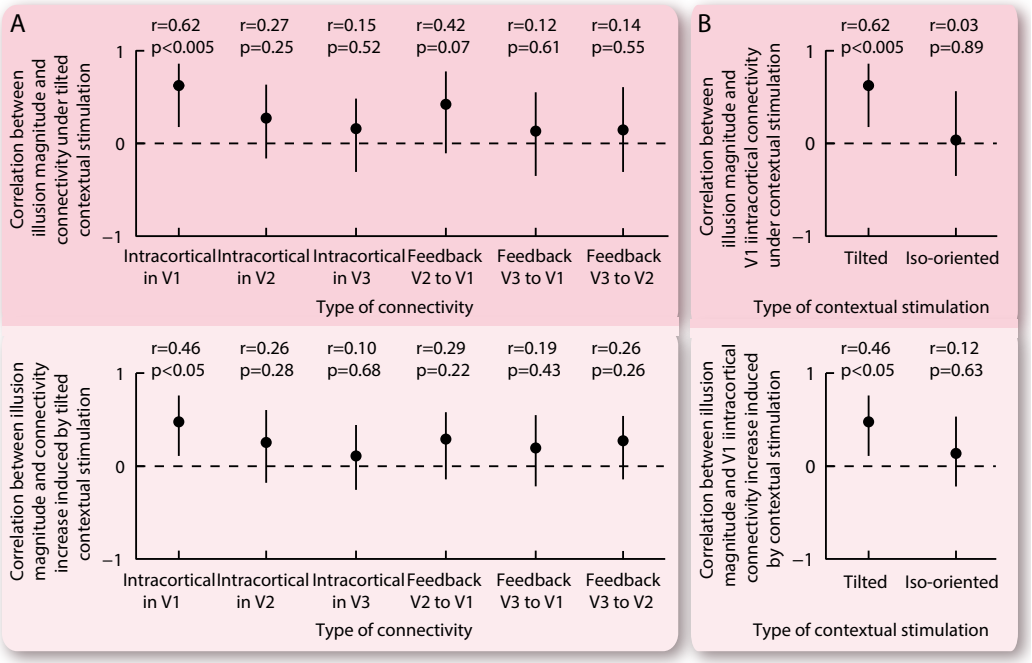

Figure 8.3: Visual cortical connectivity and perceptual variability. (A) Contextual stimulation affected intracortical connectivity within each early visual cortex from its peripheral region to its foveal region, and feedback connectivity between different early visual cortices from the higher peripheral region to the lower foveal region. For each of these affected connectivity, I calculated its inter-individual correlation with the tilt illusion magnitude. The correlation was significant only for intracortical connectivity within V1. (B) Contextual stimulation affected V1 intracortical connectivity regardless of whether the surrounding context had a different or an identical orientation to the central stimulus. For each of these two stimulation conditions, I calculated inter-individual correlation between V1 intracortical connectivity and tilt illusion magnitude. The correlation was significant for the tilted contextual stimulation but not for the iso-oriented contextual stimulation. Statistical values reflect Spearman's rho with FDR correction for multi-comparisons (α = 0.025).

8.4 Discussion

In summary, my study revealed a substantial degree of inter-individual variability in visual cortical connectivity that mediated inter-individual perceptual variability in orientation contextual illusion (tilt illusion). I found that, surrounding a central stimulus with a tilted context not only shifted the perceived orientation of the central stimulus away from its physical orientation (the phenomenon of tilt illusion), but also changed the intracortical and feedback connectivity from peripheral to foveal visual cortical regions that responded respectively to the surrounding context and the central stimulus. Such context-induced shift in perceived orientation and

context-induced change in visual cortical connectivity both varied substantially across individuals. Moreover, an inter-individual correlation with the context-induced shift in perceived orientation (the magnitude of tilt illusion) was observed specifically for the context-induced change in intracortical connectivity from peripheral to foveal V1.

The context-induced change in intracortical and feedback connectivity suggested an involvement of these visual cortical connections in contextual modulation of visual neural responses. Indeed, neurons in early visual cortices have center-surround receptive fields, where the neural responses to orientation at receptive field center (orientation of the central stimulus) are modulated by orientation at receptive field surround (orientation of the surrounding context), and the level of modulation increases with the orientation similarity between the central stimulus and the surrounding context [184, 185]. Initially, it was believed that such contextual modulation of visual neural responses took place through intracortical connection, as intracortical connections preferentially linked neurons selective for similar orientation, which would lead to an increased level of contextual modulation with the increased orientation similarity between the central stimulus and the surrounding context [188, 189, 190]. However, empirical studies in animal models later revealed that the spatiotemporal scales of intracortical connections were smaller than that of neural receptive fields. As such, it was suggested that feedback connections, which covered larger visual field and had faster propagation speed than intracortical connections, also played a key role in contextual modulation of visual neural responses [191, 192]. Consistent with these animal studies, my experiment observations in human participants provided empirical evidence for the involvement of intracortical and feedback connections in contextual modulation of visual neural responses.

In contrast to the context-induced change in visual cortical connectivity, which was observed generally for different intracortical and feedback connections in early visual cortices, the context-induced correlation between visual cortical connectivity and tilt illusion magnitude was observed specifically for intracortical connections in V1. Moreover, this correlation with tilt illusion magnitude was specific to the measure of V1 intracortical connectivity under tilted contextual stimulation, as opposed to the measure of V1 intracortical connectivity under iso-oriented contextual stimulation. Such specificity indicated an involvement of orientation-dependent V1 intracortical connections in contextual modulation of orientation perception. Indeed, it was postulated, long before my study, that contextual modulation of orientation perception took place through visual cortical connections between neurons selective for similar orientation, as such neural interactions would shift the neural population responses (and cor-

responding, the perceived orientation of the central stimulus) in a direction repulsive to the orientation of the surrounding context [193, 194, 195]. This orientation dependency was observed for intracortical connections within V1, in that V1 neurons selective for more similar orientation were also more intracortically connected [38, 43]. By contrast, feedback connections between different early visual cortices (V1, V2, V3) lacked such orientation dependency and linked different neurons regardless of their orientation selectivity [188, 189, 190]. These different properties exhibited by different visual cortical connections put V1 intracortical connections as the most likely candidate for contextual modulation of orientation perception. However, despite the rich theoretical literatures, it had been traditionally difficult to acquire a non-invasive assessment of cortical connections in human participants, and no empirical study had directly addressed the role of visual cortical connections in contextual modulation of visual perception. Nevertheless, with the recent advances in DCM, I was able to measure V1 intracortical connections non-invasively in human participants, and demonstrated their empirical involvement in contextual modulation of orientation perception.

Because of the difficulty in non-invasive measure of cortical connections, traditional studies were limited to viewing the level of visually evoked BOLD responses as the neural correlates for the contents of visual perception [186, 187]. My experiment observations, by contrast, suggested that even when a visual stimulus (e.g., the tilt illusion stimulus) evoked equivalent level of BOLD responses across individuals, the measure of visual cortical connectivity under this visual stimulus might still vary substantially across individuals that predict inter-individual variability in perception of this visual stimulus. As such, compared to the level of visually evoked BOLD responses, visual cortical connectivity might serve more reliably as the neural correlates, at least for inter-individual variability in perception of tilt illusion. Indeed, individual visual cortical neurons only process isolated pieces of visual information (such as the central stimulus alone or the surrounding context alone), whereas visual perception is an integrated process involving visual information processed by distributed visual cortical neurons. Consequently, the contents of visual perception are more likely to be shaped by the level of neural interactions (as indicated in visual cortical connectivity), rather than by the level of overall neural responses (as indicated in the BOLD responses). Since the level of BOLD responses reflects the aggregated contributions of many different visual cortical connections, linking it to the contents of visual perception cannot disentangle the effects of different visual cortical connections and may thus fail to show any significant correlation.

In addition to its advantage over the traditional approach of examining the level of BOLD

responses, DCM also has several advantages over other non-invasive assessment of cortical connections in human participants. For example, whereas the anatomical connectivity analysis using DTI can only reveal the white-matter-mediated intercortical connectivity [196], the effective connectivity analysis using DCM can also reveal the gray-matter-mediated intracortical connectivity. Moreover, the effective connectivity analysis using DCM allows estimation of directionality in cortical connections, which the anatomical connectivity analysis using DTI and the functional connectivity analysis examining statistical dependency both fail to address [197].

Despite these advantages, DCM is limited by the indirect nature and the low resolution of fMRI BOLD signals. Consequently, DCM provides a rough population estimate, rather than an accurate synaptic measure, of cortical connectivity. Nevertheless, utilizing such population estimate, I am able to demonstrate that, the weakening of intracortical connectivity indeed shifts the scope of visual perception from global context-oriented (stronger contextual illusion) to local detail-oriented (weaker contextual illusion), which in turn provides empirical support for my hypothesis (in Chapter Four / Five / Six) that visual cortical surface area influences visual perception through the scaling of intracortical connectivity. Moreover, it is interesting to note that such population estimate of cortical connectivity from DCM already contains a considerable amount of perception-related information. With the advances of two-photon microscopy, the synaptic wiring diagram can now be characterized in awake behaving animals at a subcellular resolution of individual dendritic spines [198, 199]. This opens up future research into the relationship between visual perception and visual cortical connectivity at a subcellular level, albeit in animal models.

Chapter 9

General Discussion

In my thesis, I investigated the neurobiological basis of inter-individual variability in visual feature perception. I began my studies by exploring the extent to which visual feature perception varied across healthy human adults. I found that local feature perception, as assessed from visual discrimination of local feature details [2, 99], and global feature perception, as assessed from visual illusion induced by global feature contexts [100, 101, 102], both exhibited a substantial degree of inter-individual variability. Moreover, whereas the extent of inter-individual perceptual variability was similar across different visual features (orientation, contrast, luminance), local and global perception of orientation exhibited an inter-individual trade-off that was not observed in perception of contrast or luminance. This feature specificity suggested that inter-individual perceptual variability did not arise purely from generic factors such as decision-making ability, but instead had its neurobiological basis in visual cortical architecture.

I then asked whether such inter-individual variability in subjective perception of visual feature might arise from inter-individual variability in objective anatomy of visual cortex. Specifically, I asked how the two fundamental anatomical dimensions, the surface area and the thickness, of early visual cortices, might shape visual feature perception. I found that an increase in the surface area of early visual cortices was associated with a shift in the scope of visual feature perception from global-context-oriented to local-detail-oriented, where individuals with smaller visual cortical surface area experienced stronger visual illusion and individuals with larger visual cortical surface area performed more accurate visual discrimination. Intriguingly, an increase in the thickness of early visual cortices had the opposite influence, where visual discrimination was less accurate at visual field locations corresponding to thicker parts of early visual cortex.

The fact that visual feature perception was influenced in opposite directions by the two

fundamental anatomical dimensions, the surface area and the thickness, of early visual cortices suggested that the perceptual variability might arise not directly from the anatomical variability, but instead through the mediation of neural responses. Indeed, I found that in individuals with larger surface area of early visual cortices, visual cortical neurons exhibited higher selectivity and responded to a smaller, more localized visual field range. By contrast, at thicker parts of early visual cortices, visual cortical neurons exhibited lower selectivity and responded to a larger, more globalized visual field range. This suggested that the variability in visual feature perception was driven by the variability in visual neural selectivity, which was in turn shaped by the two fundamental anatomical dimensions, the surface area and the thickness, of early visual cortices.

Based on these findings, I explored whether the opposite influences exerted by the two anatomical dimensions (surface area, thickness) of early visual cortices might nonetheless be unified under the framework of intracortical scaling, where the visual cortical surface area influenced the inter-columnar connections between cortical columns and the visual cortical thickness influenced the inter-laminar connections between cortical layers. Since an empirical measure of intracortical connections would be difficult in human participants, I tested my hypothesis theoretically, by building a visual cortical model that captured visual neural selectivity and visual feature perception through inter-columnar and inter-laminar connections. The model simulations reproduced the empirical observations. It suggested that, as the visual cortex enlarged in surface area, an increase in the overall number of cortical columns would obstruct communication (connection) among different cortical columns, which would in turn raise the response specificity (selectivity) of individual cortical columns and localise the visual scope; by contrast, as the visual cortex enlarged in thickness, an increase in the laminar communication (connection) delay within individual cortical columns would facilitate the response synchronization among different cortical columns, which would in turn lower the response specificity (selectivity) of individual cortical columns and globalise the visual scope.

The hypothesis that the two anatomical dimensions (surface area, thickness) of early visual cortices influenced visual neural selectivity and visual feature perception via the scaling of intracortical connections was further test empirically, where I applied Dynamic Causal Modeling (DCM) analysis to measure the effective strength of intracortical connections between subregions of early visual cortices, as an approximation to the net strength of inter-columnar and inter-laminar connections. Consistent with the model simulations, I found that a decrease in intracortical connectivity led to a shift in the scope of visual feature perception from global-

context-oriented to local-detail-oriented. Together, my studies revealed that the individuality in visual feature perception arose neurobiologically from inter-individual differences in visual cortical anatomy, where the links between visual cortical anatomy and visual feature perception were gradually built through intracortical circuits and neural feature selectivity.

My findings hint towards a potential mechanism underlying the anatomy-behavior correlations. The correlations between cortical anatomy (surface area, thickness, volume) and behavioral performance (perception, cognition) have received growing research interest [1]. However, most of the reported anatomy-behavior correlations remain phenomenological and offer no inference of the possible underlying mechanisms. Such a lack of mechanistic understanding is likely to result from our limited knowledge in the microscopic architecture of most cortical regions. Moreover, for most cortical regions, the delineation of their boundaries is based on the co-registration of structural MRI image to a common brain atlas. This procedure may fail to capture the substantial degree of inter-individual variability in the functional localization of a cortical region, which adds to the complexity of interpreting these correlations between cortical anatomy and behavioral performance.

In contrast to most other cortical regions, early visual cortices have a relatively well-defined microscopic architecture [37, 38, 97] and are functionally localizable through retinotopic mapping [71]. These properties of early visual cortices provide an opportunity for exploring possible mechanisms underlying the correlations between cortical anatomy and behavioral performance. Utilizing these advantages, my studies reveal that a larger cortical volume is not always advantageous. Instead, a perceptually advantageous visual cortical design involves a thinned visual cortex with an enlarged surface area. This is consistent with the developmental trend that the sensory experience drives the expansion of sensory cortical map but the thinning of sensory cortex [139, 181]. Moreover, the association between a thinner visual cortex and a finer visual function is consistent with a similar trend in the retina. In the retina, the part with the highest visual acuity, the fovea, is also the thinnest. The fovea has only one photoreceptor layer that potentially minimizes light absorption along the retinal pathway [182].

As such, a finer visual function may in general be achieved through the optimization of tissue distribution rather than the increase in tissue volume. This assertion, however, raises concerns for the classical approach taken in studying the anatomical basis of behavioral performance, where one simply assumes that a larger cortical volume (surface area, thickness) is beneficial, and searches for cortical region whose focal volume exhibits positive correlation with the behavioral performance [200, 201, 202]. By demonstrating that the two determinants

of cortical volume, the cortical thickness and the cortical surface area, may exert opposite functional impacts, my findings call for a more careful approach to be taken in future research, where the cortical thickness and the cortical surface area are to be addressed separately, and any negative correlation between cortical volume and behavioral performance is not to be ignored.

In my thesis, I focused on low-level perception of elementary visual features (orientation, visual field location, contrast, luminance). Given the substantial degree of variability in low-level perception of elementary visual features, it is foreseeable that high-level perception of complicated visual images will exhibit an equally large, if not larger, degree of inter-individual variability. Moreover, such a high-level perceptual variability of complicated visual images may be decomposable into low-level perceptual variability of elementary visual features. Indeed, by filtering a complicated visual image into several elementary images and calculating the pixel-by-pixel center-surround differences of each elementary image, one can compute a saliency map that captures eye movements, visual selective attention, and face recognition [92, 94].

When computing the saliency map, the filter bandwidth may correspond with the visual discrimination of local feature details, whereas the center-surround differentiation may correspond with the visual modulation (illusion) by global feature contexts. As such, the variability in local and global perception of elementary visual features may be incorporated to compute saliency maps for complicated visual images. Whether these saliency maps can capture the variability in perception of complicated visual images, and how the high-level perceptual variability of complicated visual images is linked to the low-level perceptual variability of elementary visual features, are interesting topics for future research.

The dichotomy between visual discrimination of local feature details (visual precision) and visual modulation by global feature contexts (visual contextual modulation) raises interesting questions regarding their ecological significance. The Hebbian rule suggests that the brain is optimized to identify contextual information in sensory environment by strengthening connections between presynaptic and postsynaptic neurons [139]. By contrast, the anti-Hebbian rule suggests that the brain is optimized to increase functional specificity (selectivity) and reduce coding redundancy by de-correlating activity between neurons [139]. The two opposing mechanisms are both likely to operate, depending on the pressing challenges in the natural and social environment where the animals reside. Since an orderly representation of elementary visual features is prominent in the early visual cortices of primates [37, 41, 42], a trade-off

between local and global perception of elementary visual features may be the ecological force behind the evolution of early visual cortices.

Indeed, the anatomy of early visual cortices exhibits not only a large degree of intra-species variability but an even larger degree of inter-species variability, where the size of primary visual cortex has increased 250 times from mice to macaque and 2.5 times from macaque to human [45]. However, the human brain is not a scaled version of the mice brain or the macaque brain. By contrast, compared to the allometric predictions from other species, humans have relatively small primary visual cortex [203], but relatively large anterior prefrontal cortex [204]. Mirroring the inter-species scaling of cortical regions, an intra-species trade-off between the size of primary visual cortex and the size of anterior prefrontal cortex was observed in my data [205].

Specifically, I found that individuals with larger primary visual cortex had larger primary auditory cortex but smaller anterior prefrontal cortex, regardless of the inter-individual difference in overall brain size. Moreover, the dorsal and ventral halves of primary visual cortex exhibited focal anti-correlations with the dorsolateral and ventromedial halves of anterior prefrontal cortex. Primary visual cortex and anterior prefrontal cortex are located at the two opposite ends of the cortex. In mice, the two genes Emx2 and Pax6 are expressed in opposing gradients along the anterior-posterior axis. In Emx2 mutant mice, anterior areas are expanded whereas posterior areas are contracted, and the opposite is the case for Pax6 mutant mice [206]. It is possible that the human cortical arealization is also regulated by genes with contrasting expression along the anterior-posterior axis. As such, the anterior-posterior trade-off I observed might result from the individual variations in gene expression levels and might be regulated by environmental interventions during development [207].

This anatomical trade-off between primary visual cortex and anterior prefrontal cortex suggests a reciprocal link, behaviorally or functionally, between two fundamental cognitive domains - basic sensation and high-order cognition. The intriguing similarity in this scaling pattern between intra-species and inter-species suggests its ecological significance, where the relative expansion and contraction of different cortical regions along the path of primate evolution may reflect their importance in generating behavioral complexity. Indeed, the brain evolves through genetic changes from adaptive selection on cognitive ability, and gene expression shows consistent variations within species as well as across species [208]. For example, two important genes for brain size, ASPM and MCPH1, which regulate neural stem cell proliferation and differentiation during brain development, have evolved under strong positive se-

lection in the human evolutionary lineage and are still evolving adaptively in modern humans [209, 210]. The anatomical trade-off between primary visual cortex and anterior prefrontal cortex may reflect the gene expression divergences associated with adaptive evolution. It will be of interest for future research to explore the ecological significance of intra-species and inter-species variability in visual cortical anatomy.

References

[1] Kanai, R. and Rees, G. The structural basis of inter-individual differences in human behaviour and cognition. *Nature Reviews Neuroscience* **12**, 231–242 (2011).

[2] Halpern, S. D., Timothy, J. A., and Purves, D. Interindividual variation in human visual performance. *Journal of Cognitive Neuroscience* **11**, 521–534 (1999).

[3] Bosten, J. M. and Mollon, J. D. Is there a general trait of susceptibility to simultaneous contrast? *Vision Research* **50**, 1656–1664 (2010).

[4] Burbeck, C. A. and Regan, D. Independence of orientation and size in spatial discrimination. *Journal of the Optical Society of America* **73**, 1691–1694 (1983).

[5] Ginsburg, A. P., Evans, D., Cannon, M. W., Owsley, C., and Mulvanny, P. Large-sample norms for contrast sensitivity. *Journal of the Optical Society of America* **61**, 80–84 (1984).

[6] Yates, J. T., Harrison, J. M., Conner, P. S., and Balentine, C. Contrast sensitivity: Characteristics of a large young adult population. *American Journal of Optometry and Physiological Optics* **64**, 519–527 (1987).

[7] Hubel, D. H. Eye, brain and vision. *W H Freeman Publishers* (1995).

[8] Dowling, J. E. The retina: an approachable part of the brain. *Harvard University Press* (1987).

[9] Masland, R. H. The fundamental plan of the retina. *Nature Neuroscience* **4**, 877–886 (2001).

[10] Patton, N., Aslam, T., MacGillivray, T., Deary, I., Dhillon, B., Eikelboom, R., Yogesan, K., Constable, I., and Villegas, G. M. Electron microscopic study of the vertebrate retina. *Journal of General Physiology* **43**, 15–43 (1960).

[11] Bowmaker, J. K. and Dartnall, H. J. A. Visual pigments of rods and cones in a human retina. *Journal of Physiology* **298**, 501–511 (1980).

[12] Thomas, E. and Yiannis, K. Vertebrate photoreceptors. *Progress in Retinal and Eye Research* **20**, 49–94 (2001).

[13] Curcio, C. A., Sloan, K. R., Kalina, R. E., and Hendrickson, A. E. Human photoreceptor topography. *The Journal of Comparative Neurology* **292**, 497–523 (1990).

[14] Roorda, A. and Williams, D. R. The arrangement of the three cone classes in the living human eye. *Nature* **397**, 520–522 (1999).

[15] Okawa, H. and Sampath, A. P. Optimization of single-photon response transmission at the rod-to-rod bipolar synapse. *Physiology* **22**, 279–286 (2007).

[16] Strettoi, E., Novelli, E., Mazzoni, F., Barone, I., and Damiani, D. Complexity of retinal cone bipolar cells. *Progress in Retinal and Eye Research* **29**, 272–283 (2010).

[17] Hubel, D. H. Exploration of the primary visual cortex. *Nature* **299**, 1955–1978 (1982).

[18] Blasdel, G. G. and Fitzpatrick, D. Physiological organization of layer 4 in the macaque striate cortex. *Journal of Neuroscience* **4**, 880–895 (1984).

[19] Blasdel, G. G. and Lund, J. S. Termination of afferent axons in macaque striate cortex. *Journal of Neuroscience* **3**, 1389–1413 (1983).

[20] Perkel, D. J., Bullier, J., and Kennedy, H. Topography of the afferent connectivity of area 17 in the macaque monkey: a double-labelling study. *Journal of Comparative Neurology* **253**, 374–402 (1986).

[21] Lund, J. S., Lund, R. D., Hendrickson, A. E., Bunt, A. H., and Fuchs, A. F. The origin of efferent pathways from the primary visual cortex, area 17, of the macaque monkey as shown by retrograde transport of horseradish peroxidase. *Journal of Comparative Neurology* **164**, 287–303 (1975).

[22] Lund, J. S. Local circuit neurons of macaque monkey striate cortex. i. neurons of laminae 4c and 5a. *Journal of Comparative Neurology* **257**, 60–92 (1987).

[23] Lund, J. S. and Yoshioka, T. Local circuit neurons of macaque monkey striate cortex. iii. neurons of laminae 4b, 4a, and 3b. *Journal of Comparative Neurology* **311**, 234–258 (1991).

[24] Lund, J. S. and Wu, C. Q. Local circuit neurons of macaque monkey striate cortex. iv. neurons of laminae 1-3a. *Journal of Comparative Neurology* **384**, 109–126 (1997).

[25] Lund, J. S. and Hawken, M. J. Local circuit neurons of macaque monkey striate cortex. ii. neurons of laminae 5b and 6. *Journal of Comparative Neurology* **276**, 1–29 (1988).

[26] Hubel, D. H. and Wiesel, T. N. Laminar and columnar distribution of geniculo-cortical fibers in the macaque monkey. *Journal of Comparative Neurology* **146**, 421–450 (1972).

[27] Lund, J. S. and Boothe, R. G. Interlaminar connections and pyramidal neuron organization in the visual cortex, area 17, of the macaque monkey. *Journal of Comparative Neurology* **159**, 305–334 (1975).

[28] Hubel, D. H. and Wiesel, T. N. Receptive fields of single neurones in the cat's striate cortex. *Journal of Physiology* **148**, 574–591 (1959).

[29] Valois, R. L. D., Yund, E. W., and Hepler, N. The orientation and direction selectivity of cells in the macaque visual cortex. *Vision Research* **22**, 531–544 (1982).

[30] Cavanaugh, J. R., Bair, W., and Movshon, J. A. Nature and interaction of signals from the receptive field center and surround in macaque v1 neurons. *Journal of Neurophysiology* **88**, 2530–2546 (2002).

[31] Leventhal, A. G., Thompson, K. G., Liu, D., Zhou, Y., and Ault, S. J. Concomitant sensitivity to orientation, direction, and color of cells in layers 2, 3, and 4 of monkey striate cortex. *Journal of Neuroscience* **15**, 1808–1818 (1995).

[32] Hubel, D. H. and Wiesel, T. N. Receptive fields and functional architecture of monkey striate cortex. *Journal of Physiology* **195**, 215–243 (1968).

[33] Felleman, D. J. and Essen, D. C. V. Distributed hierarchical processing in the primate cerebral cortex. *Cerebral Cortex* **1**, 1–47 (1991).

[34] Essen, D. C. V., Anderson, C. H., and Felleman, D. J. Information processing in the primate visual system: an integrated systems perspective. *Science* **255**, 419–423 (1992).

[35] Roe, A. and Tso, D. Y. Visual topography in primate v2: multiple representation across functional stripes. *Journal of Neuroscience* **15**, 3689–3715 (1995).

[36] Kaskan, P. M., Lu, H. D., Dillenburger, B. C., Kaas, J. H., and Roe, A. W. The organization of orientation-selective, luminance-change and binocular-preference domains in

the second (v2) and third (v3) visual areas of new world owl monkeys as revealed by intrinsic signal optical imaging. *Cerebral Cortex* **19**, 1394–1407 (2009).

[37] Chklovskii, D. B. and Koulakov, A. A. Maps in the brain: What can we learn from them? *Annual Review Neuroscience* **27**, 369–392 (2004).

[38] Ko, H., Hofer, S. B., Pichler, B., Buchanan, K. A., J.esper, P., and Mrsic-Flogel, T. D. Functional specificity of local synaptic connections in neocortical networks. *Nature* **473**, 87–91 (2011).

[39] Hubel, D. H. and Wiesel, T. N. Sequence regularity and geometry of orientation columns in the monkey striate cortex. *Journal of Comparative Neurology* **158**, 267–293 (1974).

[40] Hubel, D. H., Wiesel, T. N., and Stryker, M. P. Orientation columns in macaque monkey visual cortex demonstrated by the 2-deoxyglucose autoradiographic technique. *Nature* **269**, 328–330 (1977).

[41] Yacoub, E., Harel, N., and Ugurbil, K. High-field fmri unveils orientation columns in humans. *Proceedings of the National Academy of Sciences* **105**, 10607–10612 (2008).

[42] Kaschube, M., Schnabel, M., Lowel, S., Coppola, D. M., White, L. E., and Wolf, F. Universality in the evolution of orientation columns in the visual cortex. *Science* **330**, 1113–1116 (2010).

[43] Li, Y., Lu, H., Cheng, P. L., Ge, S., Xu, H., Shi, S. H., and Dan, Y. Clonally related visual cortical neurons show similar stimulus feature selectivity. *Nature* **486**, 118–121 (2012).

[44] Ringo, J. L. Neuronal interconnection as a function of brain size. *Brain, Behavior and Evolution* **38**, 1–6 (1991).

[45] Kaas, J. Why is brain size so important: Design problems and solutions as neocortex gets bigger or smaller. *Brain and Mind* **1**, 7–23 (2000).

[46] Rakic, P. Specification of cerebral cortical areas. *Science* **241**, 170–176 (1988).

[47] Andrews, T. J., Halpern, S. D., and Purves, D. Correlated size variations in human visual cortex, lateral geniculate nucleus and optic tract. *Journal of Neuroscience* **17**, 2859–2868 (1997).

[48] Dougherty, R. F., Koch, V. M., Brewer, A. A., Fischer, B., Modersitzki, J., and Wandell, B. A. Visual field representations and locations of visual areas v1/2/3 in human visual cortex. *Journal of Vision* **3**, 586–598 (2003).

[49] Joyner, A. H., Bloss, C. S., Bakken, T. E., Rimol, L. M., Melle, I., Agartz, I., Djurovic, S., Topol, E. J., Schork, N. J., Andreassen, O. A., and Dale, A. M. A common mecp2 haplotype associates with reduced cortical surface area in humans in two independent populations. *Proceedings of the National Academy of Sciences* **106**, 15483–15488 (2009).

[50] Bakkena, T. E., Roddey, J. C., Djurovicd, S., and Dale, A. M. Association of common genetic variants in gpcpd1 with scaling of visual cortical surface area in humans. *Proceedings of the National Academy of Sciences* **10**, 1073 (2012).

[51] Rubenstein, J. L. Genetic control of cortical regionalization and connectivity. *Cerebral Cortex* **9**, 524–532 (1999).

[52] Rubenstein, J. L. and Rakic, P. Genetic control of cortical development. *Cerebral Cortex* **9**, 521–523 (1999).

[53] Pallas, S. L. Intrinsic and extrinsic factors that shape neocortical specification. *Trends in Neuroscience* **24**, 417–423 (2001).

[54] Thompson, P. M. Genetic influences on brain structure. *Nature Neuroscience* **4**, 1253–1258 (2001).

[55] Glahn, D. C., Thompson, P. M., and Blangero, J. Neuroimaging endophenotypes: strategies for finding genes influencing brain structure and function. *Human Brain Mapping* **28**, 488–501 (2007).

[56] Peper, J. S. Genetic influences on human brain structure: a review of brain imaging studies in twins. *Human Brain Mapping* **28**, 464–473 (2007).

[57] Panizzon, M. S., Christine, F. N., Eyler, L. T., Jernigan, T. L., Wormley, E., Neale, M., Jacobson, K., Lyons, M. J., Grant, M. D., Franz, C. E., Xian, H., Tsuang, M., Fischl, B., Seidman, L., Dale, A., and Kremen, W. S. Distinct genetic influences on cortical surface area and cortical thickness. *Cerebral Cortex* **19**, 2728–2735 (2009).

[58] Chen, C. H., Panizzon, M. S., Eyler, L. T., Jernigan, T. L., Thompson, W., Notestine, C., Jak, A. J., Neale, M. C., Franz, C. E., Hamza, S., Lyons, M. J., Grant, M. D., Fischl, B.,

Seidman, L. J., Tsuang, M. T., Kremen, W. S., and Dale, A. M. Genetic influences on cortical regionalization in the human brain. *Neuron* **72**, 537–544 (2011).

[59] Huettel, S. A., Song, A. W., and McCarthy, G. Functional magnetic resonance imaging. *Sinauer Associates Publishers* (2004).

[60] Raichle, M. E. A brief history of human brain mapping. *Trends in Neurosciences* **32**, 118–126 (2008).

[61] Jin, J. Electromagnetic analysis and design in magnetic resonance imaging. *CRC Press* (1999).

[62] Slichter, C. P. Principles of magnetic resonance. *Springer-Verlag* (1990).

[63] Twieg, D. B. The k-trajectory formulation of the nmr imaging process with applications in analysis and synthesis of imaging methods. *Medical Physics* **10**, 610–621 (1983).

[64] Bracewell, R. N. The fourier transform and its applications. *McGraw-Hill* **10**, 610–621 (1986).

[65] Purcell, E. M., Torrey, H. C., and Pound, R. V. Resonance absorption by nuclear magnetic moments in a solid. *Physical Review* **69**, 37–38 (1945).

[66] Bloch, F., Hansen, W. W., and Packard, M. Nuclear induction. *Physical Review* **70**, 460–473 (1946).

[67] Haacke, E. M., Brown, R. W., Thompson, M. R., and Venkatesan, R. Magnetic resonance imaging: Physical principles and sequence design. *John Wiley and Sons* (1999).

[68] Roy, C. S. and Sherrington, C. S. On the regulation of the blood-supply of the brain. *Journal of Physiology* **11**, 85–108 (1890).

[69] Duvernoy, H. M., Delon, S., and Vannson, J. L. Cortical blood vessels of the human brain. *Brain Research Bulletin* **7**, 519–579 (1981).

[70] Attwell, D. and Iadecola, C. The neural basis of functional brain imaging signals. *Trends in Neuroscience* **25**, 621–625 (2002).

[71] Sereno, M. I., Dale, A. M., Reppas, J. B., Kwong, K. K., Belliveau, J. W., Brady, T. J., Rosen, B. R., and Tootell, R. B. H. Borders of multiple visual areas in human revealed by functional magnetic resonance imaging. *Science* **268**, 889–893 (1995).

[72] Kolster, H., Peeters, R., and Orban, G. A. The retinotopic organization of the human middle temporal area mt/v5 and its cortical neighbors. *Journal of Neuroscience* **30**, 9801–9820 (2010).

[73] Wandell, B. A., Brewer, A. A., and Dougherty, R. F. Visual field map clusters in human cortex. *Philosophical Transactions of the Royal Society B* **1628**, 1–15 (2005).

[74] Wandell, B. A., Dumoulin, S. O., and Brewer, A. A. Visual field maps in human cortex. *Neuron* **56**, 366–383 (2007).

[75] Larsson, J. and Heeger, D. J. Two retinotopic visual areas in human lateral occipital cortex. *Journal of Neuroscience* **26**, 13128–13142 (2006).

[76] Silver, M. and Kastner, S. Topographic maps in human frontal and parietal cortex. *Trends in Cognitive Sciences* **13**, 488–495 (2009).

[77] Brewer, A. A. and Barton, B. Visual field map organization in human visual cortex. *Visual Cortex: Current Status and Perspectives* **1**, 29–60 (2012).

[78] Dale, A. M., Fischl, B., and Sereno, M. I. Cortical surface-based analysis i: Segmentation and surface reconstruction. *Neuroimage* **9**, 179–194 (1999).

[79] Fischl, B., Sereno, M. I., and Dale, A. M. Cortical surface-based analysis ii: Inflation, flattening, and a surface based coordinate system. *Neuroimage* **9**, 195–207 (1999).

[80] Friston, K. J., Harrison, L., and Penny, W. Dynamic causal modelling. *Neuroimage* **19**, 1273–1302 (2003).

[81] Friston, K. J. Modalities, models, and models in functional neuroimaging. *Science* **326**, 399–403 (2009).

[82] Firston, K. Functional and effective connectivity: A review. *Brain Connectivity* **1**, 13–36 (2011).

[83] Smith, S. M., Miller, K. L., Salimi-Khorshidi, G., Webster, M., Beckmann, C. F., Nichols, T. E., Ramsey, J. D., and Woolrich, M. W. Network modelling methods for fmri. *Neuroimage* **54**, 875–891 (2011).

[84] David, O., Guillemain, I., Saillet, S., Reyt, S., Deransart, C., Segebarth, C., and Depaulis, A. Identifying neural drivers with functional mri: An electrophysiological validation. *PLoS Biology* **23**, 2683–2697 (2008).

[85] Aertsen, A. and Preissl, H. Dynamics of activity and connectivity in physiological neuronal networks. *Nonlinear Dynamics and Neuronal Networks* **12**, 281–301 (1991).

[86] Gerstein, G. L. and Perkel, D. H. Simultaneously recorded trains of action potentials: analysis and functional interpretation. *Science* **16**, 828–830 (1969).

[87] Friston, K. J., Mechelli, A., Turner, R., and Prices, C. J. Nonlinear responses in fmri: The balloon model, volterra kernels, and other hemodynamics. *Neuroimage* **12**, 466–477 (2000).

[88] Deco, G., Jirsa, V. K., Robinson, P. A., Breakspear, M., and Friston, K. The dynamic brain: From spiking neurons to neural masses and cortical fields. *PLoS Computational Biology* **4**, e1000092 (2008).

[89] Penny, W. D., Mattout, J., and Trujillo-Barreto, N. Bayesian model selection and averaging. *Statistical Parametric Mapping: Models for brain imaging* , 1–29 (2006).

[90] Penny, W. Comparing dynamic causal models using aic, bic and free energy. *Neuroimage* **59**, 319–330 (2012).

[91] Itti, L., Koch, C., and Niebur, E. A model of saliency-based visual attention for rapid scene analysis. *IEEE Transactions Pattern Analysis and Machine Intelligence* **20**, 1254–1259 (1998).

[92] Itti, L. and Koch, C. Computational modeling of visual attention. *Nature Reviews Neuroscience* **2**, 194–203 (2001).

[93] Ban, W. S., Shin, J. K., and Lee, M. Face detection using biologically motivated saliency map model. *Neural Networks* **1**, 119–124 (2003).

[94] Rodrigues, J. and Hans du Buf, J. M. Face recognition by cortical multi-scale line and edge representations. *Image Analysis and Recognition* **4142**, 329–340 (2006).

[95] Cappelli, R., Franco, A., and Maio, D. Gabor saliency map for face recognition. *Image Analysis and Processing* **42**, 443–447 (2007).

[96] Albrecht, D. G. Visual cortex neurons in monkey and cat: Effect of contrast on the spatial and temporal phase transfer functions. *Visual Neuroscience* **12**, 1191–1210 (1995).

[97] Swindale, N. V. How many maps are there in visual cortex? *Cerebral Cortex* **10**, 633–643 (2000).

[98] Peng, X. and Essen, D. C. V. Peaked encoding of relative luminance in macaque areas v1 and v2. *Journal of Neurophysiology* **93**, 1620–1632 (2005).

[99] Duncan, R. O. and Boynton, G. M. Cortical magnification within human primary visual cortex correlates with acuity thresholds. *Neuron* **38**, 659–671 (2003).

[100] Eagleman, D. M. Visual illusions and neurobiology. *Nature Review Neuroscience* **2**, 920–926 (2001).

[101] Albright, T. D. and Stoner, G. R. Contextual influences on visual processing. *Annual Review of Neuroscience* **25**, 339–379 (2002).

[102] Schwartz, O., Hsu, A., and Dayan, P. Space and time in visual context. *Nature Review Neuroscience* **8**, 522–535 (2007).

[103] Nauhaus, I., Benucci, A., Carandini, M., and Ringach, D. L. Neuronal selectivity and local map structure in visual cortex. *Neuron* **57**, 673–679 (2008).

[104] Gilbert, C. D. and Wiesel, T. N. The influence of contextual stimuli on the orientation selectivity of cells in primary visual cortex of the cat. *Vision Research* **30**, 1689–1701 (1990).

[105] Zipser, K., Lamme, V. A. F., and Schiller, P. H. Contextual modulation in primary visual cortex. *Journal of Neuroscience* **16**, 7376–7389 (1996).

[106] MacEvoy, S. P. and Paradiso, M. A. Lightness constancy in primary visual cortex. *Proceedings of the National Academy of Sciences* **98**, 8827–8831 (2001).

[107] Kinoshita, M. and Komatsu, H. Neural representation of the luminance and brightness of a uniform surface in the macaque primary visual cortex. *Journal of Neurophysiology* **86**, 2559–2570 (2001).

[108] Garcia-Perez, M. A., Giorgi, R. G., Woods, R. L., and Peli, E. Thresholds vary between spatial and temporal forced-choice paradigms: The case of lateral interactions in peripheral vision. *Spatial Vision* **18**, 99–127 (2005).

[109] Levitt, H. Transformed up-down methods in psychoacoustic. *Journal of the Acoustical Society of America* **49**, 467–477 (1971).

[110] Fockert, J., Davidoff, J., Fagot, J., Parron, C., and Goldstein, J. More accurate size contrast judgments in the ebbinghaus illusion by a remote culture. *Journal of Experimental Psychology: Human Perception and Performance* **33**, 738–742 (2007).

[111] Doherty, M., Tsuji, H., and Phillips, W. A. The context sensitivity of visual size perception varies across cultures. *Perception* **37**, 1426–1433 (2008).

[112] Blinkov, S. M. and Glezer, I. J. The human brain in figures and tables: A quantitative handbook. *Plenum Press* (1968).

[113] Fischl, B. and Dale, A. M. Measuring the thickness of the human cerebral cortex from magnetic resonance images. *Proceedings of the National Academy of Sciences* **97**, 11050–11055 (2000).

[114] Hilgetag, C. C. and Barbas, H. Role of mechanical factors in the morphology of the primate cerebral cortex. *PLoS Computational Biology* **2**, e22 (2006).

[115] Dekaban, A. S. and Sadowsky, D. Changes in brain weights during the span of human life: relation of brain weights to body heights and body weights. *Annals of Neurology* **4**, 345–356 (1978).

[116] Hendley, C. D. The relation between visual acuity and brightness discrimination. *The Journal of General Physiology* **20**, 433–457 (1948).

[117] Paradiso, M. A. and Carney, T. Orientation discrimination as a function of stimulus eccentricity and size. *Vision Research* **28**, 867–874 (1988).

[118] Rovamo, J., Luntinen, O., and Nasanen, R. Modelling the dependence of contrast sensitivity on grating area and spatial frequency. *Vision Research* **33**, 2773–2788 (1993).

[119] Yund, E. W. and Armington, J. C. Color and brightness contrast effects as a function of spatial variables. *Vision Research* **15**, 917–929 (1975).

[120] Cannon, M. W. and Fullenkamp, C. S. A model for inhibitory lateral interaction effects in perceived contrast. *Vision Research* **36**, 1115–1125 (1996).

[121] Smith, S. and Wenderoth, P. Large repulsion, but not attraction, tilt illusions occur when stimulus parameters selectively favour either transient (m-like) or sustained (p-like) mechanisms. *Vision Research* **39**, 4113–4121 (1999).

[122] Dumoulin, S. O. and Wandell, B. A. Population receptive field estimates in human visual cortex. *Neuroimage* **39**, 647–660 (2008).

[123] Friston, K. J., Fletcher, P., Josephs, O., Holmes, A., M. D. Rugg, M., and Turner, R. Event-related fmri: characterizing differential responses. *Neuroimage* **7**, 30–40 (1998).

[124] Glover, G. H. Deconvolution of impulse response in event-related bold fmri. *Neuroimage* **9**, 416–429 (1999).

[125] Desikan, R. S., Segonne, F., Fischl, B., Quinn, B. T., Dickerson, B. C., Blacker, D., Buckner, R. L., Dale, A. M., Maguire, R. P., Hyman, B. T., Albert, M. S., and Killiany, R. J. An automated labeling system for subdividing the human cerebral cortex on mri scans into gyral based regions of interest. *Neuroimage* **31**, 968–980 (2006).

[126] Vogels, R. and Orban, G. A. Decision processes in visual discrimination of line orientation. *Journal of Experimental Psychology: Human Perception and Performance* **12**, 115–132 (1986).

[127] Gold, J. I. and Ding, L. How mechanisms of perceptual decision-making affect the psychometric function. *Progress in Neurobiology* **103**, 98–114 (2013).

[128] Yacoub, E., Shmuel, A., Logothetis, N., and Ugurbil, K. Robust detection of ocular dominance columns in humans using hahn spin echo bold functional mri at 7 tesla. *Neuroimage* **37**, 1161–1177 (2007).

[129] Sengpiel, F., Blakemore, C., and Harrad, R. Interocular suppression in the primary visual cortex: a possible neural basis of binocular rivalry. *Vision Research* **35**, 179–195 (1995).

[130] Blake, R. A primer on binocular rivalry, including current controversies. *Brain Mind* **2**, 5–38 (2001).

[131] Genc, E., Bergmann, J., Subger, W., and Kohler, A. Surface area of early visual cortex predicts individual speed of traveling waves during binocular rivalry. *Cerebral Cortex* **24**, 1093–1098 (2014).

[132] Albright, T. D., Desimone, R., and Gross, C. G. Columnar organization of directionally selective cells in visual area mt of the macaque. *Journal of Neurophysiology* **51**, 16–31 (1984).

[133] Sereno, M. I., Lutti, A., Weiskopf, N., and Dick, F. Mapping the human cortical surface by combining quantitative t1 with retinotopy. *Cerebral Cortex* **23**, 1231–1239 (2013).

[134] Mountcastle, V. B. The columnar organization of the neocortex. *Brain* **120**, 701–722 (1997).

[135] Rakic, P. Neurons in rhesus monkey visual cortex: Systematic relation between time of origin and eventual disposition. *Science* **183**, 425–427 (1974).

[136] Bugbee, N. M. and Rakic, P. Columnar organization of corticocortical projections in squirrel and rhesus monkeys: Similarity of column width in species differing in cortical volume. *The Journal of Comparative Neurology* **220**, 355–364 (1983).

[137] Jones, E. G. Microcolumns in the cerebral cortex. *Proceedings of the National Academy of Sciences* **97**, 5019–5021 (2000).

[138] Haug, H. Brain sizes, surfaces, and neural sizes of the cortex cerebri: A stereological investigation of man and his variability and a comparison with some mammals. *The American Journal of Anatomy* **180**, 126–142 (1987).

[139] Gilbert, C. D., Sigman, M., and Crist, R. E. The neural basis of perceptual learning. *Neuron* **31**, 681–697 (2001).

[140] Ashburner, J. Spm: A history. *NeuroImage* **62**, 791–800 (2012).

[141] Jenkinson, M., Beckmann, C. F., Behrens, T. E., Woolrich, M. W., and Smith, S. M. Fsl. *NeuroImage* **62**, 782–790 (2012).

[142] Fischl, B. Freesurfer. *NeuroImage* **62**, 774–781 (2012).

[143] Bazin, P. L., Weiss, M., Dinse, J., Schafer, A., Trampel, R., and Turner, R. A computational framework for ultra-high resolution cortical segmentation at 7 tesla. *Neuroimage* , 10.1016 (2013).

[144] Helms, G., Dathe, H., and Dechent, P. Quantitative flash mri at 3t using a rational approximation of the ernst equation. *Magnetic Resonance in Medicine* **59**, 667–672 (2008).

[145] Weiskopf, N., Suckling, J., Williams, G., Correia, M. M., Inkster, B., Tait, R., Ooi, C., Bullmore, E. T., and Lutti, A. Quantitative multi-parameter mapping of r1, pd(*), mt, and r2(*) at 3t: a multi-center validation. *Frontiers in Neuroscience* **78**, doi: 10.3389 (2013).

[146] Preibisch, C. and Deichmann, R. Influence of rf spoiling on the stability and accuracy of t1 mapping based on spoiled flash with varying flip angles. *Magnetic Resonance in Medicine* **61**, 125–135 (2009).

[147] Lutti, A., Hutton, C., Finsterbusch, J., Helms, G., and Weiskopf, N. Optimization and validation of methods for mapping of the radiofrequency transmit field at 3t. *Magnetic Resonance in Medicine* **64**, 229–238 (2010).

[148] Lutti, A., Stadler, J., Josephs, O., Windischberger, C., Speck, O., Bernarding, J., Hutton, C., and Weiskopf, N. Robust and fast whole brain mapping of the rf transmit field b1 at 7t. *PLoS One* **7**, e32379 (2012).

[149] Spitzer, V., Ackerman, M. J., Scherzinger, A. L., and Whitlock, D. The visible human male: a technical report. *Journal of the American Medical Informatics Association* **3**, 118–130 (1996).

[150] Salvado, O., Hillenbrand, C., Zhang, S., and Wilson, D. L. Method to correct intensity inhomogeneity in mr images for atherosclerosis characterization. *IEEE Transactions on Medical Imaging* **25**, 539–552 (2006).

[151] Stalling, D., Westerhoff, M., and Hege, H. C. Amira: A highly interactive system for visual data analysis. *The Visualization Handbook (Elsevier)* **2**, 749–767 (2005).

[152] Mazziotta, J., Toga, A., Evans, A., Fox, P., Lancaster, J., Zilles, K., Woods, R., Paus, T., Simpson, G., Pike, B., Holmes, C., Collins, L., Thompson, P., MacDonald, D., Iacoboni, M., Schormann, T., Amunts, K., Palomero-Gallagher, N., Geyer, S., Parsons, L., Narr, K., Kabani, N., Goualher, G. L., Boomsma, D., Cannon, T., Kawashima, R., and Mazoyer, B. A probabilistic atlas and reference system for the human brain: International consortium for brain mapping (icbm). *Computer Vision and Image Understanding* **356**, 1293–1322 (2001).

[153] Ringach, D. L., Hawken, M. J., and Shapley, R. Dynamics of orientation tuning in macaque primary visual cortex. *Nature* **387**, 281–284 (1997).

[154] Purushothaman, G. and Bradley, D. C. Neural population code for fine perceptual decisions in area mt. *Nature Neuroscience* **32**, 99–106 (2005).

[155] Chisum, H. J., Mooser, F., and Fitzpatrick, D. Horizontal connections in tree shrew visual cortex. *Journal of Neuroscience* **23**, 2947–2960 (2003).

[156] Hirsch, J. A. and Martinez, L. M. Laminar processing in the visual cortical column. *Current Opinion in Neurobiology* **16**, 377–384 (2006).

[157] Angelucci, A., Levitt, J. B., Walton, E. J. S., Hupe, J. M., Bullier, J., and Lund, J. S. Circuits for local and global signal integration in primary visual cortex. *Journal of Neuroscience* **22**, 8633–8646 (2002).

[158] Sporns, O. and Zwi, J. D. The small world of the cerebral cortex. *Neuroinformatics* **2**, 145–162 (2004).

[159] Lewis, J. D., Theilmann, R. J., Sereno, M. I., and Townsend, J. The relation between connection length and degree of connectivity in young adults: A dti analysis. *Cerebral Cortex* **19**, 554–562 (2009).

[160] Koch, C. Cable theory in neurons with active, linearized membranes. *Biological Cybernetics* **50**, 15–33 (1984).

[161] Womelsdorf, T., Schoffelen, J. M., Oostenveld, R., Singer, W., Desimone, R., Engel, A. K., and Fries, P. Modulation of neuronal interactions through neuronal synchronization. *Science* **316**, 1609–1612 (2007).

[162] Sun, W. and Dan, Y. Layer-specific network oscillation and spatiotemporal receptive field in the visual cortex. *Proceedings of the National Academy of Sciences* **106**, 17986–17991 (2009).

[163] Vogels, T. P., Rajan, K., and Abbott, L. F. Neural network dynamics. *Annual Review of Neuroscience* **28**, 357–376 (2005).

[164] Carandini, M. and Heeger, D. J. Normalization as a canonical neural computation. *Nature Reviews Neuroscience* **269**, 1877–1880 (1995).

[165] Rao, R. P. N. and Ballard, D. H. Predictive coding in the visual cortex: a functional interpretation of some extra-classical receptive-field effects. *Nature Neuroscience* **2**, 79–87 (1999).

[166] Jansen, B. H. and Rit, V. G. Electroencephalogram and visual evoked potential generation in a mathematical model of coupled cortical columns. *Biological Cybernetics* **73**, 357–366 (1995).

[167] Thomson, A. M. and Bannister, A. P. Interlaminar connections in the neocortex. *Cerebral Cortex* **13**, 5–14 (2003).

[168] David, O. and et al. Dynamic causal modeling of evoked responses in eeg and meg. *Neuroimage* **30**, 1255–1272 (2006).

[169] Babajani, A. and Soltanian-Zadeh, H. Integrated meg/eeg and fmri model based on neural masses. *IEEE Transactions on Biomedical Engineering* **53**, 1794–1801 (2006).

[170] Somers, D. C., Nelson, S. B., and Sur, M. An emergent model of orientation selectivity in cat visual cortical simple cells. *Journal of Neuroscience* **15**, 5448–5465 (1995).

[171] Carandini, M. and Ringach, D. L. Predictions of a recurrent model of orientation selectivity. *Vision Research* **37**, 3061–3071 (1997).

[172] Villringer, A. and Chance, B. Non-invasive optical spectroscopy and imaging of human brain function. *Trends in Neuroscience* **20**, 435–442 (1997).

[173] Nemoto, M., Nomura, Y., Sato, C., Tamura, M., Houkin, K., Koyanagi, I., and Abe, H. Analysis of optical signals evoked by peripheral nerve stimulation in rat somatosensory cortex: Dynamic changes in hemoglobin concentration and oxygenation. *Journal of Cerebral Blood Flow Metabolism* **19**, 246–259 (1999).

[174] Kohl, M., Lindauer, U., Royl, G., Kuhl, M., Gold, L., Villringer, A., and Dirnagl, U. Physical model for the spectroscopic analysis of cortical intrinsic optical signals. *Physics in Medicine and Biology* **45**, 3749–3764 (2000).

[175] Sirotin, Y. B., Hillman, E. M. C., Bordier, C., and Das, A. Spatiotemporal precision and hemodynamic mechanism of optical point spreads in alert primates. *Proceedings of the National Academy of Sciences* **106**, 18390–18395 (2009).

[176] Markounikau, V., Igel, C., Grinvald, A., and Jancke, D. A dynamic neural eld model of mesoscopic cortical activity captured with voltage-sensitive dye imaging. *PLoS Computational Biology* **6**, e1000919 (2010).

[177] Ogata, K. Modern control engineering (3rd edition). *Prentice Hall* (1997).

[178] Boynton, G. M., Engel, S. A., Glover, G. H., and Heeger, D. V. Linear systems analysis of functional magnetic resonance imaging in human v1. *Joural of Neuroscience* **16**, 4207–4221 (1996).

[179] Lutti, A., Thomas, D. L., Hutton, C., and Weiskopf, N. High-resolution functional mri at 3 t: 3d/2d echo-planar imaging with optimized physiological noise correction. *Magnetic Resonance in Medicine* **21**, 1657–1664 (2013).

[180] Hansen, K. A., David, S. V., and Gallant, J. L. Parametric reverse correlation reveals spatial linearity of retinotopic human v1 bold response. *Neuroimage* **23**, 233–241 (2004).

[181] Jiang, J., Zhu, W., Shi, F., Liu, Y., Li, J., Qin, W., Li, K., Yu, C., and Jiang, T. Thick visual cortex in the early blind. *Journal of Neuroscience* **29**, 2205–2211 (2009).

[182] Jacobson, S. G., Aleman, T. S., Cideciyan, A. V., Heon, E., Golczak, M., Beltran, W. A., Sumaroka, A., .Schwartz, S. B., Roman, A. J., Windsor, E. A. W., Wilson, J. M., Aguirre, G. D., Stone, E. M., and Palczewski, K. Human cone photoreceptor dependence on rpe65 isomerase. *Proceedings of the National Academy of Sciences* **104**, 15123–15128 (2007).

[183] Lamme, V. A., Super, H., and Spekreijse, H. Feedforward, horizontal, and feedback processing in the visual cortex. *Current Opinion in Neurobiology* **8**, 529–535 (1998).

[184] Levitt, J. B. and Lund, J. S. Contrast dependence of contextual effects in primate visual cortex. *Nature* **387**, 73–76 (1997).

[185] Dragoi, V. and Sur, M. Dynamic properties of recurrent inhibition in primary visual cortex: Contrast and orientation dependence of contextual effects. *Journal of Neurophysiology* **83**, 1019–1030 (2000).

[186] Lumer, E. K., Friston, K. J., and Rees, G. Neural correlates of perceptual rivalry in the human brain. *Science* **280**, 1930–1933 (1998).

[187] Murray, S. O., Boyaci, H., and Kersten, D. The representation of perceived angular size in human primary visual cortex. *Nature Neuroscience* **9**, 429–434 (2006).

[188] Weliky, M., Kandler, K., Fitzpatrick, D., and Katz, L. C. Patterns of excitation and inhibition evoked by horizontal connections in visual cortex share a common relationship to orientation columns. *Neuron* **15**, 541–552 (1995).

[189] Bosking, W. H., Zhang, Y., Schofield, B., and Fitzpatrick, D. Orientation selectivity and the arrangement of horizontal connections in tree shrew striate cortex. *Journal of Neuroscience* **17**, 2112–2127 (1997).

[190] Stettler, D. D., Das, A., Bennett, J., and Gilbert, C. D. Lateral connectivity and contextual interactions in macaque primary visual cortex. *Neuron* **36**, 739–750 (2002).

[191] Bair, W., Cavanaugh, J. R., and Movshon, J. A. Time course and time-distance relationships for surround suppression in macaque v1 neurons. *Journal of Neuroscience* **23**, 7690–7701 (2003).

[192] Schwabe, L., Obermayer, K., Angelucci, A., and Bressloff, P. C. The role of feedback in shaping the extra-classical receptive field of cortical neurons: a recurrent network model. *Journal of Neuroscience* **26**, 9117–9129 (2006).

[193] Tolhurst, D. J. and Thompson, P. G. Orientation illusions and after-effects: inhibition between channels. *Vision Research* **15**, 967–972 (1975).

[194] Sengpiel, F., Sen, A., and Blackemore, C. Characteristics of surround inhibition in cat area 17. *Experimental Brain Research* **116**, 216–228 (1997).

[195] Schwartz, O., Sejnowski, T. J., and Dayan, P. Perceptual organization in the tilt illusion. *Journal of Vision* **9**, 1–20 (2009).

[196] Gong, G., He, Y., Concha, L., Lebel, C., Gross, D. W., Evans, A. C., and Beaulieu, C. Mapping anatomical connectivity patterns of human cerebral cortex using in vivo diffusion tensor imaging tractography. *Cerebral Cortex* **19**, 524–536 (2008).

[197] Friston, K. J. Functional and effective connectivity in neuroimaging: A synthesis. *Human Brain Mapping* **2**, 56–78 (1994).

[198] Drew, P. J., Shih, A. Y., Driscoll, J. D., Knutsen, P. M., Blinder, P., Davalos, D., Akassoglou, K., Tsai, P. S., and Kleinfeld, D. Chronic optical access through a polished and reinforced thinned skull. *Nature Methods* **7**, 981–984 (2010).

[199] Andermann, M. L., Kerlin, A. M., and Reid, R. C. Chronic cellular imaging of mouse visual cortex during operant behavior and passive viewing. *Frontiers in Cellular Neuroscience* **4**, 3 (2010).

[200] Maguire, E. A., Gadian, D. G., Johnsrude, I. S., Good, C. D., Ashburner, J., Frackowiak, R. S. J., and Frith, C. D. Navigation-related structural change in the hippocampi of taxi drivers. *Proceedings of the National Academy of Sciences* **97**, 4398–4403 (2000).

[201] Draganski, B., Gaser, C., Busch, V., Schuierer, G., Bogdahn, U., and May, A. Changes in grey matter induced by training. *Nature* **427**, 311–312 (2004).

[202] Fleming, S. M., Weil, R. S., Nagy, Z., Dolan, R. J., and Rees, G. Relating introspective accuracy to individual differences in brain structure. *Science* **329**, 1541–1543 (2010).

[203] de Sousa, A. A., Sherwood, C. C., Mohlberg, H., Amunts, K., Schleicher, A., MacLeod, C. M., p. R. Hof, Frahmd, H., and Zilles, K. Hominoid visual brain structure volumes and the position of the lunate sulcus. *Journal of Human Evolution* **58**, 281–292 (2010).

[204] Schoenemann, P. T. Evolution of the size and functional areas of the human brain. *Annual Review Anthropology* **35**, 379–406 (2006).

[205] Song, C., Schwarzkopf, D., Kanai, R., and Rees, G. Reciprocal anatomical relationship between primary sensory and prefrontal cortices in the human brain. *Journal of Neuroscience* **31**, 9472–9480 (2011).

[206] Bishop, K. M., Goudreau, G., and O'Leary, D. D. M. Regulation of area identity in the mammalian neocortex by emx2 and pax6. *Science* **288**, 344–349 (2000).

[207] Gogtay, N., Giedd, J. N., Lusk, L., Hayashi, K. M., Greenstein, D., Vaituzis, A. C., Nugent, T. F., Herman, D. H., Clasen, L. S., Toga, A. W., Rapoport, J. L., and Thompson, P. M. Dynamic mapping of human cortical development during childhood through early adulthood. *Proceedings of the National Academy of Sciences* **101**, 8175–8179 (2004).

[208] Khaitovich, P., Weiss, G., Lachmann, M., Hellmann, I., Enard, W., Muetzel, B., Wirkner, U., Ansorge, W., and Paabo, S. A neutral model of transcriptome evolution. *PLoS Biology* **2**, 682–689 (2004).

[209] Evans, P. D., Gilbert, S. L., Mekel-Bobrov, N., Vallender, E. J., Anderson, J. R., Vaez-Azizi, L. M., Tishkoff, S. A., Hudson, R. R., and Lahn, B. T. Microcephalin, a gene regulating brain size, continues to evolve adaptively in humans. *Science* **309**, 1717–1720 (2005).

[210] Mekel-Bobrov, N., Gilbert, S. L., Evans, P. D., Vallender, E. J., Anderson, J. R., Hudson, R. R., Tishkoff, S. A., and Lahn, B. T. Ongoing adaptive evolution of aspm, a brain size determinant in homo sapiens. *Science* **309**, 1720–1722 (2005).